Aerodynamic and Aeroacoustic Analysis of Low-Reynolds Number Propellers Using Higher-Order RANS Transition Turbulence Modeling

Naina Pisharoti

Dissertation submitted to the Faculty of the
Virginia Polytechnic Institute and State University
in partial fulfillment of the requirements for the degree of

Doctor of Philosophy
in
Aerospace Engineering

Stefano Brizzolara, Chair
W. Nathan Alexander
Christopher Roy
William Devenport
Daniel Stillwell

April 26, 2024
Blacksburg, Virginia

Keywords: Flow Transition, Turbulence modeling, Reynolds Stress, Blade Self-noise

Aerodynamic and Aeroacoustic Analysis of Low-Reynolds Number Propellers Using Higher-Order RANS Transition Turbulence Modeling

Naina Pisharoti

(ABSTRACT)

The advent of advanced vehicle concepts involving Urban Air Mobility (UAM) and small Unmanned Aerial Systems (sUAS) has brought about a new class of rotorcraft technology which operate predominantly in low-Reynolds (Re) number regimes. In such regimes, the flow experiences complex boundary layer phenomena like laminar separation, flow transition and reattachment. These effects are known to greatly alter the flow at and near the rotor wall, influencing its aerodynamic performance as well as the noise generated. Capturing these effects in our computational models is necessary to further our understanding of rotor aerodynamics and acoustics.

The current study has introduced a novel RANS transition turbulence model, SSG/LRR-ω-γ, that is capable of modeling different modes of transition involving natural, bypass, separation-induced and crossflow transition. The model framework uses a Reynolds stress transport model, SSG/LRR-ω, as the base turbulence formulation and is coupled with Menter's γ transition model. It was validated using a number of canonical cases that exhibited different transition mechanisms and the model performed equivalently or better than existing state-of-the-art transition models. It is worthy to note that the proposed model was able to perform well in three-dimensional flows, demonstrated using the case of a prolate spheroid. This underscores the capability of Reynolds stress models to accurately capture complex flow curvatures, improving upon the capabilities of linear eddy viscosity models.

The transition model, integrated into OpenFOAM, was then employed to analyze two different UAV propellers. The rotor flow was examined using a URANS simulation with an overset grid. The objective was twofold: firstly, to validate the predictions generated by the proposed model for low-Reynolds number (low-Re) rotors, and secondly, to evaluate its effectiveness across a range of operating conditions. Comparisons were drawn against established fully turbulent and transition models. The analysis showed that transition models in general tended to be consistent in their predictions and less sensitive to changing operating conditions when compared to fully turbulent models. They also demonstrated the ability to accurately predict the mechanisms leading to separation and transition. Further, the proposed transition model demonstrated superior capability in capturing detailed flow features, particularly in the wake, compared to other fully turbulent and transition models, which is attributed to its Galilean invariant framework.

To leverage the boundary layer information obtained from the proposed model, a semi-empirical broadband noise prediction method was implemented. This method utilized boundary layer data predicted by URANS simulations to estimate blade self-noise. An evaluation of the fully turbulent k-ω SST model and the proposed transition model revealed that both exhibited reasonable accuracy at lower rotor advance ratios. However, the transition model performed better at higher advance ratios. It was also observed that CFD-based approaches provided superior prediction accuracy compared to lower-fidelity aerodynamic models in the context of blade self-noise prediction.

Finally, the proposed aerodynamic and acoustic computational framework was applied to a design case study of swept propellers to understand the advantages of blade sweep on rotor aerodynamics and noise. A qualitative analysis of the flow suggested that the swept rotor exhibited lower levels of blade wake interaction compared to the unswept geometry, in line with the experimental observations.

Aerodynamic and Aeroacoustic Analysis of Low-Reynolds Number Propellers Using Higher-Order RANS Transition Turbulence Modeling

Naina Pisharoti

(GENERAL AUDIENCE ABSTRACT)

Advanced vehicle concepts such as air taxis for Urban Air Mobility (UAM) and other multicopter applications like drone delivery, reconnaissance, etc. are emerging sectors in aviation that have garnered great industrial as well as academic interest. However, since these vehicles are expected to fly at low altitudes within urban settings, noise mitigation is of particular interest to improve their public acceptance. The vehicle configurations in these applications predominantly comprise of rotorcraft which operate at low Reynolds (Re) numbers and tip speeds. These operating conditions introduce complex phenomena like flow transition and separation within the boundary layer that significantly alter their aerodynamic as well as aeroacoustic performance. The current work proposes a novel transition turbulence model that improves prediction of these complex boundary layer mechanisms in low-Re propellers compared to the state-of-the-art. Furthermore, this work establishes a fast broadband noise prediction method by leveraging the detailed flow data from the transition model. The focus of this method is on modeling those propeller noise sources that are directly influenced by the aforementioned boundary layer phenomena (blade self-noise). The noise prediction study revealed that transition models yield consistent predictions across different operating conditions. Finally, a brief design study is conducted using the proposed aerodynamic and acoustic framework to assess the flow dynamics and possible noise mitigation capabilities of a swept propeller.

Acknowledgments

This work would not have been possible without the constant help and support I received from my family, friends, mentors and peers. First and foremost, I would like to thank my mother, Shalini Pisharoti, my father, Vinod Kumar Pisharoti, and my husband, Anirudh Sarma, for the immense support, patience, and encouragement they provided throughout the course of my PhD.

I extend my deepest gratitude to my PhD advisor, Dr. Stefano Brizzolara, for his invaluable guidance and unwavering faith in my abilities. His kindness and steadfast support during the various challenges I encountered throughout my PhD have been truly remarkable. I would also like to thank Dr. Nathan Alexander for his assistance with the aeroacoustics aspect of my work. I am grateful for his deep insights and constructive feedback, which significantly helped hone my research approach. My committee members, Dr. Christopher Roy and Dr. William Devenport, taught me the fundamentals upon which this work is built. I am ever grateful for the impact they have had on me as researchers and instructors. I would also like to extend my gratitude towards Dr. Daniel Stillwell for providing me with a very collaborative and enriching research environment at CMAR.

A special thanks to my colleague, Dr. Jeremiah Whelchel, for actively collaborating with me and providing experimental data that proved invaluable for validating my computational models. I would also like to acknowledge Matthew Brown at VT Advanced Research Computing for his constant assistance in accessing and using the supercomputing clusters, which significantly helped speed up my work. I am thankful to my peers at VT-iShip, all of whom worked on a diverse set of projects that I enjoyed learning and discussing about.

Lastly, I would like to thank my extended family, Pramodh Sarma, Achraj Sarma, and Ayush Pisharody, as well as all my friends in Blacksburg and Atlanta, whose constant love and support provided the strength I needed to persevere through my PhD journey.

Contents

List of Figures

List of Tables

Chapter 1

Introduction

1.1 Motivation

Advanced Air Mobility (AAM) is an emerging and exciting sector in aviation. The FAA and NASA define AAM as "an air transportation system that moves people and cargo between local, regional, intra-regional, and urban places previously not served or under-served by aviation using revolutionary new aircraft". The goal of AAM is to introduce innovative aircraft concepts to transport goods and people in a cost-effective and sustainable way. Rizzi et al. [93] classified AAM applications into four broad categories: small UAS (unmanned aerial systems), Urban Air Mobility (UAM), thin/short haul, and Large UAS and HALE (High Altitude Long Endurance). The sUAS aircraft tend to operate at low to mid level altitudes for applications pertaining to package delivery, reconnaissance, aerial photography and infrastructure inspection. Urban Air Mobility (UAM) involves transportation in urban and suburban settings to reduce traffic congestion, using the concept of eVTOLs (Electric Vertical Takeoff and Landing) or hybrid VTOLs [48, 93]. UAM aircraft are expected to fly at altitudes less than 3000 ft and transport upto 6 passengers. The thin/short haul category includes vehicles intended for flights less than 12,500 ft with 9-30 passengers or equivalent cargo weight. Lastly, vehicles serving the large UAS and HALE markets are intended to perform long endurance missions at a broad range of altitudes with no transportation of humans.

Due to the low operating altitudes of Urban Air Mobility (UAM) and small Unmanned Aerial Systems (sUAS) applications, these aircraft face distinctive challenges. A significant concern within these AAM categories revolves around the noise they generate and their consequent impact on communities as well as the environment [93, 120]. The National Academies of Science, Engineering, and Medicine have underscored public acceptance, particularly regarding noise pollution, as one of the foremost challenges in the advancement of Advanced Air Mobility (AAM) [85]. Furthermore, a psychoacoustic study conducted by researchers at NASA Langley revealed that participants perceived drone noise to be more intrusive compared to noise from traditional road vehicles [19]. Therefore, to improve community acceptance and reduce acoustic signatures of these vehicles, the sources responsible for the noise generated by them need to be well understood. Given this interesting challenge, the current work focuses on the UAM and sUAS application space.

eVTOLs for UAM have varied configurations, which have been proposed based on their use-case and operating conditions [47]. They vary in the number or rotors used, rotor placement and geometry of the aircraft. Figure 1.1 (a) shows the Joby S4 aircraft which has a tilt-rotor configuration with six rotors. Figure 1.1 (b) shows the two-seater Volocopter 2X which employs 18 fixed-pitch propellers and finally, figure 1.1 (c) shows the lift+cruise configuration with tilt-rotors used in the Wisk Gen-6 aircraft. Similarly, the sUAS space, which mainly comprises of multi-copters, is also seeing rapid innovation in the design and applications. Companies like Google, Amazon and Zipline are actively working on introducing efficient design ideas to bring sustainable, low emission and faster logistic services to urban as well as rural communities [84]. Figure 1.2 (a) shows the Platform 2 drone by Zipline with their patented low-noise propellers being highlighted and figure 1.2 (b) shows the MK30 drone introduced by Prime Air.

As evident from the examples above, rotors serve as the primary lift-generating components

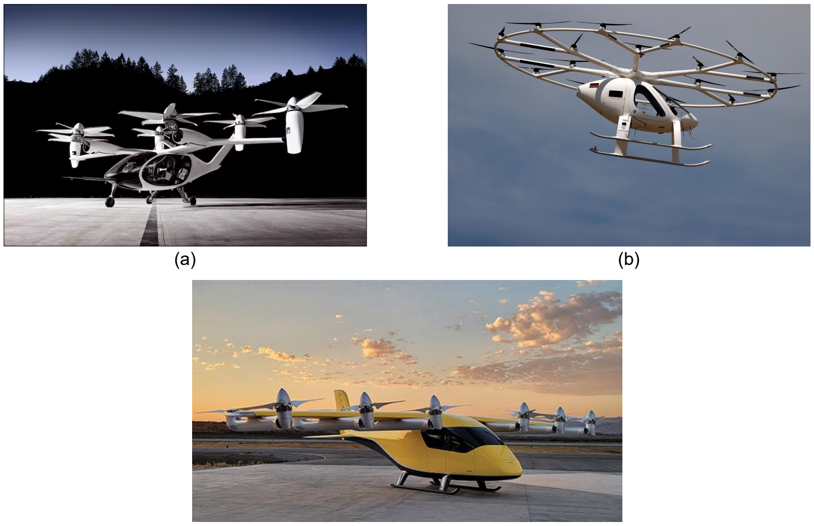

(a) (b)

(c)

Figure 1.1: eVTOL configurations: a) Joby S4 b) Volocopter 2X and c) Wisk Gen 6 aircraft

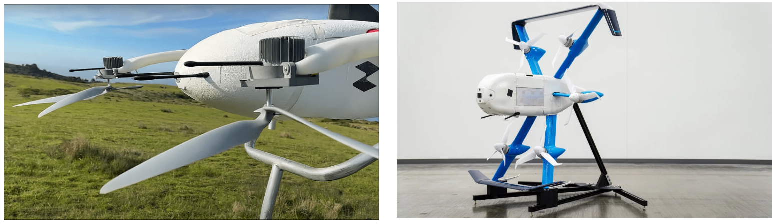

(a) (b)

Figure 1.2: sUAS configurations: a) Zipline Platfrom 2 drone and b) MK30 drone by Prime Air

in this new class of electric aircraft. When compared to fixed-wing aerodynamics, rotor aerodynamics is considerably more complex. The dynamic loading on the rotors, flow interaction effects among the blades as well as between other rotors, aeroelastic response, and unsteady aerodynamics collectively result in a complex flow-field [8]. Furthermore, the aerodynamics of rotors impact the thrust and power requirements of these vehicles. Additionally, these intricate flow interactions in rotors also directly influence the noise generated by them, significantly contributing to the overall acoustic signature of these vehicles [93]. To expedite innovation in the design and development of this advanced rotorcraft technology, it is crucial to gain a deeper understanding of the fundamental flow physics governing isolated rotor operation.

1.1.1 Aerodynamics of eVTOL and sUAS rotors

The flow regime for rotors are usually characterized in terms of two non-dimensional parameters: tip Mach number and Reynolds number at 75% chord and are defined as:

$$M_{tip} \;=\; \frac{\Omega\ R}{a_\infty}, \quad Re_c\ (0.75\ R) \;=\; \frac{\rho_\infty\ \Omega\ (0.75R)\ c}{\mu_\infty} \tag{1.1}$$

where, R is the radius of the rotor, Ω is the rotational speed, c is the chord at the 75% span location. A crucial distinction concerning rotors in eVTOLs and sUAS vehicles is that, unlike conventional rotorcraft, they typically operate in very different flow regimes. Due to the reliance on distributed propulsion in eVTOLs and sUAS vehicles, they facilitate the use of smaller-sized rotors capable of operating at lower tip speeds [93]. This brings down the tip Mach number to a range of $0.15 \leq M_{tip} \leq 0.3$ and Reynolds number to the range of $10^4 - 10^5$, in comparison to the conventional rotors where M_{tip} ranges between $0.7 \leq M_{tip} \leq 0.8$ and $Re_c \sim 10^6$ [131]. The high Reynolds number regimes that conventional rotorcraft operate in tend to encounter a fully turbulent flow. However, in the low Reynolds number operating regime, various flow complexities arise. Boundary layer phenomena such as laminar separation, transition, and reattachment of the flow become more prominent in these cases. Due to this low Reynolds number operating regime of the eVTOL and sUAS rotors, they will be collectively referred to as '*low-Re rotors*' for the remainder of this document.

One commonly occurring low Reynolds number phenomenon observed in the boundary layer of lifting surfaces, such as wings and rotors, is the formation of laminar separation bubbles. In Figure 1.3(a), we observe the separation of the laminar boundary layer under an adverse

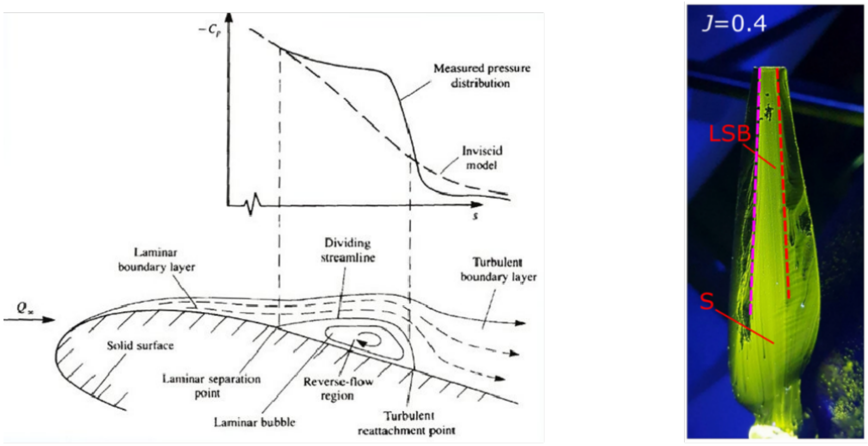

(a)

(b)

Figure 1.3: (a) Laminar Separation Bubble (LSB) on an airfoil surface and its impact on the surface pressure distribution [50] (b) Oil flow visualization of over the suction side of the rotor blade showing the occurrence of the LSB [40].

pressure gradient over an airfoil. Subsequently, due to freestream turbulence and the curvature of the body, the separated boundary layer reattaches, forming a laminar separation bubble (LSB). It is seen that the surface pressure distribution is influenced by the LSB, which in turn affects the lift and drag characteristics of the airfoil. Several computational and experimental studies on low-*Re* airfoils have highlighted the sensitivity of their performance to Reynolds number variations and complex boundary layer physics. These studies have revealed the presence of small to large laminar separation bubbles (LSBs), transition phenomena, laminar separation, and vortex shedding. [6, 35, 66, 95, 124].

In the context of eVTOL and sUAS applications, studies have looked into global performance characteristics of isolated rotors [7, 77, 86] as well as full-scale vehicles [94] operating under low Reynolds number regimes. Brandt and Selig [7] conducted an experiment to assess the performance of various sUAS rotors at different Reynolds numbers. They observed a reduction in the propellers' performance as the Reynolds number decreased. This decrease was attributed to Reynolds effects, which are typically not observed in large-scale rotors. Similary, Ol et al. [86] conduceted wind tunnel tests for a range of propellers and concluded that the scatter observed in the thrust versus advance ratio for small diameter propellers was attributable to Reynolds number effects. Intaratep et al. [45] conducted tests on the full-scale DJI Phantom quadcopter in an anechoic wind tunnel using various off-the-shelf rotor geometries with the same diameters. In their aerodynamic analysis they found that in spite of operating at largely similar Reynolds number regimes, the rotors exhibited very different aerodynamic performance. They concluded that small-scale rotors tend to depend largely on the rotor geometry and configuration and are controlled by small scale aerodynamics. The efforts in most of these studies were geared towards characterizing the rotor performance based on geometry, rotor configuration, and operating conditions. However, it wasn't clear what low-Re phenomena influenced this behavior in these rotors. Detailed rotor studies focusing on capturing low-Re phenomena within the boundary layer remain scarce. This scarcity is due to significant challenges encountered in both experimental and computational analyses in adequately capturing these intricate effects. To bridge that gap, recently Grande et al. [40, 41] carried out oil flow visualizations and PIV measurements on a modified APC-96 propeller to analyze the flow near the rotor wall at various operating conditions and captured the occurrence of a laminar separation bubble on the rotor surface. Figure 1.3(b) shows the oil flow visualization over the propeller surface, wherein the region with oil accumulation (green region marked as LSB) shows the laminar separation bubble. Their experiment also demonstrated that with decreasing advance ratio, the effective angle of attack at blade sections increases. Consequently, this movement of the effective angle of attack upstream of the chord also reduces the size of the separation bubble. Additionally, the separation of the laminar boundary layer can lead to vortex shedding at different frequencies depending on the advance ratio. This goes to show the prevalence of the complex boundary layer phenomena in these rotors that in turn impact their aerodynamic performance.

1.1.2 Influence of Low-Re Aerodynamics on Rotor Acoustics

Aerodynamically generated rotor noise can be broadly classified into deterministic and non-deterministic noise sources as shown in figure 1.4 [42]. The tonal noise components comprise of deterministic components which can be due to steady or unsteady sources. The steady loading and thickness noise caused due to the periodic sweep of the blade . The thickness noise is a function of the blade geometry and rotation rate and is therefore easily predictable. It radiates primarily in the rotor disk plane. The loading noise radiates along the axis of rotation down to observers on the ground in rotorcraft configurations. Therefore, it is critical to accurately model the spanwise distribution of the blade loading. This is particularly complicated at low-Re as these propellers are more susceptible to separation and transition effects which significantly influence the mean blade lift. Blade Vortex interaction (BVI) noise is another important tonal noise source which is an impulse caused by the interaction of the blade with shed vortices, whose strengths and positions are known, making it deterministic. There is an additional tonal noise source called the high-speed impulse noise which is observed in conventional rotors with high tip speeds but is absent in low-Re rotors.

The blade interactions with self-generated and incident turbulence causes unsteady fluid dynamics which is stochastic in nature and hence, non-deterministic. Turbulence ingestion noise (TIN) arises from the unsteady blade loading caused due to the interaction of the rotor leading edge with incident turbulence. It can produce both narrow-band as well as broadband spectral features. Within confined spaces and closed anechoic chambers, the flow recirculation tends to produce narrow spectral features and impacting the higher harmonics. This is not a true representation of an isolated rotor in hover, but a result of the experimental conditions and hence, care needs to be taken to ensure recirculation does not impact noise measurements in confined spaces [43, 105]. When the blade leading edge interacts with the turbulent wake shed by a previous blade, it is referred to as Blade-Wake Interaction (BWI)

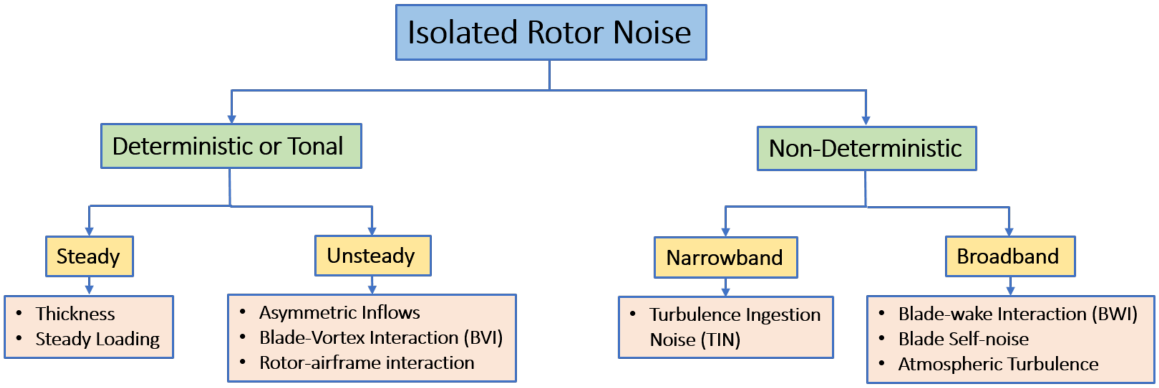

Figure 1.4: Classification of isolated rotor noise, adapted from [42, 120]

noise. It results in broad spectral features in the mid to high-frequency range due to the different scales of turbulent eddies present in the wake [9]. Finally, blade self-noise is a high-frequency broadband noise source caused due to the scattering of the turbulence pressure field resulting from the passage of turbulence over the trailing edge of the blade [10, 59]. It is predominantly influenced by boundary layer phenomena close to the trailing edge [11]. This can be categorized into five types based on the noise generating mechanisms [10, 11]:

- turbulent boundary layer flow over the trailing edge (TBL-TE),
- boundary layer separation due to the onset of stall at high angles of attack (TBL-A)
- vortex shedding due to laminar boundary layer separation (LBL-VS)
- vortex shedding due to bluntness at the trailing edge (TEB-VS) and
- formation and shedding of the tip vortex (TVF)

Studies have shown that both tonal and broadband noise are important for sUAS and eVTOL rotorcraft applications [93, 119]. In an effort to evaluate the individual contribution of different noise sources, Whelchel et al. separated the measured tonal and broadband noise components using a phase-averaging technique [119]. Their work showed that noise produced by isolated low-*Re* rotors at the blade passage frequency (BPF) is dominated by tonal sources but the higher harmonics can be attributed to broadband interactions. Broadband noise was shown to contribute significantly to the total measured far field noise. Moreover, in the context of rotors used in eVTOL and sUAS applications, self-noise has been demonstrated to be significant concerning human ear sensitivity.In the acoustic measurements conducted by Intaratep et al. [45], it was observed that rotor geometries with the same diameters exhibited significant differences in mid to high frequency noise, whereas differences in low frequency noise were less pronounced. This underscores the importance of self-noise in the rotors that were tested. Additionally, other studies investigating the acoustics of low Reynolds number rotors have also found that self-noise tends to increase with the number of rotors, rotational speed, and can vary throughout a single rotor revolution.[37, 40, 87, 131]. These observations highlight the significance of self-noise, a component largely influenced by boundary layer phenomena. Consequently, further detailed study of mechanisms influencing self-noise becomes imperative, making it one of the focal points of the current study.

1.1.3 Current State of Computational Methods for Low-*Re* Rotors

Aerodynamic Modeling

Computational techniques for modeling flow around rotors can be broadly categorized into different fidelity levels based on the computational time required by each method and the amount of physics modeled [21]. Current low-fidelity methods typically model the blade rather than resolving its geometry to predict the aerodynamic performance. The actuator disk theory is the simplest method used to analyze rotor performance [60, 106]. It follows the principles of momentum theory, wherein an infinitely thin disk, modelled as a pressure discontinuity induces a constant velocity along the rotation axis. Since it doesn't require any information of the blade geometry, it can estimate the performance characteristics in a matter of seconds. However, this method is limited by the simplistic assumptions and cannot model complex aerodynamic effects accurately [106]. Other popularly used low-fidelity methods include the Blade Element Theory (BET) and Blade Element Momentum Theory (BEMT) [60]. In the former approach, the blade is divided into different spanwise sections, and aerodynamic forces are estimated under the assumption that each section behaves as a lifting surface. These forces are integrated across the span to give the net aerodynamic performance of the rotor. The latter is an extended version of BET which incorporates momentum theory, providing more information on the induced flow. Efforts to enhance the Blade Element Momentum Theory (BEMT) method have yielded promising results by incorporating corrections for top loss, Mach effects, three-dimensionality, wake effects, and Reynolds effects [63, 70]. However, these methods fail at modeling the complex and intricate aerodynamic effects effects observed in a rotor. They further lose out in accuracy when it comes to small-diameter rotors due to significant Reynolds effects [86].

On the other end of the spectrum of computational models, high-fidelity techniques completely resolve the blade geometry. Conventional Computational Fluid Dynamics (CFD) methods fall under this category. CFD methods can be further categorized based on the amount of turbulence resolved [3]. Direct Numerical Simulation (DNS), as the name suggests, solves the Navier-Stokes equations directly without any simplifying assumptions, making it the most accurate method. This approach is capable of resolving turbulence down to the smallest scale. However, this comes at a huge cost since the grid requirements for this method increase exponentially with the Reynolds number, limiting the method to very low Reynolds number applications. Large Eddy Simulation (LES) is a method which resolves the large scales of turbulence and models the small eddies. It using spatial filtering to separate the eddies and uses sub-grid scale models to model small eddies. Even though this method is comparatively cheaper than DNS, it is still limited by Reynolds number. It becomes especially expensive for wall bounded flows where cost of resolving the near wall region is high.

The cheapest turbulence modeling method is the Reynolds Average Navier Stokes (RANS) Simulations. A Reynolds decomposition is performed to separate the mean and fluctuating components. In this method, only the mean flow is modeled and no turbulence is actually resolved. However, for most engineering applications, this approximation of the flow is sufficient to understand the underlying aerodynamics. RANS simulations make use of turbulence models that vary based on how accurately the Reynolds stress is resolved and are formulated using extensive empirical data. When the mean flow exhibits periodic variations or unsteadiness over long periods of time, the Unsteady Reynolds-Averaged Navier-Stokes (URANS) method can be applied.

A fourth category in CFD methods that is popular in the rotorcraft community is the hybrid RANS/LES method. It applies LES in the free-stream or in regions with large separation and RANS near the wall [4, 110]. DES and its variants [103] are some of the common hybrid RANS/LES methods which are capable of resolving large scales of turbulence in the wake and separated regions of a rotor. Finally, it is important to acknowledge the recent and promising rise in the use of the Lattice Boltzmann Method (LBM) for simulating fluid flows. [15, 16, 51]. The method is capable of resolving different scales of turbulence while keeping computational costs significantly low [5]. However, since most commercial or open-source fluid simulation software are Navier-Stokes based solvers, this method is not yet widely accessible to many researchers.

There have been multiple high-fidelity studies carried out for sUAS and eVTOL applications. Yoon et al. [130] analyze an isolated rotor as well as different multi-copter configurations using the Spalart-Allmaras (SA) based DDES model to emphasize the importance of interactional aerodynamics. Diaz et al. [114] performed a similar high-fidelity CFD analysis on different commercially available multi-copters in forward flight and suggested design modifications to improve their efficiency. Mankbadi et al [67] carry out an in-depth analysis of the DJI Phantom 3 isolated rotor using the SA-DDES model as well. The study was carried out to identify the different regions on the blade that could contribute to overall noise. However, all the afore-mentioned studies use an underlying fully-turbulent model. It has been shown that using a transition based RANS model in a hybrid RANS/LES framework is essential for flows that encounter transition [132]. Although, hybrid models with a base RANS transition model are difficult to implement due to difficulties encountered in blending the RANS and LES zones [34]. Further, Thai et al. [109] studied the difference between a URANS simulation and a DES simulation. There were noticeable differences when it came to the resolution in the wake and its interaction with the rotor, but not enough to affect the prediction of the aerodynamic performance.

There have also been plenty isolated rotor studies using the URANS approach [54, 64, 88, 108, 109]. Lakshminarayan and Baeder [54] analyze an sUAS rotor under hover conditions with different leading and trailing edge geometries. They address the deficiency of the fully turbulent model in estimating power accurately. Thai et al. [108] conducted a comparative analysis of the fully turbulent Spalart Allmaras model and its transition model variants and concluded that transition models did not provide an added advantage to the estimation of thrust and figure of merit. However, the study did not look into flow conditions beyond hover. They also did not investigate deeper into the near-wall flow to understand the behavior of the models. Recently, a first-of-its-kind study investigated the differences between streamline and crossflow transition models for two different rotors [46]. The transition location predicted by the transition models matched well with the experimental measurements. However, the predictions saw large errors in the predicted thrust and sufficient justification for the over-prediction was not provided.

Using a URANS framework, the current study aims to fill the knowledge gap in current literature regarding the holistic influence of transition models on rotor aerodynamic performance. The study aims to place equal emphasis on global performance metrics such as thrust and torque, while also delving deep into analyzing flow parameters like transition and separation characteristics at the wall since these factors are known to have a significant impact on rotor performance, as explained in Section 1.1.1.

Aeroacoustic Modeling

To model the sound generated due to flow, Computational Aeroacoustics (CAA) simulations must account for the disparate scales and requirements imposed by both fluid dynamic and acoustic simulations. Acoustic perturbations are inherently unsteady with magnitudes generally much smaller than flow perturbations and length scales which are larger. Additionally, the frequency range of interest is generally very broad which creates stringent resolution requirements [107]. The typical approaches used to compute noise are: 1) the direct CFD approach and 2) the acoustic analogy approach [118]. Direct CFD approach is where the flow and acoustics are solved together using compressible Navier-Stokes equations and applied when there is a two-way coupling between noise and flow [5]. It requires a very refined computational domain that can represent the flow and acoustics well which makes it computationally demanding. The acoustic analogy is a method where the flow and acoustic calculations are decoupled [33]. This is where the Ffowcs-Williams and Hawkings (FW-H) equation comes into play [123]. The flow calculation is performed first (either using low fidelity methods like potential flow solvers or high fidelity methods like CFD) and then fed into FW-H equation to compute noise propagation. The most salient feature of acoustic analogy is that it does not involve any approximations and hence is an exact formulation.

Thus, the onus lies on the flow computation to ensure the accuracy of the noise prediction, underscoring the need for accurate aerodynamic models.

Due to the computational limitations of the direct approach, most of current literature has adopted the acoustic analogy approach. Zawodny at al. [131] used the DES model on the OverFLOW solver for the flow solution, while used the popular PSU-WOPWOP acoustic tool for noise prediction [8]. Predictions made by the high-fidelity CFD set-up was also compared with a BEMT based method. The blade passage frequency (BPF) and its first harmonic were studied, wherein both methods showed comparable performance at the BPF tone, while the high-fidelity model showed slightly better predictions at the first harmonic. Information beyond the second tone wasn't presented in their work. Mankbadi et al. [68] conducted a comparative analysis of permeable and impermeable surface predictions of noise for an isolated rotor using OpenFOAM, in conjunction with an acoustic tool introduced by UniCFDLab [31]. They observed that permeable calculations improved prediction accuracy but exhibited a similar trend to other studies, with deteriorating prediction accuracy after the first harmonic. Further, the accuracy of the acoustic solution tends to be very sensitive to the placement of the permeable surface and can sometimes even lead to spurious signals [65, 111]. Other studies with different CFD set-ups also saw similar behavior in prediction accuracy of tonal noise [92, 111]. It can be safely concluded that with the existing popular CFD methods, prediction of high frequency deterministic noise and broadband noise is not feasible. This could be attributed to the lack of sufficient resolution of turbulence scales that tend to affect the higher harmonics in the acoustic spectra [119].

For broadband noise predition, most researchers have resorted to employing semi-empirical models. More specifically, there has been a lot of effort in modeling the self-noise component of broadband noise. A widely popular broadband noise framework is the UCD-QuietFly, introduced by Li and Lee [62]. Using a combination of BEMT and XFOIL analysis, the aerodynamic and boundary layer parameters for different spanwise sections are estimated, which is then fed into an empirical wall pressure spectrum [58]. The wall pressure spectrum is plugged in the analytical formulation for trailing edge noise [98], that has been modified to include blade twist angle, collective pitch angle, flapping angle, azimuthal angle, sectional radius, and rotor tilt angle. Multiple works have used this method in estimating broadband noise for varying flight conditions [69, 96, 111, 125] and have shown promising results. However, the method was initially developed with the assumption of a fully turbulent boundary layer and therefore, only incorporated those effects in their trailing edge noise model. In a subsequent publication, Li and Lee [61] incorporated the effects of laminar boundary layer vortex shedding (LBL-VS) noise. However, they acknowledged that prior knowledge of experimental data was necessary to tune certain parameters in the model, which could be challenging.

Another well-known broadband noise model is the Brooks Pope and Marcolini (BPM) method which was initially introduced by Brooks et al. [10] for an airfoil and then extended by Burley and Casey [11] to predict helicopter noise. It is a semi-empirical model formulated using boundary layer data derived from NACA0012 airfoil at a wide range of Reynolds numbers and angles of attack. The method models all five components of self-noise described in Section 1.1.2 and therefore is of interest to the current work. BPM method was initially introduced for predicting helicopter noise but has been adopted by the sUAS and eVTOL community in the recent past [49, 87, 120, 131]. However, rotors in this application space have largely different geometric profiles compared to NACA0012, which the BPM model was initially scaled on [49, 131]. A straightforward solution to this issue was proposed by Jung et al. [49], where they suggested inputting boundary layer data obtained from 2-D (RANS) simulations conducted on various spanwise sections into the BPM model. Their calculation using the DJI 9443 CF propeller exhibited good agreement with experimental data. This methodology will be adopted in the current work. The current work aims to adopt this method to study the influence of the different low-Re boundary layer phenomena on blade self-noise.

1.2 Problem Statement

To summarize the above discussion, sUAS and eVTOL rotors are significantly affected by boundary layer phenomena such as laminar separation, transition, and reattachment. Computational models aimed at predicting the performance of these rotors must carefully consider these effects to ensure accurate predictions. This also needs to be achieved without large computational expenses, so that it can easily translate to industrial applications. Further, these boundary layer mechanisms have shown to impact the high frequency broadband noise or self-noise emitted by the rotors. Hence, a noise prediction methodology needs to be developed that can leverage the flow predictions made by an efficient computational model and reflect those effects in the acoustic spectra. This will help in understanding different rotor noise sources in greater depth, thereby, paving the path for noise mitigation technology and other innovative rotor design ideas.

"The current work aims to establish a robust computational framework capable of modeling low-Re boundary layer phenomena, so as to predict the complex aerodynamics of a rotor and its impact on noise, while maintaining computational efficiency."

To accomplish this objective, specific tasks were undertaken which essentially encompass the contributions of the current study and are discussed in the following section.

1.3 Contributions

- To tackle the issue of modeling low-Re flows, a novel transition turbulence model, SSG/LRR-ω-γ has been proposed. The model framework uses a Reynolds stress transport model, SSG/LRR-ω, as the base turbulence formulation and is coupled with Menter's γ transition model. The proposed model uses simplified correlations that do not depend on freestream quantities, making it coordinate independent and rendering it Galilean invariant. Additionally, using a second-order closure turbulence model makes it suitable for complex flow-fields. A validation study of the model revealed that the proposed approach performed equivalently or even better than existing state-of-the-art transition models for different transition phenomena.

- Further, the turbulence model was extended to include crossflow transition. The modification to the original model formulation was made by adding a term to the intermittency production that accounts for crossflow transition. The RST-based transition model consistently exhibited good accuracy and was able to better capture regions where crossflow and natural transition occur simultaneously compared to other existing crossflow transition models.

- The proposed transition model was applied to different low-Re UAV rotors and it was seen that the model was able to predict the aerodynamic performance characteristics with good accuracy. A comparative study with existing state-of-the-art RANS turbulence models of varying orders of fidelity was carried out. The comparative study represents a pioneering effort, evaluating the models based on their prediction accuracy for both global performance metrics and the prediction of transition and separation phenomena.

- A RANS-CFD-based blade self-noise prediction method was developed using the BPM formulation, incorporating boundary layer parameters derived from 2D-RANS simulations. The investigation explored the impact of utilizing both fully turbulent and transition turbulence models within the broadband noise prediction framework. Furthermore, an assessment comparing the CFD-based methods with lower-fidelity approaches, such as XFOIL, was conducted. This comprehensive effort not only shed light on the effectiveness of various computational methods in estimating blade self-noise but also revealed their respective limitations.

- Finally, a design case study for swept rotors has been conducted. Utilizing the predictive capabilities of the established computational framework, the aerodynamic characteristics of the swept rotor were thoroughly analyzed. Experimental studies have indicated that the swept propeller demonstrates reduced broadband noise compared to its unswept counterpart at low advance ratios. The computational aerodynamic and acoustic analysis aimed to further investigate the factors contributing to this lower acoustic signature.

1.4 Thesis Outline

- **CHAPTER 2**: This chapter includes the theory behind flow transition and explains how it can be numerically modelled. The evolution of transition models has also been presented along with brief descriptions of existing state-of-the-art transition turbulence models.
- **CHAPTER 3**: Here, the novel SSG/LRR-ω-γ model formulation is introduced, along with a discussion on the various canonical cases used to validate the model. Furthermore, the predictions of the model are compared against existing transition models for different modes of transition. Additionally, the chapter includes the crossflow exten-

sion implemented for the proposed model, accompanied by its corresponding validation cases.

- **CHAPTER 4**: The computational methods used for the application of low-*Re* rotors is detailed in this chapter. Details on grid generation and the complete CFD set-up using OpenFOAM is discussed. Further, the detailed methodology for the fast broadband noise prediction framework is explained.
- **CHAPTER 5**: This chapter presents the aerodynamic analysis of two rotor test cases: Delft-APC Propeller and T-Motor 30x10 CF Propeller. Both the geometries have pre-existing experimental data against which the established model framework is validated. Predictive capabilities of five different RANS transition turbulence models are assessed. The models were compared on the basis of global thrust and torque, skin friction coefficient over the blade surface, and boundary layer parameters. The analysis also gave insight into the behavior of rotors at varying operating conditions.
- **CHAPTER 6**: This chapter presents the aeroacoustic analysis of the rotors discussed in the previous chapter. It includes both tonal and broadband noise predictions made by a fully turbulent model and the proposed transition model for both propellers considered in the previous chapter. The chapter mainly focuses on assessing the numerical efficiency of different computational methods in providing an approximate prediction of the blade self-noise spectra.
- **CHAPTER 7** : The final chapter includes a design study where the current computational framework is used to analyze the effects of sweep on rotor aerodynamics and acoustics. The chapter presents the established computational analysis techniques to analyze the influence of sweep.

Chapter 2

Principles of Flow Transition and Modeling Techniques

This chapter provides a brief overview of the physics behind low-Reynolds number flows. It then discusses existing transition modeling techniques, highlighting the current state-of-the-art. The advantages and disadvantages of these methods are examined to ultimately motivate the transition turbulence model proposed in this study.

2.1 Physics of Low-Reynolds Number Flows

At low Reynolds numbers, flows are subjected to higher viscous effects which lead to instabilities in the boundary layer. These instabilities manifest in different forms, resulting in different modes of laminar to turbulent transition. These include : natural, bypass, separation, wake-induced transition and crossflow transition.

Natural transition is observed when a body encounters low free-stream turbulence ($< 1\%$) and the laminar boundary layer starts to destabilize due to acoustic or viscous disturbances. In 1947, Schubauer and Skramstad [100] proved the existence of two-dimensional Tollmein-Schlichting waves which are caused by viscous instabilities in a laminar boundary layer. These instabilities grow at a gradual pace and eventually transition to turbulent flow. A detailed depiction of this process is illustrated in Fig. 2.1a. By-pass transition on the other hand, is observed when the free-stream turbulence levels are high enough ($> 1\%$), such that the first three stages shown in Fig. 2.1a are “by-passed” to form turbulent spots which then coalesce to form the turbulent boundary layer. A special instance of the bypass transition that occurs in turbomachniery flows is the wake-induced transition. It occurs when the wake impinges on the laminar boundary layers. However, this mechanism is not analyzed in this study.

Separation-induced transition is observed in low to moderate free-stream turbulence conditions with an adverse pressure gradient. Under these conditions, the laminar boundary layer separates and the free-shear layer experiences instabilities which leads to generation of spanwise vortices that convect downstream and breakdown. The increased mixing associated with turbulence as well as the momentum transfer toward the wall induced by the large scale coherent structures forces reattachment, thus forming a bubble. Figure 2.1b indicates that the surface pressure distribution is significantly altered which in this case gives the airfoil an apparent camber. This can influence the airfoil performance characteristics and hence, it is important that this effect is captured accurately.

The final mode of transition addressed in this study is the crossflow-transition. This is observed in fully three-dimensional flows like swept wings or rotor blades. In these cases the spanwise flow component is known to generate instabilities in the laminar boundary layer, which results in three-dimensional transition, or crossflow transition. An illustration of this phenomena is shown in figure 2.1c.

2.2 Modeling Transitional Flows

Laminar to turbulent flow transition prediction has been one of the most challenging tasks in turbulence modeling. The difficulty in modeling a physics-informed framework to predict

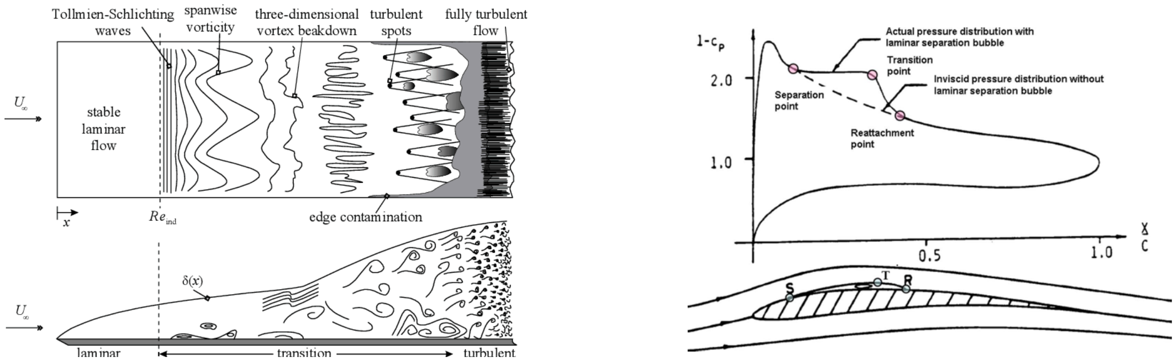

(a) Natural and Bypass transition mechanism [97]

(b) Effects of sepatation-induced transition on C_p distribution [95]

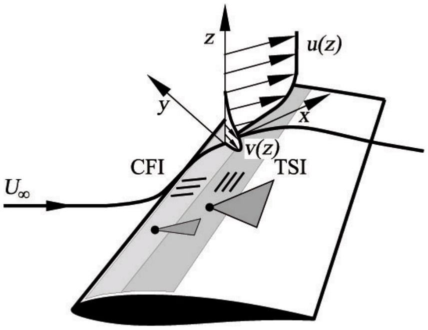

(c) Crossflow Effects in the boundary layer of a three-dimensional flow over a wing

Figure 2.1: Illustration of different transition mechanisms

transition arises due to the combined linear and non-linear instabilities that result in varied mechanisms of transition discussed above.

Over the past few decades, various techniques have been formulated to predict transition. The e^N method from Van Ingen [113] and Smith and Gamberoni [101] is a commonly used linear stability model implemented in the popular coupled viscous-inviscid panel method XFOIL [26, 27]. The e^N method is subject to a number of limitations when extended to complex 3-dimensional flows. The method requires apriori knowledge of the geometry and grid. While examples exist of three-dimensional boundary layer predictions using this model [28], the need for coupling with a high fidelity boundary layer code and inability to predict bypass transition limits its utility with modern CFD codes. Researchers have also explored more direct modeling techniques like Direct Numerical Simulation (DNS) and highly resolved Large Eddy Simulations (LES) [78, 127, 128] which were successful in accurately predicting transition. However, these methods are computationally very expensive and hence are not practical to be widely used for many engineering applications in the foreseeable future.

In an effort to overcome this issue, researchers turned to modeling transitional flows using the Reynolds Averaged Navier-Stokes (RANS) equation. RANS-based methods are computationally less expensive compared to the LES and DNS methods mentioned earlier. Equation (2.1) gives the RANS governing equations,

$$\begin{aligned} \frac{\partial U_i}{\partial x_i} &= 0 \\ \rho\frac{\partial U_i}{\partial t} + \rho U_j\frac{\partial U_i}{\partial x_j} &= -\frac{\partial p}{\partial x_i} + \frac{\partial}{\partial x_j}(2\mu S_{ij} - \rho\overline{u_i^{'}u_j^{'}}) \end{aligned} \tag{2.1}$$

wherein, the Reynolds stress tensor term ($\rho R_{ij} = \rho\overline{u_i^{'}u_j^{'}}$) is modelled to close this system of equations [3]. Most commonly, this term is modelled using the Boussinesq approximation, given in equation (2.2). It assumes that the turbulent stress is linearly proportional to the mean strain rate (S_{ij}).

$$\overline{u_i^{'}u_j^{'}} = 2\nu_t S_{ij} - \frac{2}{3}k\delta_{ij} \tag{2.2}$$

In the above equation, ν_t stands for turbulent eddy viscosity, which represents the apparent viscosity due to turbulent eddies. The second term on the right hand side is included to ensure that contracting the Reynolds stress gives the Turbulent Kinetic Energy (TKE), represented as k below. Models that follow the Boussinesq approximation are known as linear eddy viscosity models. Some commonly used fully turbulent linear eddy viscosity models are Spalart Allmaras (SA) [102], k-ϵ [17], k-ω [122] and k-ω SST [74] models.

Generally, RANS models are formulated using transport equations of mean turbulent flow quantities. To model transition, some additional quantities are used in the model framework. Menter et. al introduced the k-ω SST-based transition model that uses the 'Local-Correlation Based Transition Modeling (LCTM)' method [56, 72, 73]. In addition to the turbulence quantities of TKE (k) and dissipation rate (ω) that govern the production and dissipation of turbulence respectively, the model uses intermittency (γ) and transition momentum thickness Reynolds number ($Re_{\theta t}$) as the transport variables that govern the transition mechanism. The principle is that when the vorticity Reynolds number (Re_{ν}) exceeds $Re_{\theta t}$ based on a set transition criteria, γ is produced indicating the onset of transition. The effects of the free-stream turbulence is incorporated into the model by the transport equation for $Re_{\theta t}$ and in turn manifests in the empirical correlations for the transition length and onset criteria. However, this results in a lack of Galilean invariance, which implies that it is applicable only to cases with stationary walls and subsequently dependent on non-local variables. To overcome this drawback and to further simplify the formulation, Menter et al. came up with a modified transition model a few years later [76]. This method is also based on LCTM modeling, albeit with only γ. By eliminating dependence on the velocity vector contained in the correlations for $Re_{\theta t}$, the model formulation is rendered Galilean invariant. Both models introduced by Menter are coupled with the k-ω SST [74] turbulence model by scaling the production and dissipation terms of kinetic energy transport equation with γ. Validation studies using the LCTM concept show that it is capable of predicting transition in engineering flows [79, 129].

Alternate approaches to LCTM have also been studied and one prominent example is the 'physics-based' Laminar Kinetic Energy model (k-kl model) introduced by Walters and Leylek [117] and Walters and Cokljat [116]. This formulation is linked with the Wilcox k-ω [2, 122] model and uses only one additional transport equation that models the effects of laminar fluctuations. This model was able to capture different transition mechanisms well, however, it inherited sensitivity to free-stream boundary conditions from the k-ω model [75]. Additionally, it uses a complex formulation which makes it difficult to adjust to other turbulence models [76]. The other alternative that has been studied is to use algebraic models. Cakmakcioglu, et al., [12] introduced a Spalart-Allmaras framework based transition model which uses an algebraic expression for intermittency as a function of transport variables from the SA model. Initially, the γ expression was formulated with a lack of Galielean invariance and also as a function of free-stream Reynolds number which introduced a non-unique reference length scale. These issues were later rectified to form the current SA-BCM model [13, 81]. The modified intermittency, γ_{BC}, is multiplied with the production term in the SA equation which suppresses the turbulence until the transition criteria is met. The transition criteria used, $Re_\nu > Re_{\theta c}$, is the same as most transition models. Although this method showed promising results in predicting the transition location, the fully turbulent region properties were not as accurately predicted compared to other models for the cases examined in the study and additionally, since it depends on the Spalart-Allmaras framework, its applicability is restricted to simpler aerodynamic flows. The current work however, does not focus on the algebraic or physics-based modeling methods, instead, solely focuses on modeling based on transport equations.

All transition models discussed so far have been based on linear eddy viscosity model frameworks, which rely on the Boussinesq approximation as mentioned earlier. However, this approximation tends to fail when it comes to flows over curved surfaces or strong streamline curvature, flows with sudden changes in mean strain rate, rotating flows or highly three dimensional flows. These are important cases for aerodynamic applications and hence need to be modelled accurately. This drawback is overcome by implementing models that directly model the turbulent stress tensor, R_{ij} and this class of models are called Reynolds stress models (RSMs). Since there are no simplifying assumptions made for R_{ij}, these models are capable of modeling both isotropic and anisotropic components of the turbulent stress tensor, thereby, providing a fuller representation of the actual flow. Some of the commonly used Reynolds stress transport-based models (RSTMs) are the Launder-Reece-Rodi model [57] and the Speziale-Sarkar-Gatski (SSG) [104] model. Similar to the $k-\omega$ SST model [74], Eisfeld et al., [29, 30] introduced a model, SSG/LRR-ω, combining the SSG for freestream regions and LRR for near-wall regions using the same blending function given by Menter [74]. Recently, this fully turbulent RSTM was coupled with the γ-$Re_{\theta t}$ transition model by Nie et al., [82] to give the SSG/LRR-ω-γ-$Re_{\theta t}$ model. It was tested for different flat-plate cases, 2-D airfoil and 3-D spheroid cases and performed as well as, if not better, than the SST-based γ-$Re_{\theta t}$ model. However, due to its dependence on the transition Reynolds number $Re_{\theta t}$, it lacks Galilean invariance. Additionally, the model correlations are adopted from the SST-based γ-$Re_{\theta t}$ model which involves iterative methods to solve for the transition Reynolds number , $Re_{\theta t}$, resulting in a complex formulation.

Historically, transition models have been developed with formulations that can predict streamwise transition phenomena like natural, bypass and separation induced transition first. Subsequently, the models have been modified in later iterations to account for crossflow transition. This can be attributed to the fact that modeling crossflow transition is a lot more challenging due to its complex three-dimensional nature. For geometries like underwater vehicles, low-speed airships and aircraft, experiencing complex 3D flows in the boundary layer, there is a significant amount of crossflow velocity that can cause a yawing effect and a favorable pressure gradient leading to an earlier transition than TS-instability. Therefore, it is important that the transition turbulence model capture these crossflow transition effects.

There have been multiple works aimed at extending the SST-based γ-$Re_{\theta t}$ to include crossflow transition effects [18, 38, 39, 55, 71]. A semi-local approach was introduced by Grabe et al. [38], and Medida et al. [71], around the same time which showed promising results. However, these methods were dependent on the geometry and coordinate system. Later, to overcome this drawback, Langtry presented a new crossflow transition model that was based on the local helicity criteria [55, 80], since helicity was discovered as a major contributor to the crossflow velocity gradient. The formulation also included roughness effects. Grabe et al., presented a comparison between their fully local C1-based formulation and helicity-based formulation [39]. It was concluded that the helicity-based model is more widely applicable to multiple geometries compared to the local C1 approach that is more suitable for wing-like geometries. On a similar note, the SST-based γ transition model was extended to include crossflow formulation by Pillai et al. [112]. It also employed the helicity-based formulation to account for crossflow transition and included the effects of surface roughness in its formulation. It was validated using multiple test cases that showed good agreement with experimental data. In the higher-order transition models, Nie et al extended the RSTM-based γ-$Re_{\theta t}$ model to include crossflow effects which showed better transition prediction when compared to its SST-based counterpart [83].

The current work aims at combining the advantages of a higher order RST-based model and the simplified γ transition formulation to accurately predict different transition mechanisms, including crossflow transition. The detailed description of the proposed model formulation and validation cases are given in chapter 3.

Chapter 3

Development and Validation of SSG/LRR-ω-γ Transition Model

This chapter discusses the formulation and validation of the novel SSG/LRR-ω-γ transition turbulence model [90]. It also includes the extension of the proposed model to include crossflow transition, accompanied with corresponding validation cases.

The proposed model aims at overcoming the shortages in γ-$Re_{\theta t}$ RSTM by adopting the ideas introduced by Menter et al., [76] for the one equation model. The formulation for the new model is simplified by eliminating any dependency on transition Reynolds number, $Re_{\theta t}$, which in turn eliminates dependency on free-stream variables like turbulence intensity and additionally, reduces the complexity of the model since the correlations that depend on $Re_{\theta t}$ are removed. This is achieved by coupling the SSG/LRR-ω model with a modified one equation γ model that is formulated based on local quantities within the boundary layer. Therefore, the second-order closure turbulence model makes the new model applicable to complex flow-fields and the independence from free-stream quantities makes it Galilean invariant, giving it an upper-hand compared to existing linear eddy viscosity based and RSTM based transition models. The complete formulation of the SSG/LRR-ω-γ model is given in Section 3.1 with details on modified correlations described in Section 3.2. Subsequently, the model formulation to include crossflow transition is given in Setion 3.3. A grid sensitivity analysis of the model is presented in Section 3.4, followed by various canonical cases on which the model has been validated. The proposed model was implemented on OpenFOAM-v2006 and has been publicly shared on github.

3.1 Formulation of the SSG/LRR-ω-γ Model

3.1.1 SSG/LLR-ω Reynolds Stress Model

The transport equation for Reynolds stress tensor in the SSG/LRR-ω model is given by (3.1). The model correlations and constants for this transport equation are unchanged from the formulation presented by Eisfeld et al. [30].

$$\frac{\partial \rho R_{ij}}{\partial t} + \frac{\partial (\rho U_k R_{ij})}{\partial x_k} = \rho P_{ij} + \rho \Pi_{ij} - \rho \epsilon_{ij} + \rho D_{ij} \tag{3.1}$$

where $R_{ij} = u_i u_j$ represents the Cartesian components of the Reynolds stress tensor, ρ is the density and μ is the dynamic viscosity of the fluid. The Reynolds stress production term P_{ij} is given by (3.2). There is no modeling required for this term as information regarding velocity gradient and Reynolds stress tensor is available from the system of equations and thereby, give the exact value.

$$\rho P_{ij} = -\rho R_{ik} \frac{\partial U_j}{\partial x_k} - \rho R_{jk} \frac{\partial U_i}{\partial x_k} \tag{3.2}$$

The remaining three terms in the Reynolds stress transport equation, ϵ_{ij}, D_{ij} and Π_{ij}, are modeled based on mathematical relations which hold true for both SSG and LRR models. The only difference between the two will be in the model coefficients which are calculated based on a blending function adopted from Menter's SST model [74].

Dissipation, ϵ_{ij} is given by (3.3). It is modeled as the isotropic component of specific dissipation rate which in turn is calculated using the transport equation given in (3.7)

$$\rho\epsilon_{ij} = \frac{2}{3}\rho\epsilon\delta_{ij}; \qquad \epsilon = C_\mu k\omega \tag{3.3}$$

where, $C_\mu = 0.09$ and $k = R_{ii}/2$ is the kinetic energy. Diffusion of the Reynolds stress tensor, D_{ij}, is modeled using generalized gradient diffusion (GGD) introduced by Daley and Harlow [25] and is given by (3.4).

$$\rho D_{ij} = \frac{\partial}{\partial x_k}\left[\left(\mu\delta_{kl} + D^{(GD)}\frac{\rho R_{kl}}{C_\mu\omega}\right)\frac{\partial R_{ij}}{\partial x_l}\right] \tag{3.4}$$

The pressure strain term , Π_{ij}, which is specific to Reynolds stress transport equation is applied to redistribute the turbulent stresses. It is given by (3.5).

$$\begin{aligned}\rho\Pi_{ij} = &-\left(C_1\rho\epsilon + \frac{1}{2}C_1^*\rho P_{kk}\right)b_{ij} + C_2\rho\epsilon\left(b_{ik}b_{kj} - \frac{1}{3}b_{kl}b_{kl}\delta_{ij}\right) + \left(C_3 - C_3^*\sqrt{b_{kl}b_{kl}}\right)\rho k S_{ij}^* \\ &+ C_4\rho k\left(b_{ik}S_{jk} + b_{jk}S_{ik} - \frac{2}{3}b_{kl}S_{kl}\delta_{ij}\right) + C_5\rho k\left(b_{ik}W_{jk} + b_{jk}W_{ik}\right)\end{aligned} \tag{3.5}$$

where, b_{ij}, S_{ij} and W_{ij} are Cartesian components of the anisotropic tensor, mean strain rate tensor and vorticity tensor respectively. S_{ij}^* is the deviatoric component of the mean strain rate tensor. The constants C_{1-5} are the same as given in [30]. P_{kk} is the trace of the production term, P_{ij}.

$$b_{ij} = \frac{R_{ij}}{2k} - \frac{1}{3}\delta_{ij}, \quad S_{ij} = \frac{1}{2}\left(\frac{\partial U_i}{\partial x_j} + \frac{\partial U_j}{\partial x_i}\right), \quad S_{ij}^* = S_{ij} - \frac{1}{3}S_{kk}\delta_{ij}, \quad W_{ij} = \frac{1}{2}\left(\frac{\partial U_i}{\partial x_j} - \frac{\partial U_j}{\partial x_i}\right) \tag{3.6}$$

The specific dissipation transport equation, also known as length scale determining equation is used to calculate the isotropic dissipation rate, ϵ. The production term which is a function of the trace of the Reynolds stress production, the dissipation, diffusion and cross-diffusion terms are given in (3.7).

$$\frac{\partial(\rho\omega)}{\partial t} + \frac{\partial(\rho U_k \omega)}{\partial x_k} = \frac{\alpha_\omega \omega}{k}\frac{\rho P_{kk}}{2} - \beta\rho\omega^2 + \frac{\partial}{\partial x_k}\left[\left(\mu + \sigma_\omega \frac{\rho k}{\omega}\right)\frac{\partial \omega}{\partial x_k}\right] + \sigma_d \frac{\rho}{\omega} max\left(\frac{\partial k}{\partial x_j}\frac{\partial \omega}{\partial x_j}, 0\right) \tag{3.7}$$

All the model coefficients encountered so far are blended using Menter's SST blending function, F_1, [74] and is calculated as

$$\phi = F_1 \phi_{LRR} + (1 - F_1)\phi_{SSG} \tag{3.8}$$

where, ϕ_{LRR} represents the LRR model coefficients and are applied in the near wall regions ($F_1 = 1$) and ϕ_{SSG} represents the SSG model coefficients which are applied beyond the edge of the boundary layer ($F_1 = 0$).The values of the coefficients are equal to the ones given in Eisfeld et al. [30].

3.1.2 γ Transition Model

The γ transition model [76] is governed by the intermittency transport equation (Eq. (3.9)). All the model correlations and constants for this transport equation are taken from the one-equation transition model formulation presented by Menter et al [76].

$$\frac{\partial(\rho\gamma)}{\partial t} + \frac{\partial(\rho U_j \gamma)}{\partial x_j} = P_\gamma - E_\gamma + \frac{\partial}{\partial x_j}\left[\left(\mu + \frac{\mu_t}{\sigma_\gamma}\right)\frac{\partial \gamma}{\partial x_j}\right] \tag{3.9}$$

where σ_γ is a model constant equal to 1. The source term for transition is defined by

$$P_\gamma = F_{length}\rho S\gamma(1-\gamma)F_{onset} \tag{3.10}$$

where, F_{length} is used to control the magnitude of the production term and is set to 100. It was a correlation function of $Re_{\theta t}$ in the $\gamma - Re_{\theta t}$ SST [56] and RSM [82] models, however, is a constant for the one-equation transition model introduced by Menter et al. [76]. The term S is the magnitude of strain rate and '$(1-\gamma)$' is used to limit the value of intermittency to 1. This is done to ensure that intermittency does not exceed the freestream value, which is set to 1 [73]. F_{onset} is an important term that is responsible for the triggering of transition mechanism which indicates the onset of intermittency production. It is set off when the vorticity Reynolds number exceeds the set transition criteria (Eq.(3.25)).

$$\begin{gathered} F_{onset1} = \frac{Re_{\nu}}{2.2Re_{\theta c}}, \qquad F_{onset2} = min(F_{onset1}, 2.0) \\ F_{onset3} = max\left(1 - \left(\frac{R_T}{3.5}\right)^3, 0\right), \qquad F_{onset} = max(F_{onset2} - F_{onset3}, 0) \end{gathered} \tag{3.11}$$

where, $Re_{\nu} = \frac{\rho y^2 S}{\mu}$ is the vorticity Reynolds number and R_T is the viscosity ratio. The term $Re_{\theta c}$ is the critical Reynolds number and is the point where the intermittency begins to rise and turbulence begins to grow. Similar to the model variable F_{length}, $Re_{\theta c}$ was also modeled as a correlation function of $Re_{\theta t}$. However, in the one-equation transition model [76], this dependency was eliminated and was modeled as a function of local turbulence intensity and pressure gradient. The correlation for $Re_{\theta c}$ is taken from [76].

The dissipation term, E_{γ}, ensures that the intermittency stays close to zero in the laminar boundary layer regions and is given by Eq. (3.12)

$$E_{\gamma} = c_{a2}\rho\Omega\gamma F_{turb}(c_{e2}\gamma - 1) \tag{3.12}$$

c_{a2} and c_{e2} are model constants equal to 0.06 and 50 respectively. Ω is the absolute vorticity magnitude. F_{turb} is responsible to turn off dissipation in turbulent regions and in the viscous sublayer and its expression is given in [76].

The γ transition model includes a modification to the original blending function (F_{1orig}) introduced by Menter et al [73, 74], given by Eq.(3.13), which consistently sets the value of F_1 equal to 1 in the laminar region. This is to ensure that the near wall LRR turbulence model remains active in laminar, transition and turbulent regions in the boundary layer.

$$R_y = \frac{\rho y \sqrt{k}}{\mu} \quad , \quad F_3 = e^{-\left(\frac{R_y}{120}\right)^8} \quad , \quad F_1 = \max(F_{1orig.}, F_3) \tag{3.13}$$

3.1.3 Coupling γ Transition Model with SSG/LRR-ω

The Reynolds stress model, SSG/LRR-ω, and the intermittency transport equation, γ, are coupled by scaling the production, dissipation and pressure strain terms of the Reynolds stress transport equation with γ (3.14). This is similar to the approach introduced by Nie et al [82] where the SSG/LRR-ω was coupled with the two equation γ-$Re_{\theta t}$ transition model. Due to the low values of intermittency ($\gamma \approx 0$) in the laminar regions, scaling production with γ ensures very low levels of turbulent Reynolds stresses. In the laminar region, the coupling enables the destruction to be larger than turbulent production and low levels of pressure-strain term prevents re-distribution of turbulent stresses. On the other hand, intermittency is equal to 1 in turbulent regions, resulting in the model to resume its fully turbulent behavior.

$$\tilde{P}_{ij} = \gamma P_{ij} \quad , \quad \tilde{\Pi}_{ij} = \gamma \Pi_{ij} \quad , \quad \tilde{\epsilon}_{ij} = \max(\gamma, 0.1)\epsilon_{ij} \tag{3.14}$$

3.2 Modifications to the SSG/LRR-ω-γ Model

The following section details the modifications made to the model formulation, in order to make it adaptable to all transition mechanisms and improve its prediction capabilities, while preserving all other correlations. In particular, the changes have been made to the production terms for Reynolds stress and specific dissipation rate.

3.2.1 Auxiliary production term for separated flows

In cases with low levels of freestream turbulence, that generally result in natural or separation-induced transition, it was observed that the SSG/LRR-ω model takes longer to produce turbulence inside the boundary layer, despite the transition being triggered at the right location. This effect was also observed in the SST model and therefore, to improve the transition prediction in flows with low freestream turbulence intensity, a scalar supplementary turbulence production term P_k^{lim} (Eq. (3.15)) was introduced by Menter et al. [76]. In the current formulation, this supplementary term is modified to be a scalar function of P_{kk}, which is the trace of the diagonal of the Reynolds stress production term, P_{ij}. This aids in generating additional turbulence when the transition is driven by laminar separation, or by TS wave growth. The auxiliary term is activated when transition is triggered and deactivated once the transition process is complete.

$$P_{ij}^{lim} = 5C_k max(\gamma - 0.2, 0)(1-\gamma)F_{on}^{lim} max(3C_{SEP}\nu - \nu_T, 0)\frac{\omega}{k}P_{kk}\delta_{ij} \tag{3.15}$$

$$\tilde{P}_{ij} = \gamma P_{ij} + P_{ij}^{lim} \tag{3.16}$$

The onset term F_{on}^{lim} is given by (Eq. (3.17)). The constant C_k controls the magnitude of supplementary turbulence production and is equal to 1. The constant C_{SEP}, which is set to 1, is responsible to deactivate the supplementary term when the magnitude of turbulent viscosity goes higher than three times the kinematic viscosity.

$$F_{lim}^{on} = \min\left(\max\left(\frac{Re_V}{2.2Re_{\theta_C}^{lim}} - 1, 0\right), 3\right) \quad , \quad Re_{\theta_c}^{lim} = 1100 \tag{3.17}$$

Figure 3.1 shows that the transition predicted by the original formulation is initiated way downstream due to the delayed production of turbulence within the boundary layer. On the other hand, the addition of the auxiliary production term results in adequate levels of turbulence production to initiate transition at the right position.

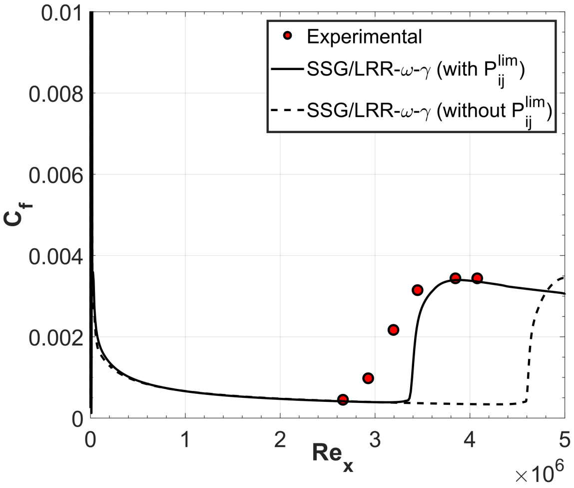

Figure 3.1: Comparison of skin friction coefficient, C_f, predicted by the original and modified formulation for the SK-flat plate case [99] exhibiting natural transition with $Tu = 0.03\%$

3.2.2 Modification of the ω transport equation

In their implementation of the SSG/LRR-ω model coupled to γ-$Re_{\theta t}$ transition model, Nie et. al [82] observed that the production of specific dissipation rate, P_ω, calculated using the original formulation (Eq. (3.18)), was very low in laminar regions. This is the result of P_ω being a function of Reynolds stress production, which in turn is scaled using intermittency, γ. Since γ has negligible values in the laminar region, the dissipation produced is also low. This results in a faster growth rate of turbulence and pre-mature flow transition. This effect is depicted in Fig. 3.2a (dashed curve) which shows a pre-mature peak in the specific dissipation rate for the original formulation given by the following equation.

$$P_{\omega_{RSM}} = \frac{\alpha_\omega \omega}{k} \frac{\rho P_{kk}}{2} \tag{3.18}$$

On the other hand, the drawback of low levels of turbulent dissipation does not affect the $k - \omega$ SST based transition models. This is because the production of specific dissipation rate, even though originally is a function of Reynolds stress, in this case is a function of mean strain rate (Eq. (3.19)) which is a direct consequence of the Boussinesq approximation (Eq. (3.20)).

$$P_{\omega_{SST}} = \frac{\alpha_\omega}{\nu_t} \left(-\rho R_{ik} \frac{\partial U_i}{\partial x_k} \right) = \alpha_\omega \rho S^2 \tag{3.19}$$

$$R_{ij} = - \left(\ 2\nu_t S_{ij} - 2k\delta_{ij}/3 \ \right) \tag{3.20}$$

Nie et al [82] introduced a hybridized form of the production of specific dissipation rate that uses a blending function which activates the SST production term in laminar regions and RSM production term in turbulent regions. The current formulation also introduces a hybrid production term, $P_{\omega_{RSM,hybrid}}$, given as:

$$P_{\omega_{RSM,hybrid}} \ = \ (1 \ - \ C_{lam}) P_{\omega_{SST}} \ + \ C_{lam} P_{\omega_{RSM}} \tag{3.21}$$

The blending function, C_{lam} was originally formulated as a function of $Re_{\theta t}$ and γ by Nie et al [82]. Since the current model does not have information on $Re_{\theta t}$, the blending function has been modified to be a function of critical Reynolds number, $Re_{\theta c}$ instead, as given in

Eq. (3.22).

$$C_{lam} = \begin{cases} 0 & \text{if } c_\omega > \gamma \\ \frac{\gamma - c_\omega}{1 - c_\omega} & \text{if } c_\omega < \gamma \end{cases} \quad \text{and} \quad c_\omega = \left(\exp\left(- \left(\frac{420}{Re_{\theta c} + C_{Re}} \right)^4 \right) \right)^2 \tag{3.22}$$

$$C_{Re} = 500$$

Critical Reynolds number ($Re_{\theta c}$) is defined as the point at which turbulence first starts to grow and intermittency begins to increase while transition Reynolds number is the point at which velocity begins to deviate from its laminar profile, skin friction coefficient begins to increase and is an indication of the onset of transition. $Re_{\theta c}$ is generally encountered upstream of $Re_{\theta t}$ since the instability needs to develop to appreciable levels before changing from laminar to turbulent profiles [73]. Therefore, it was hypothesized that the blending function presented by Nie et al. will hold good for the current model, provided the transition Reynolds number is replaced by the critical Reynolds number plus a value that would account for the difference between the two. The constant C_{Re} was tuned to make up for this difference. In figure 3.2b, the dotted line indicating the modified equation shows a good agreement with experimental data, thereby, confirming the validity of the hypothesis.

Figure 3.2a also shows the trend in the dissipation rate when the auxiliary production term, P_{ij}^{lim} is added to the original (dash-dot curve) and modified (solid curve) formulation of dissipation rate. In the former case, since the primary purpose of P_{ij}^{lim} is to produce additional turbulence, the onset of turbulence gets pushed way upstream when adequate amounts of dissipation in laminar regions is lacking. Subsequently, Fig. 3.2b shows the distribution of skin friction coefficient where the transition, that is originally observed around mid-way through the flat plate gets pushed way upstream due to high levels of turbulence and low levels of dissipation. On the other hand, the final form of the current formulation, which

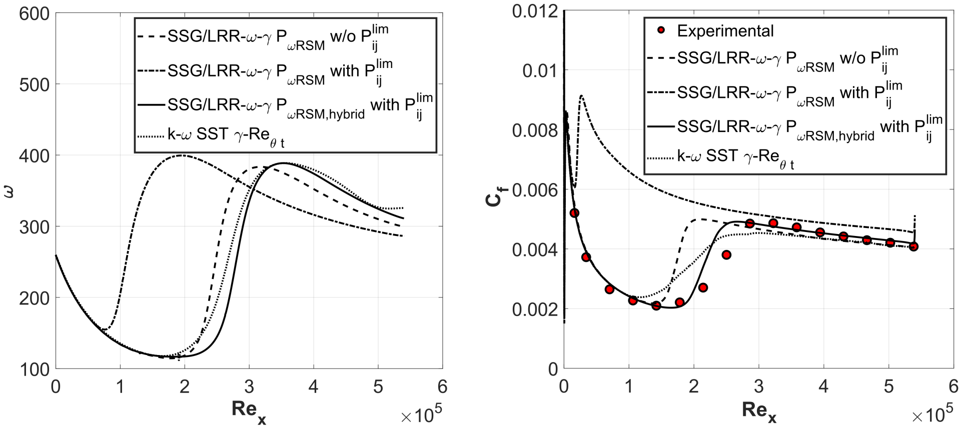

(a) (b)

Figure 3.2: Specific dissipation rate distribution, ω (a) and skin friction coefficient distribution, C_f (b) along the length of the T3A flat plate [23]

includes the modified formulation for dissipation rate and the auxiliary production term, balances the turbulence and dissipation production, thereby achieving a good prediction in transition when compared to experimental data.

3.3 Extension for crossflow Transition

In order to incorporate effects of crossflow transition, the only term that needs to be altered from the original SSG/LRR-ω-γ formulation is the production of intermittency in eqn. (3.9). The γ-production term is modified by adding a crossflow production term as given in eqn.(3.23).

$$\rho P_\gamma = \rho P_{\gamma,sw} + \rho P_{\gamma,cf} \tag{3.23}$$

where, the subscript sw represents streamwise terms and cf represents crossflow terms. The streamwise intermittency production is the same as the original SSG/LRR-ω-γ model and is given in eqn. (3.24)

$$\rho P_{\gamma,sw} = F_{length,sw} \rho S \gamma (1-\gamma) F_{onset,sw} \tag{3.24}$$

where, the term $F_{length,sw}$ represents the length of transition and is set to 100. S represents the magnitude of the mean strain rate tensor and '(1-γ)' is used to limit the value of intermittency from exceeding 1. The term $F_{onset,sw}$ controls the transition onset location and is given in eqn. (3.25).

$$\begin{gathered} F_{onset1,sw} = \frac{Re_{\nu}}{2.2 Re_{\theta c}}, \qquad F_{onset2,sw} = min(F_{onset1,sw}, 2.0) \\ F_{onset3,sw} = max\left(1 - \left(\frac{R_T}{3}\right)^3, 0\right), \qquad F_{onset,sw} = max(F_{onset2,sw} - F_{onset3,sw}, 0) \end{gathered} \tag{3.25}$$

where, $Re_{\theta c}$ is the critical Reynolds number and is modeled as a function of the local turbulence intensity and pressure gradient. The detailed correlation is given in [76]. The term R_T represents the viscosity ratio ($\frac{\rho k}{\mu \omega} = \frac{\nu_t}{\nu}$).

Similar to the streamwise production, the crossflow production is given in eqn. (3.26). It is based on the local helicity approach introduced by Grabe et al. [39],

$$\rho P_{\gamma,cf} = F_{length,cf} \rho S \gamma (1 - \gamma) F_{onset,cf} \tag{3.26}$$

Here, $F_{length,cf}$ is set to a constant value of 5. The term $F_{onset,cf}$ controls the onset of crossflow transition. The criteria to determine this onset location depends on the local helicity Reynolds number, Re_{He}, which is a good indicator to detect crossflow instabilities as it is a function of crossflow velocity gradients [39, 83]. It plays a similar role to the vorticity Reynolds number, Re_v , which detects the onset of instabilities in streamwise transition formulations and is a function of streamwise velocity gradients.

$$Re_{He} = \frac{y^2}{\nu} \frac{He}{|u_k|} \qquad He = |u_k \cdot (\nabla \times u_k)| \tag{3.27}$$

$$F_{onset1,cf} = \frac{Re_{He}}{Re_{He,C}} \quad , \quad F_{onset2,cf} = \min(F_{onset1}, 2.0)$$
$$F_{onset3,cf} = \max\left(1 - \left(\frac{R_T}{3}\right)^3, 0\right) \quad , \quad F_{onset,cf} = \max(F_{onset2} - F_{onset3}, 0) \tag{3.28}$$

where, He is the local helicity which is determined by taking the dot product between the local velocity (u_k) and vorticity vectors. A drawback of using quantities like helicity is that it makes the model coordinate dependent. This results in the crossflow formulation losing the Galilean invariant property which was originally present in the streamwise formulation.

The correlation for $Re_{He,C}$ is given as a function of shape factor, H, as shown in eqn. (3.29).

$$Re_{He,C} = 0.55 \max(-456.83H + 1337.2, 150.0) \tag{3.29}$$

The shape factor is further calculated using a correlation introduced by Cliquet et al [20]. It is modeled as a function of the local pressure gradient parameter, λ, which is easily available from the γ transition model:

$$H(\lambda_{\theta L}) = 4.02923 - \sqrt{-8838.4\lambda^4 + 1105.1\lambda^3 - 67.96\lambda^2 + 17.574\lambda + 2.0593} \tag{3.30}$$

For the sake of clarity, in the following sections, the streamwise model will simply be referred to as SSG/LRR-ω-γ, while the crossflow model will be indicated with a suffix "CF": SSG/LRR-ω-γ-CF.

3.4 Grid Sensitivity and Numerical Setup

Different turbulence models exhibit different grid sensitivities. Therefore, to understand how the current model responds to changes in grid parameters, a systematic grid sensitivity study was conducted. Computational meshes for the test cases were generated with the commercial CFD software Star-CCM+ and imported into OpenFOAM. The meshes consisted of polyhedral cells with prism layers near walls to resolve the boundary layer. For two dimensional cases, the geometries were extruded in the spanwise direction with a single cell resolution. All the test cases were solved using a transient solver with numerical schemes that were first-order in time and second-order in space. Gradient limiters were introduced to improve the stability of the Reynolds stress model. All boundary conditions are calculated according to the method specified for SSG/LRR-ω model in the NASA turbulence modeling repository [1]. In all the cases, velocity is set to a no-slip condition at the wall. Intermittency is initialized to be 1 throughout the domain indicating a fully turbulent flow initially.

Since the focus of the current study is to capture transition and near-wall behavior of the flow, boundary layer grid parameters like streamwise resolution, number of prism layers and near-wall spacing were considered. The test case chosen for the analysis was the S-K flat plate test case [99]. Figure 3.3a presents the effect of streamwise spacing on the transition prediction. The location of flow transition was set as the point where the skin friction coefficient, C_f, shows a sharp change in its gradient. Interestingly, the transition location moves downstream as the spacing decreases and achieves independence for a grid with 300 points in the streamwise direction. Figure 3.3b shows the clear influence the number of prism layers have on the transition prediction. Prism layer resolution is defined as the number of grid points required in the wall-normal direction to resolve the boundary layer and values of $25, 50$ and 75 were tested for the current analysis. It is important to note that N_y in Fig. 3.3 denotes the number of prism layers and not the total number of cells in the wall-normal direction within the domain. It was seen that the coarser meshes seemed to predict transition way downstream. This is due to the fact that lower resolutions in the wall normal direction can lead to a poor estimation of the velocity gradient which in turn results in an underestimation of the vorticity Reynolds number ($Re_v = \frac{\rho y^2 S}{\mu}$). The prism layer and streamwise spacing analyses were done using meshes that maintained a $y^+(1)$ value of 1. To further study the effects of near-wall spacing, multiple $y^+(1)$ values required to resolve the viscous sublayer were tested as shown in Fig. 3.3c. The transition prediction was not largely affected by changes in the resolution in the viscous sublayer, however, the approximation in the fully turbulent region was greatly improved with a lower $y^+(1)$ as is shown in the zoomed in window of Fig. 3.3c.

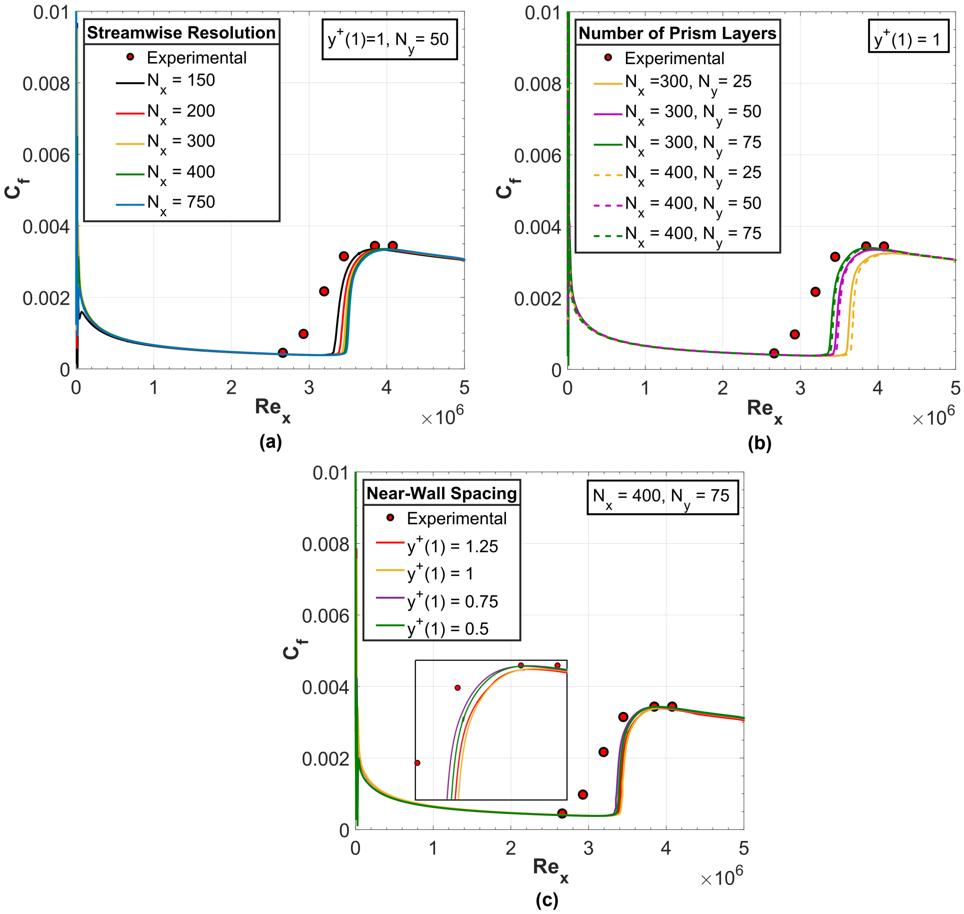

Figure 3.3: Grid sensitivity study conducted on the SK-flat plate undergoing natural transition. a) Effect of streamwise spacing, b) Effect of number of prism layers and c) Effect of near-wall spacing on the skin friction coefficient of the flat plate.

From the grid sensitivity study, it can be concluded that the model is most influenced by wall normal resolution and is an important grid parameter in approximating the transition accurately. The model is not too sensitive to near-wall spacing to predict transition, however, is important to resolve the turbulent boundary layer more accurately. Additionally, a considerable resolution in the streamwise direction is also desired. Furthermore, for all test cases, thin boundary layer theory was used to 1) calculate the boundary layer thickness to get an estimate of the desired total prism layer thickness, and 2) to calculate the near wall spacing of the first cell to maintain a $y^+(1) = 1$. Doing this ensures a fair practice in grid generation near the wall.

3.5 SSG/LRR-ω-γ Model Validation Cases

The SSG/LRR-ω-γ transition model was validated using multiple test cases, each representing different modes of transition. The benchmark flat plate cases, Schubauer-Klebanoff (S-K) for natural transition [99] and the ERCOFTAC (European Reseach Community on Flow, Turbulence and Combustion) T3 series for bypass transition [23] were chosen. To test the capability of the model in predicting laminar separation induced transition, the NACA-0018 airfoil was studied at two different Reynolds numbers [35]. Finally, a three-dimensional wing which also exhibited laminar separation induced transition was analysed and compared with experimental data taken from Bastedo et al [6].

3.5.1 Benchmark Flat Plate Cases

Flat plate boundary layers with zero pressure gradient were simulated with the current model to examine the model performance compared to experiments typically used to calibrate transition models. The flow parameters for the flat plate test cases are given in table 3.1.

The geometry considered for all the cases had a plate length of 1.5m with a leading edge radius of 0.75mm as given in Menter et al. [73]. The inlet was placed 0.2m ahead of the flat plate leading edge. The height of the domain was set to 0.75m since this dimension gave the least degree of non-orthogonality in the mesh.

Table 3.1: Inlet conditions for flat plate cases

Case	**S-K (1)**	**S-K (2)**	**T3A**	**T3B**	**T3A-**
Inlet Velocity (m/s)	50.1	50.1	5.4	9.4	19.8
Reynolds Number (Re)	$5\ \times 10^6$	$5\ \times 10^6$	5.4×10^5	9.4×10^5	1.98×10^6
freestream Tu (%)	0.03	0.18	3.3	6.2	0.9
Viscosity ratio (ν_t/ν)	1	1	12	90	8

S-K Flat Plate

The S-K flat plate case, taken from the experiment conducted by Schubauer and Klebanoff [99] in 1955, exhibits natural transition. The mesh obtained from the grid-independence study was used, with a near-wall spacing set to $d = 6 \times 10^{-6}$ m such that it corresponds to $y^+(1) = 0.75$. Transition prediction at two different inlet freestream turbulence intensities, $Tu = 0.03\%$ (S-K(1)) and $Tu = 0.18\%$ (S-K(2)) (listed in table 3.1) were tested. Figure 3.4a presents a comparative study of the two in-flow conditions for different transition turbulence models. The $k-\omega$ SST γ and SSG/LRR-ω-γ exhibit negligible sensitivity to any changes in the freestream conditions. This can be attributed to the formulation of the two models which entirely depend on local values. On the other hand, the $k-\omega$ SST γ-$Re_{\theta t}$ model exhibits large sensitivity to change in freestream conditions since the correlations used to predict transition largely depend on the freestream turbulence intensity. Additionally, the RSM based SSG/LRR-ω-γ is able to predict the behaviour in the turbulent region better than the other two SST based transition models.

T3-Series Flat Plates

The freestream conditions for T3-series flat plates given in table 3.1 were taken from the ERCOFTAC experimental flat plate cases [23]. The table suggests that all the T3-series flat plates experience fairly high freestream turbulence intensities which leads to bypass transition. The transition point moves downstream as the turbulence intensity decreases. Figures 3.4b, 3.4c and 3.4d show a good agreement of the current model with experimental data. For the T3A (fig. 3.4b) and T3B (fig. 3.4c) cases, the turbulent region values are approximated by SSG/LRR-ω-γ more accurately compared to other transition models. The point of transition, that is the point where the slope of the skin friction coefficient begins to increase, is predicted well for T3A and T3A- (fig. 3.4d) compared to the other two transition models which tend to predict it upstream of the actual point.

3.5.2 NACA 0018 Airfoil Case

For most practical design purposes, transition triggered by laminar separation bubbles are of much higher interest. Modeling the behavior of flows with laminar separation induced transition includes capturing the locations of laminar separation, transition, and turbulent reattachment. The current study looks at the NACA 0018 airfoil subjected to flow at low Reynolds numbers. The geometry and mesh for the airfoil is shown in Fig. 3.5.

Gerakopulos et al. [35] studied the behavior of laminar separations on a NACA 0018 airfoil section, at a range of Reynolds numbers and angles of attack. Reynolds numbers of 80,000 and 140,000 and angles of attack (α) of 2^0, 6^0, and 10^0 were selected in this study. The freestream turbulence intensity measured in the experiment was less than 0.3% and the

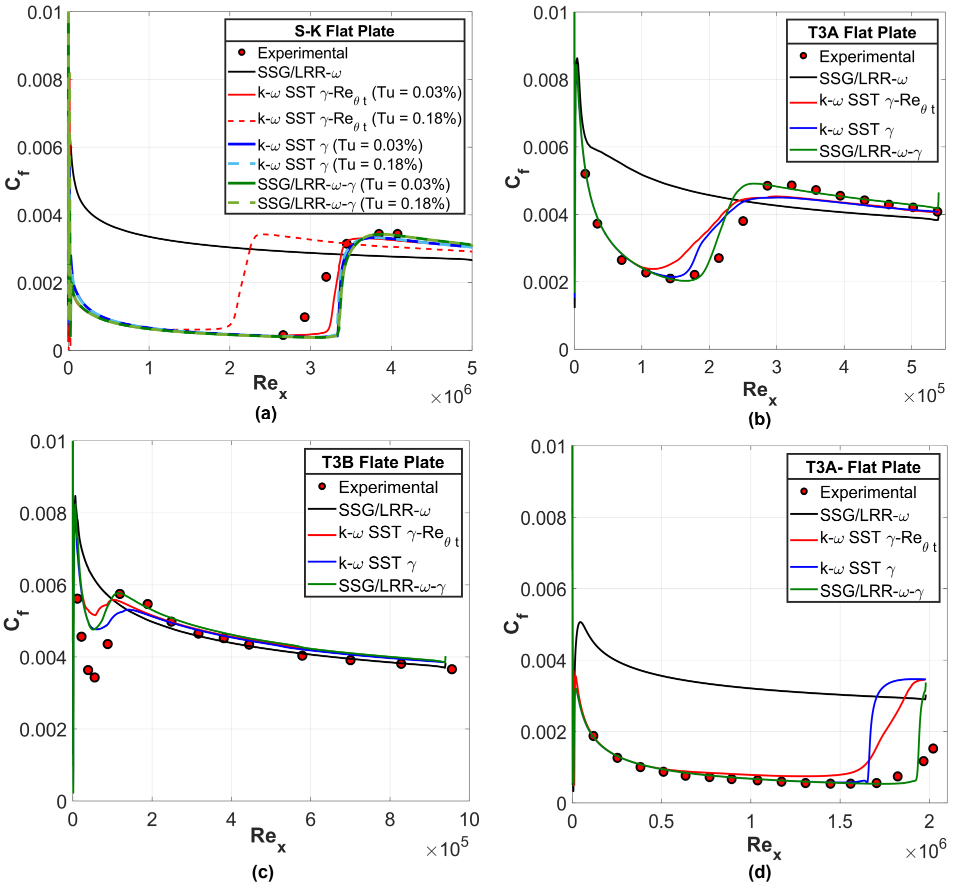

Figure 3.4: Comparison of C_f predicted by different turbulence models for benchmark flat plate cases

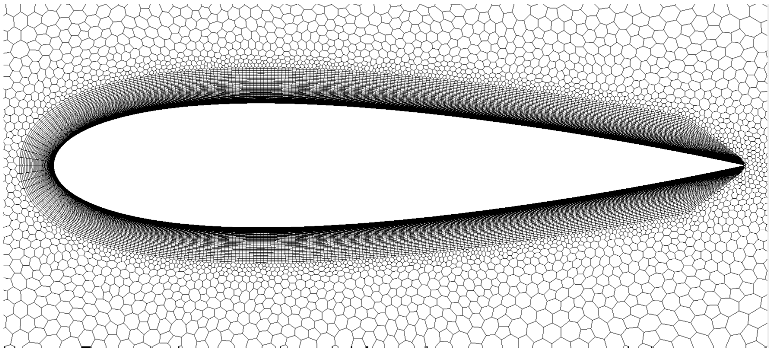

Figure 3.5: Computational mesh for NACA-0018 airfoil (complete domain not displayed for clarity)

initial conditions for the simulation were set accordingly. A fine grid with a near-wall $y^+(1)$ of 0.4 and a 75 prism layers was chosen for the analysis.

Figures 3.6 and 3.7 present the distribution of coefficient of pressure for Reynolds number equal to 80,000 and 140,000 at different angles of attack. The letter 'S' in the figure denotes the point where laminar separation occurs in the flow, 'T' represents the point where laminar to turbulent transition begins and 'R' denotes the point where turbulent re-attachment occurs. The laminar separation bubble, defined by the region between 'S' and 'R', is seen to move upstream as the angle of attack and Reynolds number increase. The size of the bubble, indicated by the length between the separation and reattachment points, tends to decrease as the angle of attack and Reynolds number increase. The proposed model seems to consistently predict this behavior accurately for all cases. The coefficient of pressure in the turbulent region as well as the laminar region is well approximated by the current model compared to other transition models. The performance of the $k-\omega$ SST γ-$Re_{\theta t}$ is comparatively better for the higher Reynolds number case (fig. 3.7). A similar trend was observed for the $k-\omega$ SST γ model as well, however, it had lower accuracy for the low angle of attack in the $Re = 140,000$ case (fig. 3.7a). The current model on the other hand, performs well for both higher and lower Reynolds numbers. Additionally, it can be observed that the RSM based fully turbulent model, SSG/LRR-ω, is able to predict laminar separation in the flow at higher angles of attack (figs. 3.6b, 3.6c, 3.7b and 3.7c). However, the transition and reattachment are not well predicted as the model formulation is not equipped to predict transition.

Figure 3.8 presents the velocity contours of the case where $Re = 140,000$ and $\alpha = 6^0$. This case was chosen to study the effect of the laminar separation bubble on flow properties. The figure compares the velocity contours for the fully turbulent SSG/LRR-ω model with the current model. Figure 3.8b clearly indicates the laminar separation bubble, represented by streamlines curling up and and the presence of a recirculation zone (indicated in blue). This is absent in the fully turbulent case. The flow separates at around 20% of the chord and

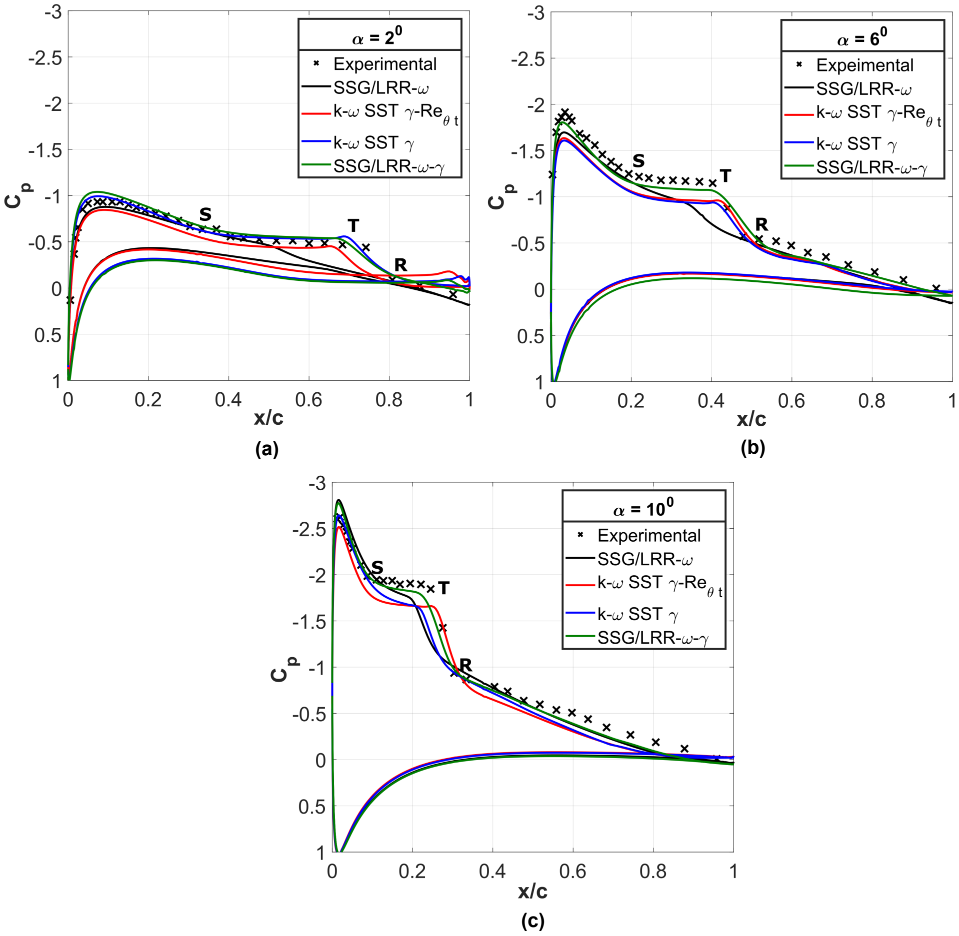

Figure 3.6: Comparison of C_p distribution predicted by different turbulence models at $\alpha = 2^0, 6^0, 10^0$ and Re = 80,000 for NACA-0018. S - Separation point; T - Transition point; R - Reattachment point

reattaches at a little beyond 40% of the chord. This is in direct agreement with the C_p plot for this case (Fig. 3.7b). Figure 3.9 gives the corresponding distribution of skin friction coefficient predicted by the fully turbulent model and the proposed transition model for the same case as in Fig. 3.8. Figure 3.9b indicates the point where skin friction coefficient goes negative as the location where laminar separation occurs and the point where it goes back to a positive value as the location where reattachment occurs. The point where the slope of the C_f curve turns positive is indicative of the beginning of flow transition. This is in good agreement with its corresponding velocity contour (Fig. 3.8b) and pressure distribution

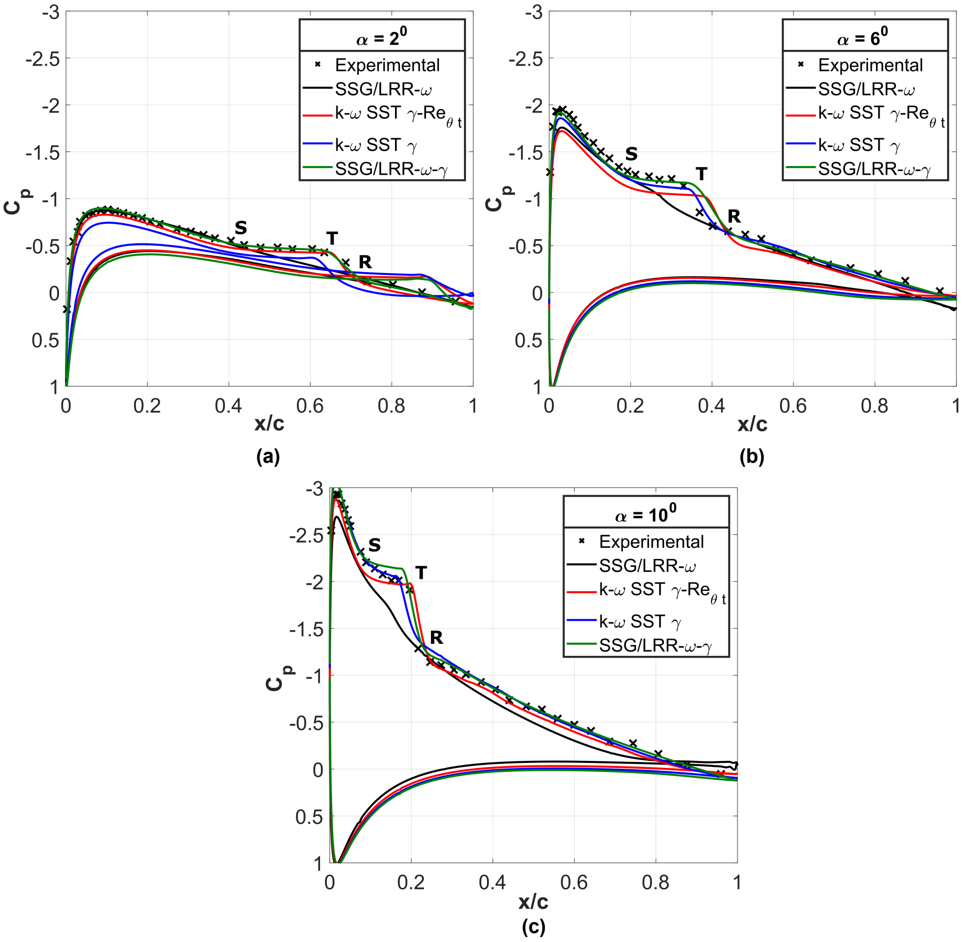

Figure 3.7: Comparison of C_p distribution predicted by different turbulence models at $\alpha = 2^0, 6^0, 10^0$ and Re = 140,000 for NACA-0018. S - Separation point; T - Transition point; R - Reattachment point

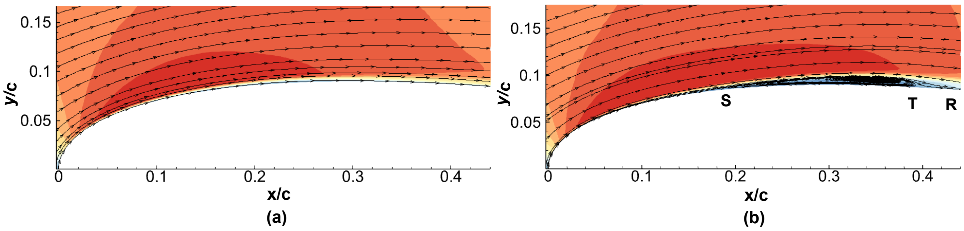

Figure 3.8: Comparison of boundary layer profiles predicted by a) fully turbulent SSG/LRR-ω model and the b) SSG/LRR-ω-γ model for the case where $Re = 140{,}000$ and $\alpha = 6^0$. The laminar separation bubble is clearly predicted in the latter case. S - Separation point; T - Transition point; R - Reattachment point

(Fig. 3.7b). These characteristics are not exhibited in the fully turbulent case where the skin friction coefficient remains positive throughout.

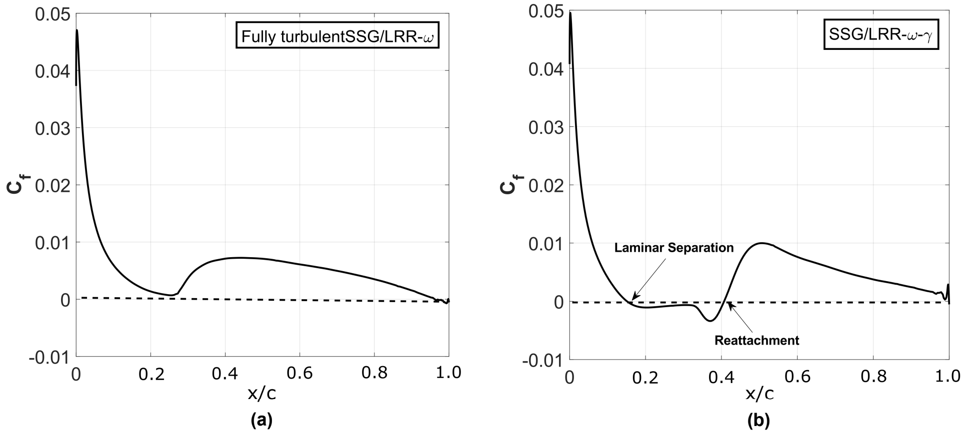

Figure 3.9: Comparison of C_f predicted by a) fully turbulent SSG/LRR-ω model and the b) SSG/LRR-ω-γ model for the case where Re = 140,000 and $\alpha = 6^0$

3.5.3 Wortmann Wing Case

A Wortmann FX63-137 Æ= 2 rectangular wing shown in Fig. 3.10 was investigated at a range of low Reynolds number flow conditions and angles of attack by Bastedo and Mueller [6]. C_P distributions were measured at various stations along the span to observe the impact of 3-dimensional flow and the wingtip vortex on the formation of a laminar separation bubble on the wing suction surface. For the current study, the flow condition selected has a chord Reynolds number of 80,000 and $\alpha = 7^0$, which results in the formation of a large region of laminar separation with turbulent reattachment, and significant variation in the bubble length from the wing root to tip. The computational domain was constructed to be geometrically similar to the wind tunnel used in the experiment in order to match any potential blockage effects. The clearance between the wing tip and the wall of the tunnel was 1.5 chord lengths. This wall was set to have the slip boundary condition. The freestream turbulence intensity in the wind tunnel used to gather experimental results was 0.1 %, and the inlet turbulence intensity was specified to match this value. The mesh for the wing case contains 15×10^6 cells, with a target surface size of 5 mm for a chord length of 1 m, and 65 prism layers in the near wall region. The near wall grid spacing was $1 \times 10^{-5} m$ to maintain a $y+(1)$ of less than 1 on the wing surface.

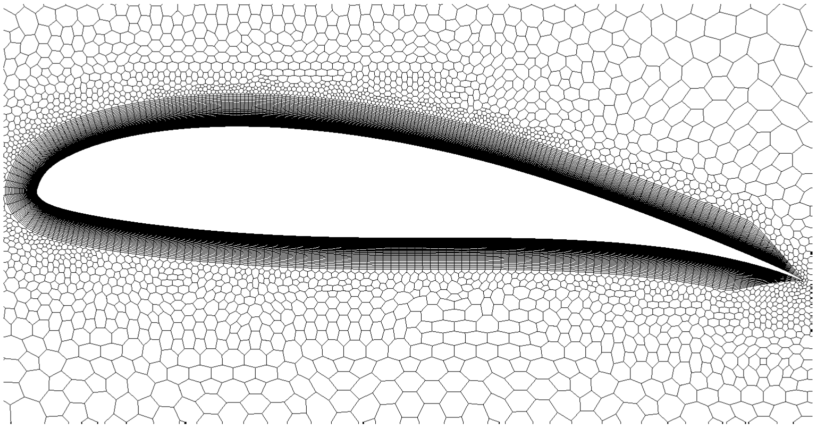

(a) FX63-137 airfoil section at $\alpha = 7^0$

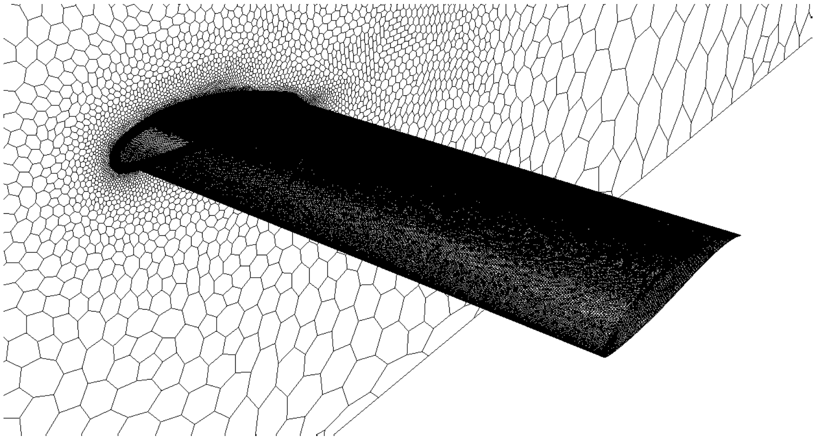

(b) Isometric view of the wing with Æ= 2

Figure 3.10: Computational mesh for Wortmann wing

Figure 3.11 presents the distribution of coefficient of pressure at different spanwise locations of the Wortmann wing ranging from the root till roughly 87% of the span. The sections closer to the wing-tip were not taken as the effects of crossflow were high. The current model successfully predicted the laminar separation at all the locations. Turbulent re-attachment is observed until the spanwise section 62.5% ,beyond which the flow simply separates. This is well captured by all the models. The transition point and reattachment points are well predicted by the respective RSM and SST one-equation transition models, however, the region defining transition (curve between transition and turbulent re-attachment points) is better approximated by the $k-\omega$ SST γ-$Re_{\theta t}$ model. This could be due to the formulation of F_{length}, the term that governs the transition length in the intermittency production. For the former two models, it is set to be a constant while in the latter it is modeled as a correlation function of critical Reynolds number ($Re_{\theta c}$). Overall, a fairly good agreement with the experimental results is observed.

The performance of the current transition model is very similar to the $k-\omega$ SST γ model in the transition and turbulent regions. However, the pressure peak in the laminar region is under-predicted by the $k-\omega$ SST γ model and this could be attributed to the fact that the model predicts larger separation at the trailing edge which in turn influences the flow upstream. This is illustrated in Fig. 3.12 that shows the velocity contours around the airfoil section at the root of the wing. The same reasoning can be extended to justify the over-prediction of the pressure peak by the fully turbulent SSG/LRR-ω model. It is ideally expected that the pressure peak predicted by a transition model be higher than a fully turbulent model due to the reduced friction loss observed by the model in laminar regions. However, that is not seen in the current case. Since the separation at the trailing edge predicted by the fully turbulent SSG/LRR-ω model is lesser than all the other transition models, it experiences a lower influence in the flow upstream, in turn resulting in a higher pressure peak.

The model was validated using a few more cases involving the McDonald Douglas 30P30N multi-element airfoil exhibiting turbulent shear layer induced transition and a prolate spheroid exhibiting three-dimensional natural transition but have not been included in the current

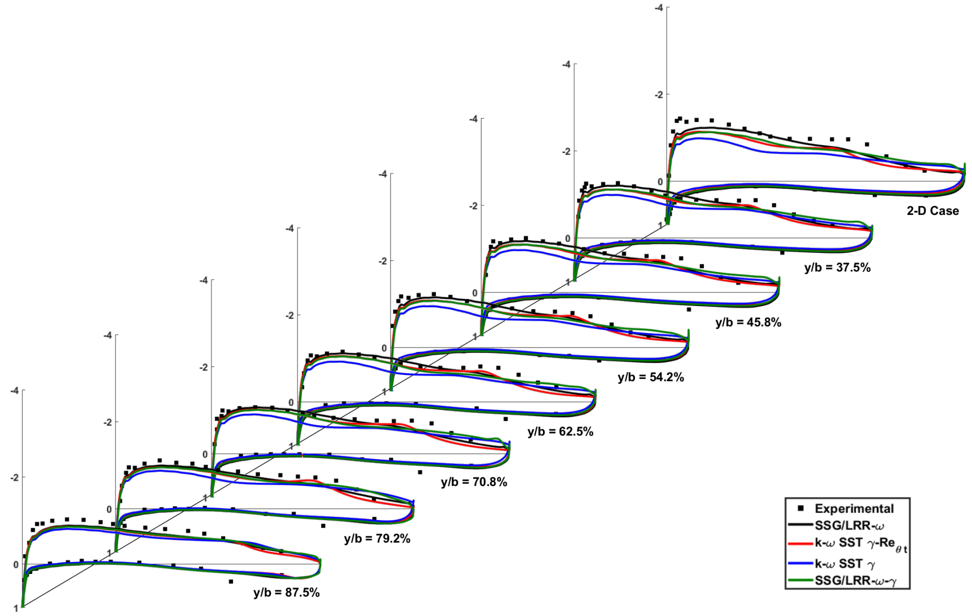

Figure 3.11: Comparison of C_p distribution for multiple spanwise locations of the Wortmann wing at $Re = 80,000$ and $\alpha = 7^0$

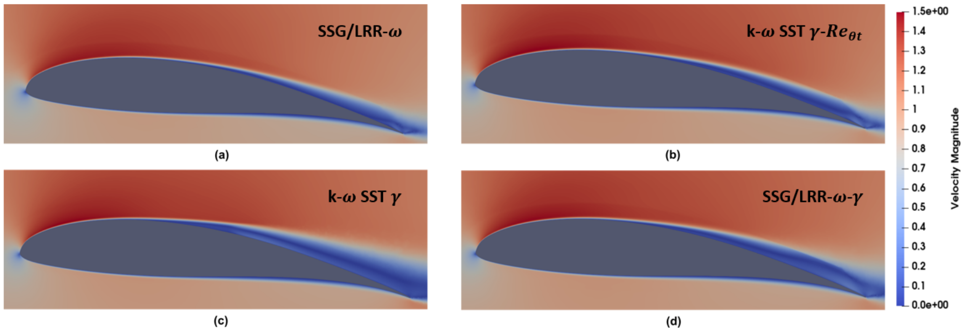

Figure 3.12: Velocity contour at the root of the Wortmann wing indicating different degrees of separation at the trailing edge

manuscript for the sake of brevity. Please refer to the publication by Pisharoti et al. [90] for details on these cases.

3.6 SSG/LRR-ω-γ-CF Validation Cases

3.6.1 NLF (2)-0415 Infinite Swept Wing

The first test case considered in this study is the NLF (2)-0415 infinite swept wing, which has a 45^o sweep. The experimental data for this case was taken from the tests conducted at the Arizona State University Unsteady Wind Tunnel [24]. In the experiment, hot wire measurements were obtained to study the crossflow instabilities and transition along the wing surface at various angles of attack. The current study has chosen the test case at $\alpha = -4^o$.

The computational domain was designed such that the inlet was 10 chord lengths ($10c$) upstream of the leading edge and the outlet was 15 chord lengths ($15c$) downstream of the trailing edge to avoid any influence of the boundaries. Periodic boundary condition (cyclic in OpenFOAM) was imposed on either side of the airfoil with a span of 0.3 chord lengths ($0.3c$). The top and bottom boundaries were placed 5 chord lengths ($5c$) from the airfoil respectively and were assigned a slip wall boundary condition. Figure 3.13 shows the computational grid close to the wing surface, wherein the wing has an angle of attack of -4^o to match the experimental conditions. In order to achieve a perfect face and point match for the cyclic boundaries, a two-dimensional grid for the NLF(2)-0415 airfoil was initially generated which then was extruded in the spanwise direction. The sweep angle was accounted for by setting the velocity vector at a 45^o angle in the $x - z$ (horizontal) plane. The initial conditions were assigned by setting the free-stream turbulence below 0.09% and viscosity ratio (ν_t/ν) equal to 1. Intermittency (γ) was initialized at a value of 1 in the whole domain.

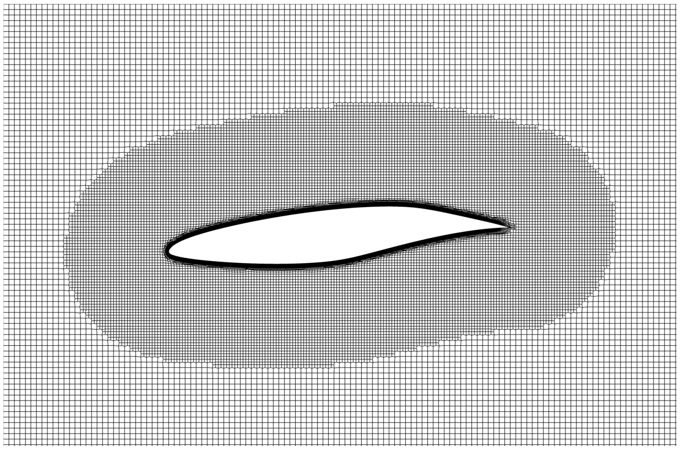

Figure 3.13: Near-body grid for the NLF (2)-0415 infinite swept wing

Grid and Numerical Scheme Sensitivity Study

The grid sensitivity study for the swept wing was carried out using four different grids, each grid progressively having finer near-body resolution. Since the focus of the current study is to capture boundary layer effects, emphasis on surface and near-wall grid parameters has been given in the current analysis. Table 3.2 shows the grid parameters for each mesh, wherein Δx_{body} is the surface spacing on the swept wing, $y^+(1)$ determines the spacing of the first layer and prism layers indicate the number of grid points in the wall-normal direction to resolve the boundary layer.

Table 3.2: Mesh parameters for grid-independence study

	Coarse	**Medium**	**Fine**	**Finest**
Δx_{body}	9.5 mm	6.3 mm	4.8 mm	3.9 mm
$y^+(1)$	1.2	1	0.8	0.5
Prism Layers	30	40	60	75
Total No. of Cells	8.3×10^5	2.7×10^6	5.3×10^6	11.1×10^6

Figure 3.14(a) presents the distribution of skin friction coefficient along the suction side of the swept wing. The curves show the grid sensitivity of the proposed model to the meshes listed in table 3.2. The coarsest mesh fails to predict transition, instead predicts

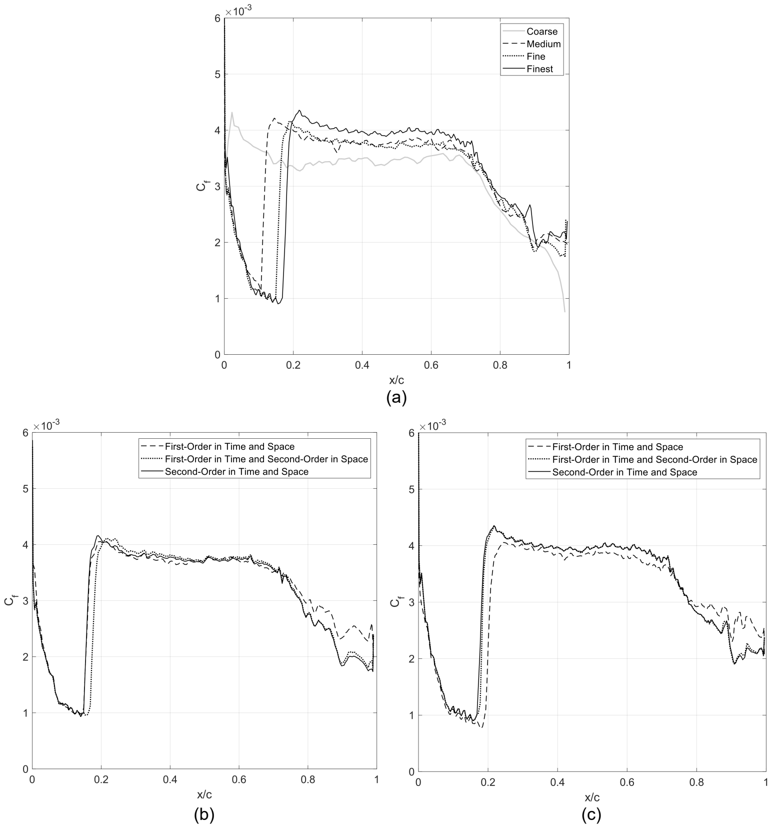

(a)

(b)

(c)

Figure 3.14: (a) Grid sensitivity study, (b) Numerical scheme sensitivity study using the "*Fine*" grid and (c) Numerical scheme sensitivity study using the "*Finest*" grid for the NLF(2)-0415 airfoil

a fully turbulent profile. As the mesh resolution increases, the transition location moves downstream. The predicted transition onset location gets closer with subsequently finer grids, however, not fully independent of the grid. It is clear that the model is quite sensitive to the grid resolution in the boundary layer. It is hypothesized that since the transition onset due to crossflow instabilities is formulated as a function of helicity, which is a function of the curl of velocity, the current model ends up being sensitive to small changes in the velocity gradient caused by changes in the grid resolution within the boundary layer. As a result, the "*Finest*" grid has been chosen for the remaining analysis. All simulations for the grid sensitivity analysis were conducted utilizing the *Crank-Nicolson* time integration scheme and the *Gauss linearUpwind* spatial discretization scheme.

To assess the impact of numerical schemes on model predictions, simulations were conducted on both the "*Fine*" and "*Finest*" grids, employing various combinations of spatial and temporal schemes of different orders. Figures 3.14 (b) and (c) show the effect of different numerical schemes on the predicted skin friction coefficient. In this analysis, first-order in time refers to the *Euler* scheme and first-order in space refers to *Gauss upwind*. Further, second-order in time refers to the *Crank Nicolson* and second-order in space refers to the "*Gauss linearUpwind*" scheme. As illustrated in Figures 3.14(b) and (c), it is evident that the location of transition onset is influenced by the choice of numerical scheme. However, concerning the flow downstream of the chord, the profiles computed using second-order spatial schemes exhibit minimal deviation, irrespective of the temporal scheme employed. This indicates that the model is more sensitive to the order of the spatial scheme close to the trailing edge, while it is fairly sensitive to all combinations of numerical schemes at the transition onset location. Therefore, to ensure sufficient accuracy, the second-order spatial and temporal schemes are applied for the remaining analysis.

It is important to emphasize that, for the stability of the current model, the divergence scheme for the Reynolds stress tensor was set to the *Gauss upwind* numerical scheme. Additionally, gradient limiters were applied to all turbulent quantities. Further, to tune the "Crank-Nicolson" scheme coefficient, an initial setting of 0.4 was implemented, gradually increasing it to 0.9 as the solution stabilized.

Study of the swept wing at multiple Reynolds numbers

Figure 3.15 illustrates the transition onset location predicted by both the streamwise and crossflow models. The transition location for each case was chosen as the point that saw the largest gradient change in the skin friction coefficient distribution over the suction side. Notably, the streamwise model consistently predicts a transition location that remains relatively unchanged across varying Reynolds numbers, thus failing to accurately capture the true onset location, especially at high Reynolds numbers. Conversely, the crossflow model demonstrates an ability to replicate the trend observed in experimental data, albeit with a consistent upstream prediction.

Figure 3.16 shows the distribution of skin friction coefficient on the swept wing surface along with limiting streamlines at different Reynolds numbers. The left column shows the predictions made by the streamwise transition model while the right column shows the crossflow model predictions. From experimental observations for the swept wing, it is known that at the lowest Reynolds number, transition is triggered predominantly by laminar separation and as the Reynolds number increases, crossflow transition becomes more prominent [18, 24]. In figure 3.16, at the lowest Reynolds number the streamwise model predicts transition initiated by laminar separation, consistent with experimental measurements, and corroborated by Figure 3.15.The crossflow model fails to predict any laminar separation, instead predicts crossflow transition further upstream. As Reynolds number increases, the streamwise model continues to predict separation-induced transition (or natural transition at the highest Reynolds number), while the crossflow model successfully captures crossflow-instability induced transition. As a result, the crossflow model also predicts a much higher skin friction coefficient along the wing surface, while the streamwise model predicts a largely laminar flow with with low levels of skin friction.

In summary, the crossflow model captures the effects of crossflow transition well, but consistently predicts an early onset of transition. Efforts in improving the accuracy of the model prediction are currently underway. The γ transition model lends itself to fine-tuning through a lot of its user-accessible model constants [76]. Calibration studies for these model constants is one such avenue that is being explored to improve model accuracy and will be presented in future studies.

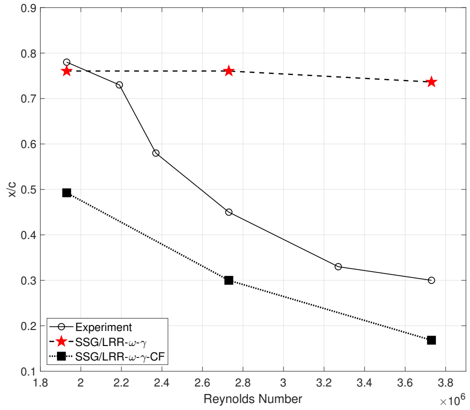

Figure 3.15: Predicted transition onset at different Reynolds numbers

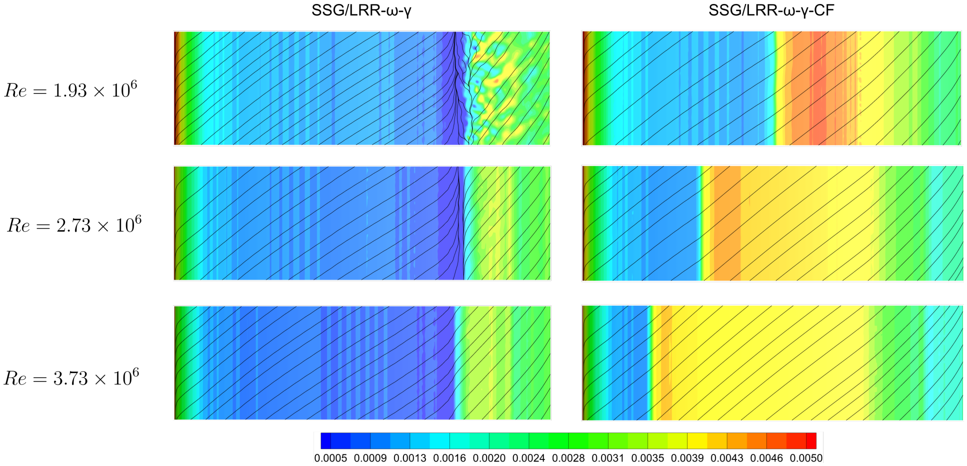

Figure 3.16: C_f contour at different Reynolds numbers with limiting streamlines on the suction side

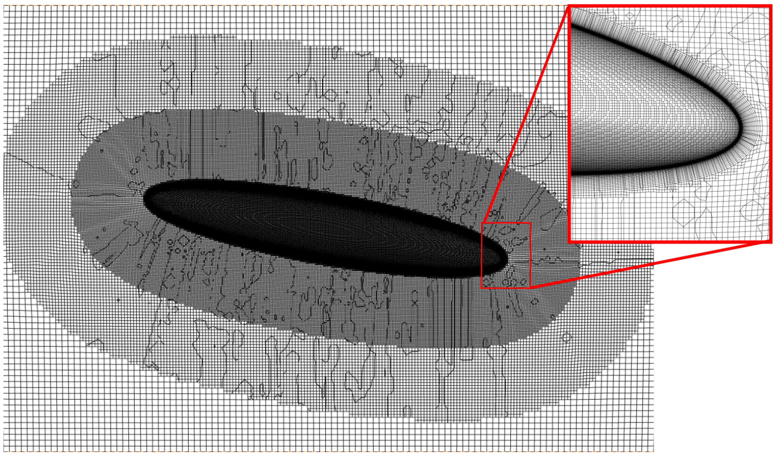

Figure 3.17: Near-body grid for the DLR 6:1 prolate spheroid

3.6.2 DLR 6:1 Prolate Spheroid

The DLR 6:1 prolate spheroid is a good test case to validate the proposed model, since it manifests complex 3-D flows involving crossflow transition and free-wake vortices. The flow around the spheroid is subject to pressure gradients in the streamwise as well as the spanwise directions , similar to the flow observed on any underwater vehicle of general 'drag-optimized' shape. Experimental data on the spheroid are taken from the tests that were carried out at the DLR Göttingen 3x3 low-speed wind tunnel in 1980 as reported in [52]. In the current study the spheroid is analyzed at three angles of attack (α) and a Reynolds number of 6.5×10^6.

Figure 3.17 shows the grid for the case where $\alpha = 10^o$, with the zoomed in window highlighting the surface and the near-wall grid. The computational domain had the same cross-section as the tunnel test section, and was set to a slip wall boundary condition. The turbulence intensity at the inlet was set to 0.3% such that it decays to a value between (0.2% - 0.1%) at the leading edge of the spheroid, as specified in the experimental conditions [52]. The viscosity ratio at the inlet (ν_t/ν) is set to a value of 2.

Grid Independence Study

The grid independence study for the spheroid was carried out on the case with a free-stream Reynolds number of 6.5×10^6 and $\alpha = 10^o$. Similar to the previous test case, parameters that influence the near-wall and surface resolution were considered in this study and are detailed in table 3.3.

Table 3.3: Mesh Parameters for grid-independence study

	Coarse	**Medium**	**Fine**	**Very Fine**
Δx_{body}	0.0125 m	0.0075 m	0.005 m	0.0037 m
$y^+(1)$	1.2	1	0.8	0.6
Prism Layers	35	45	65	80
Total resolution	946,766	3,774,781	12,294,680	28,159,365

Figure 3.18 shows the contours of skin friction coefficient predicted by the crossflow model. Sectional markers (in black) have been shown to aid in better visualization of the contour and transition locations. It is seen that the crossflow transition is captured by all grids. The transition location, specifically in the mid-portion of the body, tends to move downstream with an increase in resolution, making the prediction closer to the experimental result. On the other hand, at the windward side, it is seen that the model prediction gets worse with an increase in mesh resolution. The prediction made by the "*Coarse*" mesh along the windward side is seen to align closest with the experimental data. A similar effect is also observed in the helicity-based SSG/LRR-ω-γ-$\mathrm{Re}_{\theta t}$ crossflow transition model proposed by Nie et al. [83]. It is safe to say that the transition observed at the windward side is a lot more sensitive to the mesh resolution compared to the transition across the leeward side and the mid-body. Finally, from the "*Fine*" and the "*Very Fine*" mesh resolutions, it is seen that the transition line along the onset locations are slightly different, while it is very similar along the rest of the body. For the purposes of this study, the "*Fine*" mesh resolution has been chosen for the remaining analyses.

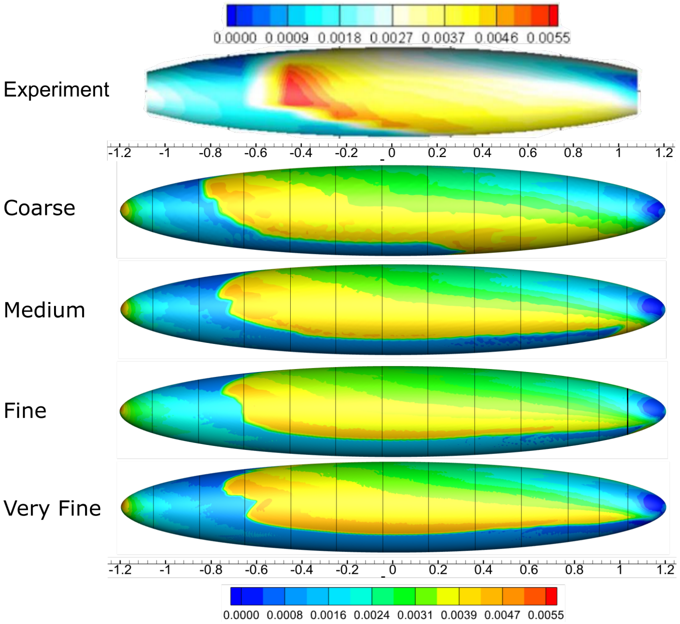

Figure 3.18: C_f distribution predicted by SSG/LRR-ω-γ-CF. Grid independence study performed at $\alpha = 10^o$ and Re$= 6.5 \times 10^6$. Experimental contour from [83].

Spheroid at $\alpha = 5^o$

Figure 3.19 shows the distribution of skin friction coefficient predicted by the streamwise and crossflow transition models at $\alpha = 5^o$. These predictions have also been compared against the fully turbulent model predictions. It is evident that the fully turbulent model predicts a largely different flow contour compared to reality. On the other hand, at the current angle of attack, both streamwise and crossflow transition models exhibit very similar behavior. They predict similar onset locations on the leeward side. The crossflow model tends to better predict transition onset along the mid-portion of the body, when compared to the streamwise model. Additionally, the model is seen to capture the transition line seen in the experimental contour well, except close to the windward side.

From previous works [53], it was shown that the spheroid experiences transition initiated by simultaneous excitation of Tollmein-Schlichting (TS) and crossflow instabilities, resulting in

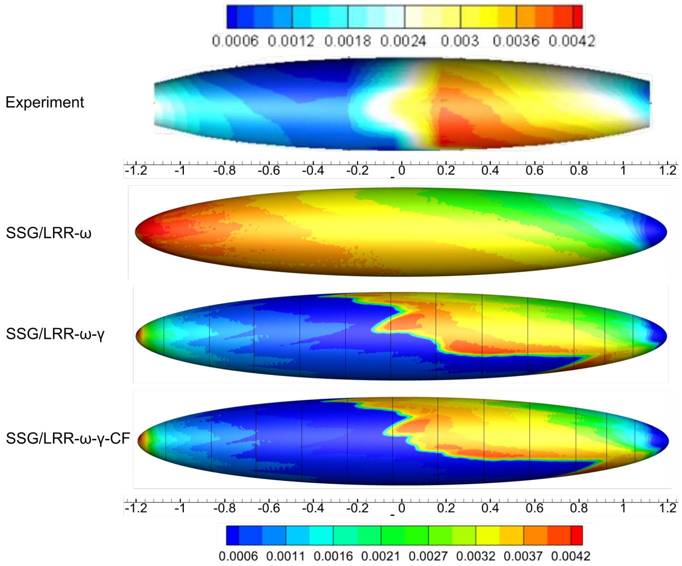

Figure 3.19: C_f contour at $\alpha = 5^o$ and Re=6.5×10^6. Experimental contour from [83].

a mix of natural and crossflow transition at this test condition. This makes the case highly complex to model. It was explained that the windward side sees transition triggered by TS-waves. Both transition models seem to be able to capture this effect, albeit with slightly better accuracy observed in the streamwise model. This could imply that the coupling of the streamwise and crossflow transition production terms could be modified to improve the state of the crossflow transition model in predicting natural transition. It is important to note that even at the finer mesh resolutions, the current transition model tends to predict the transition at the windward side, which has not been observed in any other crossflow model. Furthermore, the overall similarity of the streamwise model to the crossflow model is very specific to the proposed formulation and has not been observed in any other transition model. Further discussion on this is presented in Section 3.6.2.

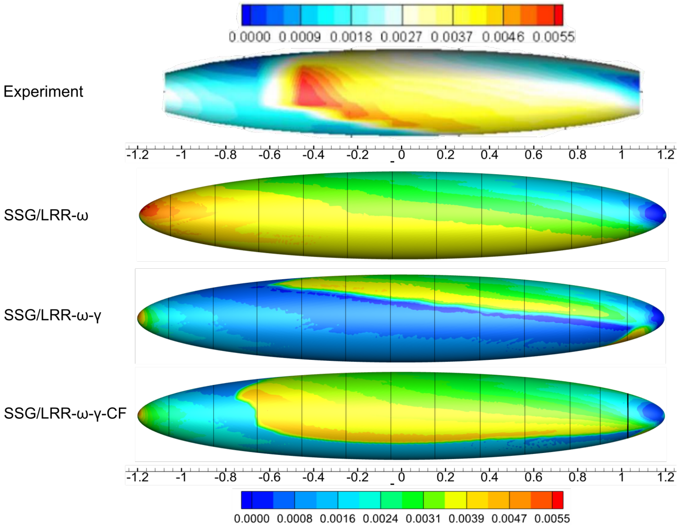

Figure 3.20: C_f contour at $\alpha = 10^o$ and Re=6.5×10^6. Experimental contour from [83].

Spheroid at $\alpha = 10^o$

The skin friction distribution at the test condition of $\alpha = 10^o$ is shown in figure 3.20. All models are able to predict the separation seen at the leeward side, close to the trailing edge (indicated in light blue). The crossflow transition is well captured at the onset, however, the model fails to capture the transition at the windward side. It was shown that even at $\alpha = 10^o$, there is transition initiated by TS-waves [53]. The streamwise transition model predicts transition onset on the leeward side and also manages to predict some transition at the windward side, albeit predicts laminar flow along most of the mid portion of the body.

Spheroid at $\alpha = 20^o$

At this high inclination, the flow experiences pure crossflow transition. Figure 3.21 shows that the spheroid experiences separation starting from the leeward side (at $x = -0.5m$) all the way to the trailing edge and is indicated by the light-blue region in the experimental contour. This effect is well captured by all turbulence models as indicated by the green-blue

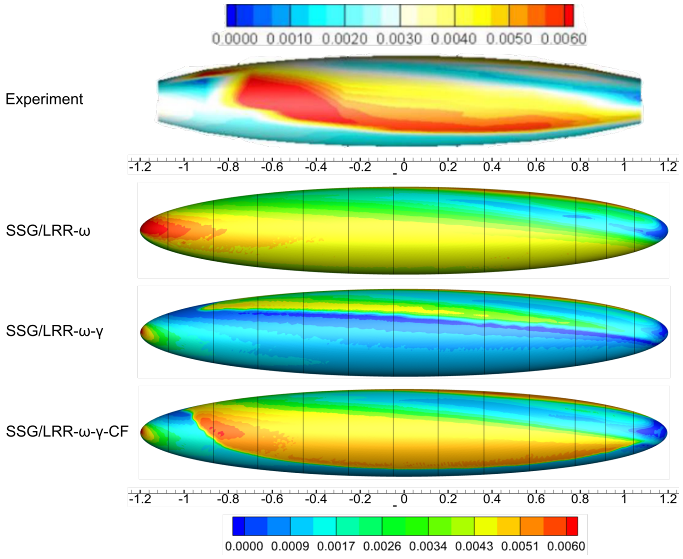

Figure 3.21: C_f contour at $\alpha = 20^o$ and Re=6.5×10^6. Experimental contour from [83].

region in the computational contours. The streamwise transition model is able to predict the transition onset on the leeward side, but fails to predict the transition line that stretches along the mid-portion of the body all the way close to the windward side. The crossflow model on the other hand, successfully predicts the onset of crossflow transition and shows a very good approximation of the transition line. However, the model predicts the onset location to be slightly upstream in comparison to the experimental data.

Comparison of Streamwise Transition Models

In this section, different streamwise transition models are analyzed and compared. Two widely used streamwise transition models have been considered, in addition to the current streamwise formulation. The first one is the k-ω SST γ-$Re_{\theta t}$, proposed by Menter [73]. The model is available in the OpenFOAM library. The second model is the k-ω SST γ model proposed by Menter et al., [76]. Since this model is not available in the OpenFOAM library, it has been implemented (and validated) by the authors [89, 90]. This analysis was carried out to understand how widely used streamwise models compare to the RST-based streamwise model in highly 3-dimensional flows which experience simultaneous crossflow and natural transition. Therefore, the spheroid at $\alpha = 5^o$ and $\alpha = 10^o$ have been considered and the same grid has been used across all models.

Figure 3.22(a) shows the skin friction coefficient distribution at the lower inclination. The models seem to predict a similar transition onset location on the leeward side, but greatly differ in predicting transition over the rest of the body. The SST-based γ-$Re_{\theta t}$ model appears to predict the least amount of transition along the body, while the SST-based γ transition model, bears more similarities with the RST model. This can be attributed to the fact that both models use the same transition model formulation. However, neither of the SST-based models have been able to capture transition on the windward side. The reason behind the RST model being able to capture a fuller transition profile, compared to the SST-based models could be attributed to the fact that the model uses the Reynolds stress-based closure which accounts for isotropic as well as anisotropic turbulent stresses, in turn resulting in an improved prediction on highly three-dimensional flows.

Figure 3.22(b) shows the model predictions at $\alpha = 10^o$ which is a case that still has a mix of natural and crossflow transition but to a smaller extent compared to the previous case. At this test condition, all streamwise transition models predict a predominantly laminar flow. The transition onset on the leeward side is better predicted by the SST and RST-based γ transition models, compared to k-ω SST γ-$Re_{\theta t}$. The RST-based transition model manages to capture some transition on the windward side but is far from the experimental results discussed earlier. It is seen that the streamwise transition models tend to behave similar to each other as the inclination increases, where crossflow instabilities become more predominant.

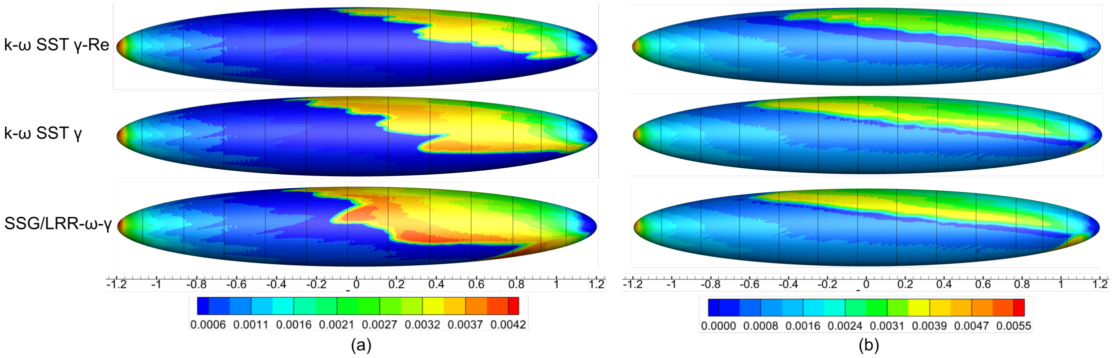

Figure 3.22: C_f Contour predicted by different streamwise transition models at (a) $\alpha = 5^o$ and (b) $\alpha = 10^o$

3.7 Conclusions

The SSG/LRR-ω Reynolds stress transport model and γ transition model were coupled and implemented in the open-source CFD toolbox, OpenFOAM, to provide a robust and simplified Galilean invariant framework for the prediction of different flow transition mechanisms. The model coupling approach was modified by adding an auxiliary source of production to the Reynolds stress transport equation in order to increase turbulence production for cases with low freestream turbulence intensity. A hybrid production term for turbulent specific dissipation rate was also introduced to ensure nominal levels of production of dissipation in laminar regions.

The transition model was also extended to include crossflow transition effects. The modification to the original model formulation was made by adding a term to the intermittency production that accounts for crossflow transition. This additional term uses a local helicity-based formulation since helicity was discovered as a major contributor to the crossflow velocity gradient and thereby acts as a good indicator of crossflow instabilities.

The model and its crossflow extension were both validated using various benchmark cases. It showed improved prediction accuracy compared to existing transition models for natural and bypass transition. It also exhibited equivalent accuracy for separation-induced transition. When it came to highly three-dimensional flows for natural and crossflow transition, the current model showed superior prediction capability, thereby making it a great candidate for complex three-dimensional flows.

Chapter 4

Computational Methods for Aerodynamic and Aeroacoustic Analysis of Propellers

4.1 Aerodynamic Modeling

4.1.1 Geometry and Grid Generation

Two propellers were considered in the current study : 1) Delft-APC Propeller and 2) T-motor CF 30×10.5. The Delft-APC propeller is a modified version of the APC-96 propeller, introduced by Casalino et al. [15] with the intention of setting a benchmark case for low-*Re* propellers. The group tested the propeller at the TU-Delft A-tunnel, which is a vertical semi-anechoic open-jet wind tunnel. They conducted oil-flow visualizations and phase-locked stereoscopic particle image velocimetry (PIV) to visualize the flow on the rotor surface and capture the formation of laminar separation bubbles [40, 41]. They also carried out far-field acoustic tests to understand the impact of flow transition and separation on the acoustic spectra, specifically, the broadband noise spectra. This experimental database is one of the few existing datasets that offer valuable insights into the surface flow characteristics of low-*Re* propellers. Figure 4.1 shows the geometry, chord and twist distribution of the Delft-APC

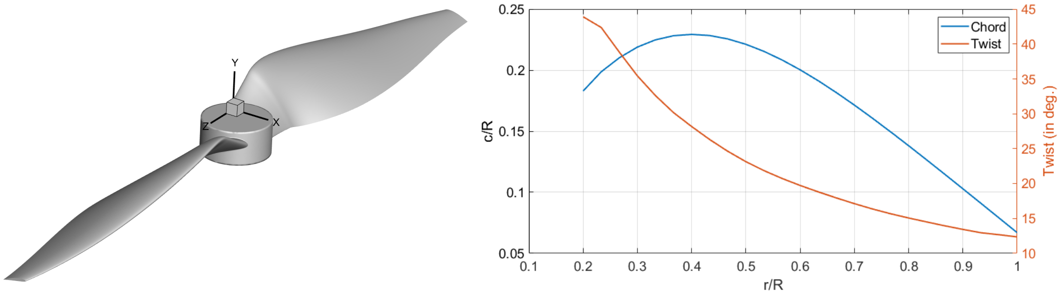

(a) (b)

Figure 4.1: Delft-APC Propeller Geometry

propeller. The propeller uses the NACA4412 profile for its cross-sections and has a diameter of 0.3m. The CAD file for this geometry was obtained directly from the authors of [15]. This propeller geometry and size are typical of those commonly used for sUAS applications.

The second propeller considered in this study is the T-motor CF 30 × 10.5. It is an off-the-shelf propeller, made of carbon fiber, with a diameter of 381mm and pitch of 266.7mm. The propeller was tested at the Virginia Tech Open Jet Wind tunnel [120]. This experimental campaign was carried out to study the effects of propeller inflow, RPM and propeller yaw on the rotor thrust, torque and acoustic characteristics. Whelchel et al. [119] also decomposed the total noise spectra into tonal and broadband components to investigate the impact of varying operating conditions on each component. This decomposition is advantageous for the current analysis, as it provides a direct comparison between the modelled broadband noise component of blade self-noise and the broadband noise spectra obtained from experimental measurements. Figure 4.2(a) displays the propeller geometry, featuring a simplified elliptical hub utilized for the CFD calculations. This hub was selected to facilitate better mesh quality by avoiding sharp edges and corners. Figure 4.2(b) give the chord and pitch distribution of the propeller. The CAD file for this geometry was obtained from a high fidelity 3D scan. This propeller geometry and size are characteristic of heavy payload multi-copters or eVTOL applications featuring distributed propulsion systems comprising a large number of rotors.

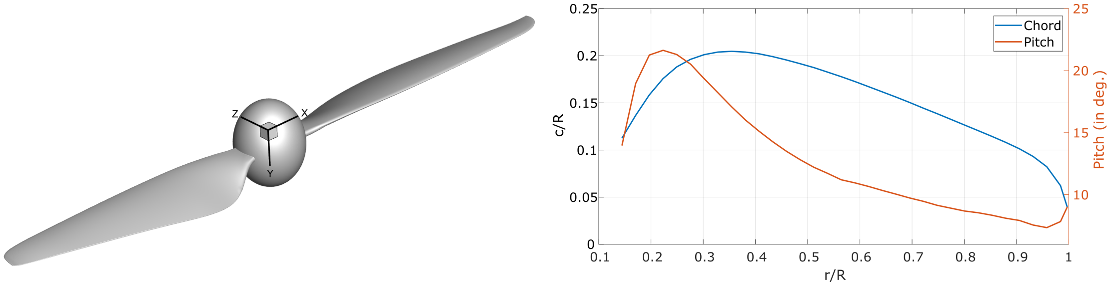

(a) (b)

Figure 4.2: T-motor CF 30 × 10.5 Propeller Geometry

The CFD analysis in this work was carried out using OpenFOAM-v2006, an open-source finite-volume code written in C++. The grids for the current analysis were constructed on the Pointwise mesh generation software. An overset grid set-up was adopted for the current study. The moving mesh and the background mesh were constructed separately and were saved in the OpenFOAM format. They were then merged on OpenFOAM using the "mergeMeshes" utility. The background mesh is a simple structured block which stretches up to $8R$ in the plane of the propeller and $10R$ in the direction of the wake. A simple domain sensitivity study showed that the inlet height needs to be equal to or greater than $2R$. Therefore, for safety, the current study selected a value of $4R$ for the inlet placement. The moving mesh was constructed using a cylindrical domain that stretched upto $1.1R$ in the radial direction. The cylindrical overset surface grid was fully structured and care was taken to ensure that the largest cell size in the moving mesh matched the smallest mesh size in the background mesh in order to avoid any overset interpolation errors. Further, the finest mesh within the background region that encompassed the moving mesh extended up to $3R$ in the direction of the wake. The volumetric grid within the moving mesh was fully unstructured. For the T-motor propeller, most of the blade surface grid was structured, except for the hub and the blade tips. On the other hand, for the Delft-APC propeller, the blade surface grid was initially constructed to be fully structured and then diagonalized to make it unstructured. It was seen that this approach reduced the non-orthogonality of the

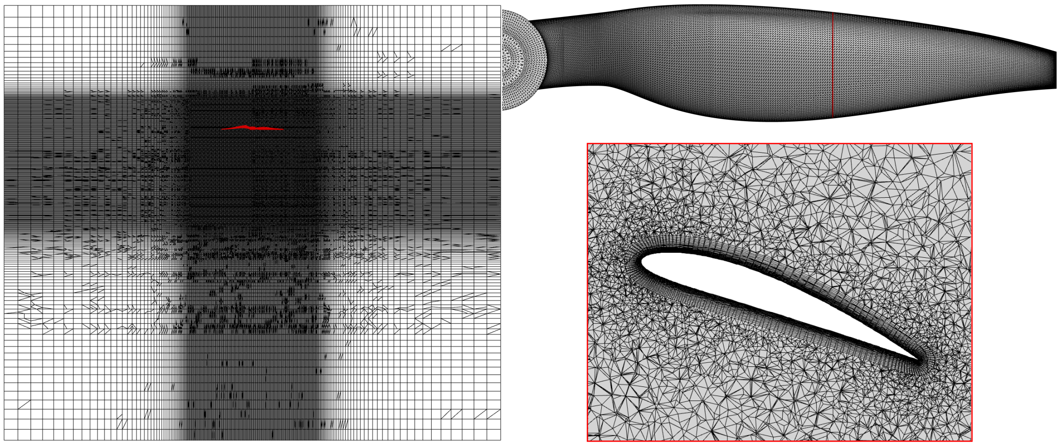

Figure 4.3: Delft-APC Propeller Computational Grid: Background Mesh (Left), Surface grid (Top-right) and Near-wall Resolution @ $r/R = 60\%$ (Bottom-right)

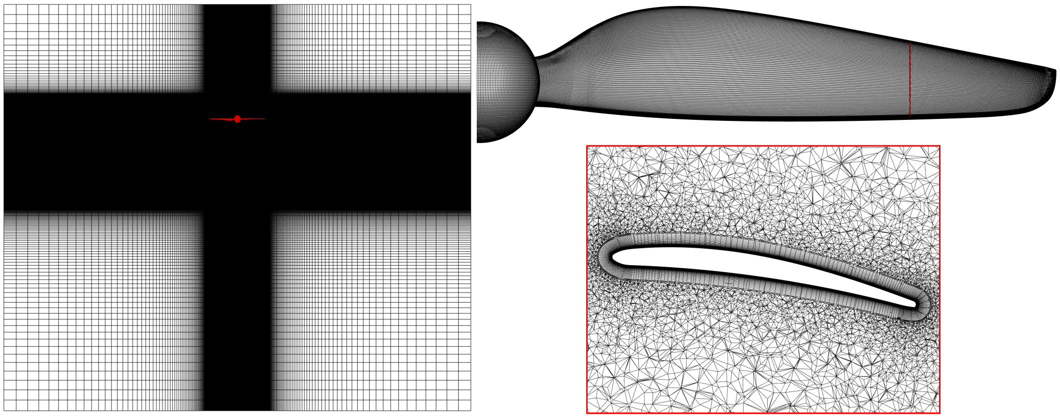

Figure 4.4: T-motor CF 30×10.5 Propeller Computational Grid: Background Mesh (Left), Surface grid (Top-right) and Near-wall Resolution @ $r/R = 75\%$ (Bottom-right)

grid at the blunt trailing edge. This was not an issue for the T-motor propeller, as it features a blunt but curved trailing edge, which facilitated the creation of a high-quality structured mesh in that region. The near-wall grid at a specific blade section, illustrating the prism layers close to the rotor surface and the unstructured T-Rex volumetric grid, is depicted in the bottom-right corner of figures 4.3 and 4.2. A grid-independence study was carried out for both these propellers, and is presented in the next chapter.

It is to be noted that grid generation in the current study was initially carried out using

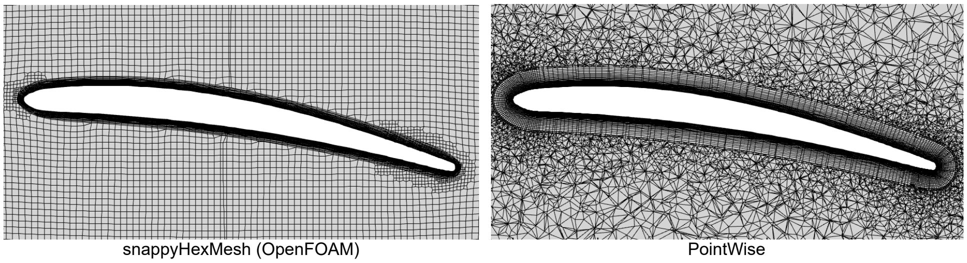

Figure 4.5: Cross-sectional grid for the T-motor propeller at $r/R = 0.75$ generated by snappyHexMesh (left) and PointWise (right)

the OpenFOAM meshing tool *snappyHexMesh*. Aerodynamic analysis using this grid was published in Pisharoti et al. [91, 92]. Later on, the Pointwise grid was adopted since it allowed for adjustments to leading and trailing edge spacings, growth rates in the volumetric region, and prism layer meshes at both blunt and sharp corners. These capabilities resulted in a well-resolved boundary layer region for the Pointwise grid, in contrast to the OpenFOAM grid, as illustrated in figure 4.5. The figure presents the grid-independent cross-sectional mesh at the spanwise section of ($r/R = 0.75$) generated by the two meshing tools. The major differences in mesh resolution are evident in the prism layers and volumetric mesh. The growth rate in the Pointwise mesh is significantly more gradual compared to OpenFOAM. Additionally, the prism layer in the OpenFOAM mesh collapses closer to the trailing edge, whereas in the Pointwise mesh, it remains well-structured and completely wraps around the trailing edge. However, in the aerodynamic analysis, it was observed that these differences did not significantly impact the prediction of performance characteristics for either grid. Despite this, the current study opted to proceed with Pointwise due to its superior control over various grid parameters.

4.1.2 Turbulence Modeling

The proposed transition model, SSG/LRR-ω-γ, was validated against the experimental data obtained for the two test geometries discussed in the previous section. In addition to the proposed model, turbulence models of different orders of RANS closure available in the OpenFOAM library were also evaluated. These models include:

- Spallart Allmaras (SA) [102]: It is a first-order closure (linear-eddy viscosity), fully turbulent model. It is widely recognized and extensively employed for high Reynolds number flows in aerospace applications. The model utilizes a single transport equation for the turbulent variable of effective turbulent viscosity, $\tilde{\nu}$. Thai et al. [109] investigated this model and its transition model variants to assess the most suitable candidate for low-Re rotor applications. They concluded that the fully turbulent model is highly robust and performs equivalently or even better than transition models under various flow conditions, with lower computational costs. Hence, it is worthwhile to evaluate the model for the proposed test geometries.

- k-ω SST [74]: It is another widely used fully turbulent model. The model is a first-order closure (linear-eddy viscosity), two-equation model that uses the transport variables of Turbulent Kinetic Energy or TKE (k) and specific dissipation rate (ω) in its formulation.

- k-ω-γ-$Re_{\theta t}$ [73]: This is one of the most popular transition turbulence models and is also known as the Langtry-Menter model. It is a first-order closure (linear-eddy viscosity), four-equation, transition turbulence model. As discussed in Chapter 3, in addition to the transport equations of k and ω, this model uses equations for intermittency (γ) and transition Reynolds number ($Re_{\theta t}$).

- SSG/LRR-ω : This is a second-order closure (Reynolds stress transport), fully turbulent model [30]. The detailed formulation for this model is given in Section 3.1.1. It solves for the six components of the Reynolds stress and the specific dissipation rate (ω), making it a seven-equation framework. The proposed transition model is an extension of this fully turbulent model. Although the model is not readily available in the OpenFOAM libraries, the author has implemented it as part of the transition model implementation.

All turbulence models were initially evaluated based on their prediction capabilities of global performance quantities such as thrust and torque. Subsequently, their prediction of boundary layer characteristics and wall-shear stress were also assessed.

4.1.3 CFD Solver Set-up

A URANS simulation was employed on the merged overset mesh using *overPimpleFOAM*, an incompressible transient solver. The *pimpleFOAM* solver is a versatile solver that is a combination of the SIMPLE and PISO algorithms for pressure-velocity coupling [115]. It is capable of handling transient flows with large time steps while maintaining convergence stability. Initially, 8 outer corrector loops were used per time step and once the solution stabilized, they were reduced to 3 per time step. Further, 3 additional inner-corrector loops (pressure-correctors) were employed, allowing for convergence of flow parameters per time step. Non-orthogonal correctors were also utilized for the solution, with the T-motor propeller employing 3 corrector iterations and the Delft-APC propeller employing 4 corrector iterations. The higher number of iterations in the latter case is attributed to the increased non-orthogonality in the mesh, as discussed in the previous section.

In the current study, specific measures were implemented to ensure the stability of the

Reynolds stress models. Although these measures were primarily intended for Reynolds stress models, they were uniformly applied to all models. The simulations were initially run with the turbulence suppressed for the first 5 revolutions, employing a time discretization equivalent to 1° of rotor revolution. Subsequently, turbulence was activated, and the simulations were continued for an additional 5 revolutions, utilizing a time discretization equivalent to 0.5° of rotor revolution. Finally, the simulations were extended for another 4 revolutions with a time discretization equivalent to 0.25° of rotor revolution. This approach of discretizing time steps based on rotor revolution facilitated easier sampling of flow and noise data. For the Delft-APC propeller, Grande et al. [40] determined the vortex shedding frequency and wavelength to be approximately $10,000$Hz and 2.4mm, respectively, at the highest advance ratio ($J = 0.6$). To ensure the accuracy of the URANS simulation, the temporal and spatial discretization near the rotor surface was approximately an order of magnitude smaller than these values. Since the vortex shedding for the T-motor propeller was not quantified, the same discretization parameters were applied to this rotor as well.

The numerical schemes employed in the study were all second-order accurate. The *Crank-Nicolson* scheme was utilized for temporal discretization, while the *limitedLinear* scheme was employed for spatial discretization. Initially, the numerical schemes were set to first-order when turbulence was activated, but gradually transitioned to second-order to enhance numerical accuracy and reduce numerical dissipation. All numerical tuning was finalized by the 12^{th} rotor revolution, and the last two revolutions were conducted with the highest permissible order of accuracy for the given problem.

The boundary conditions for all turbulent variables were established following the specifications outlined in the NASA-LARC turbulence modeling resource [1]. The rotor was assigned a moving wall boundary condition for velocity. Inlets and side boundaries were modeled as velocity inlets with a fixed value, whereas the outlet was configured as a pressure outlet.

Hover conditions typically induce some velocity upstream of the rotor due to flow curl-up [90]. Imposing a fixed value of zero velocity at the inlet would cause a discontinuity at the boundary. Therefore, for the hover case, even though the inflow velocity is zero, the velocity boundary condition was set to the zero gradient condition instead of a fixed value constraint.

4.2 Aeroacoustic Modeling

4.2.1 Tonal Noise Prediction

In the current analysis, tonal noise was predicted using the *libAcoustics* tool on OpenFOAM. It is an external library developed by UniCFDLab [31]. The library uses the acoustic analogy, wherein the flow solution is computed by the OpenFOAM solver and the acoustics are computed using the Ffowcs-Williams Hawkings equation. It is a post-processing utility, which runs concurrently with the flow solution and updates the acoustic solution in real-time. The FW-H equation as presented in [8] is shown in equation (4.1).

$$\bar{\Box}^2 p'(\mathbf{x},t) = \frac{\partial}{\partial t}\left[\left[\rho_0 v_n + \rho(u_n - v_n)\right]\delta(f)\right] - \frac{\partial}{\partial x_i}\left[\left[\rho u_i(u_n - v_n) + \Delta P_{ij} n_j\right]\delta(f)\right] + \frac{\partial^2}{\partial x_i \partial x_j}\left[T_{ij} H(f)\right] \tag{4.1}$$

where, $\bar{\Box}^2 = \frac{1}{c^2}\frac{\bar{\partial}^2}{\partial t^2} - \bar{\bar{\nabla}}^2$ is the D'Alembertian wave operator. The first term on the right hand side represents the thickness noise where v_n is the normal velocity of the surface. The second term represents loading noise due to unsteady and steady loading on the surface where P_{ij} is the compressive stress tensor (comprising of the pressure and shear stress) on the surface and n_i is the surface unit normal vector. $T_{ij} = \rho u_i u_j + P_{ij} - c^2\rho'$, is the Lighthill's stress tensor. $H(f)$ is the Heaviside function, when multiplied with T_{ij} implies that the term is applicable only when $f > 0$, that is, outside the surface. It is a volume source which is due to the turbulence off of the surface. The above expression is a form of FW-H which can be applied to permeable surfaces. When $v_n = u_n$, the equation is applicable to impermeable surfaces and that is the form that has been adopted for the current study. In low Mach number applications, noise originating from surface loading and blade thickness tends to radiate much more efficiently than noise generated by turbulence within the flow. Consequently, the last term in equation (4.1) is often neglected [36].

The computed flow solution is propagated to the far field observer using the FW-H equation with surfaces defining the impermeable boundaries in the domain, which in the current case is the rotor surface. The FW-H equation has the form of a linear in-homogeneous wave equation. Farassat came up with a solution for the general FW-H equation and is given in detail in [32]. The equations below give the final expressions for the thickness (p'_T) and loading noise (p'_L) components.

$$4\pi p'_T(\mathbf{x},t) = \int_{f=0} \left[\frac{\rho_0 \dot{v}_n}{r(1-M_r)^2} + \frac{\rho_0 v_n \hat{r}_i \dot{M}_i}{r(1-M_r)^3} \right]_{\text{ret}} dS + \int_{f=0} \left[\frac{\rho_0 c v_n (M_r - M^2)}{r^2(1-M_r)^3} \right]_{\text{ret}} dS \quad (4.2)$$

$$4\pi p'_L(\mathbf{x},t) = \int_{f=0} \left[\frac{\dot{p}\cos\theta}{cr(1-M_r)^2} + \frac{\hat{r}_i \dot{M}_i p\cos\theta}{cr(1-M_r)^3} \right]_{\text{ret}} dS + \int_{f=0} \left[\frac{p(\cos\theta - M_i n_i)}{r^2(1-M_r)^2} + \frac{(M_r - M^2) p\cos\theta}{r^2(1-M_r)^3} \right]_{\text{ret}} dS \quad (4.3)$$

This expression is formally called *Formulation 1A*. The term in the denominator '$(1 - M_r)$' is called the Doppler factor, where M_r is the Mach number in the direction of the sound radiated. The subscript '*ret*' indicates that the solution is evaluated at the retarded time ($g = \tau - t + r/c = 0$), the time at which the source emits the signal. The near-field terms are separated from far-field terms by using $(1/r^2)$ and $(1/r)$ respectively. Terms with dots are source time derivatives and terms with subscripts 'i' are the result of a dot product between the variable and the corresponding unit vector. Current work uses this formulation to solve the FW-H equation in order to predict tonal noise.

For acoustic predictions, the *libAcoustics* library samples the surface pressure distribution over the rotor every 0.5° of rotor revolution. Sampling occurs over a time period of 2 rotor revolutions to account for the time it takes for the acoustic wave to reach the observer. Only the pressure signal for the 2nd revolution is considered to compute the acoustic spectra. The signal resembles that of a periodic case, thereby outputting deterministic component of noise.

4.2.2 Blade Self-Noise Prediction

The main emphasis on aeroacoustics in the current study is on the broadband noise component of blade self-noise, that is known to stem from turbulent interactions within the blade boundary layer. Ideally, Farassat's Formulation 1A can be employed to model broadband noise by simulating surface pressure fluctuations. Wall-resolved LES or DNS methods are capable of resolving these pressure fluctuations at the surface. However, the high spatial and temporal resolution required for these methods renders them impractical, as discussed in Section 1.1.3. Since RANS models only capture the mean turbulence, they are unsuitable for predicting broadband noise using Formulation 1A. Therefore, the current work has adopted the semi-empirical Brooks Pope and Marcolini formulation (BPM) to compute self-noise. It is one of the most widely used self-noise prediction methods in academic and industrial settings.

The BPM method divides self-noise into five different sources as illustrated in figure 4.6. Scaling laws for each of these noise sources were derived based on extensive experimental

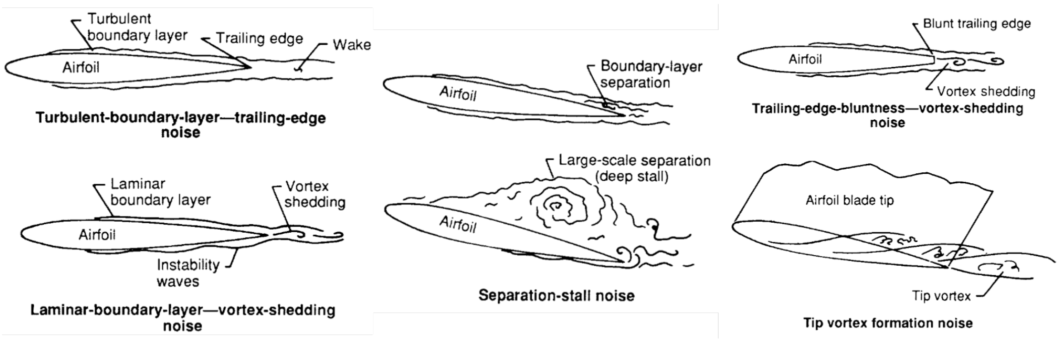

Figure 4.6: Breakdown of blade self-noise sources, from [10]

data obtained for the NACA 0012 airfoil. This airfoil was tested over a wide range of Reynolds numbers, Mach numbers, and angles of attack. The boundary layer data obtained from the experimental study of the NACA 0012 airfoil was utilized to perform an empirical curve fit and normalize the measured airfoil self-noise. The BPM method was initially developed for application to airfoils but was later extended to rotor blades under the assumption that a rotor blade can be divided into individual sections resembling a 2D airfoil under the same inflow conditions [11]. However, when it comes to low-Re rotors, the airfoil sections can largely deviate from the NACA0012 profile, in terms of thickness and camber distributions [131]. Therefore, the current study suggests utilizing the boundary layer data from the actual airfoil sections of the rotor to replace the empirical NACA 0012 curve fits originally used. This approach was inspired by similar implementations carried out by Whelchel [120], wherein the boundary layer data was computed using an XFOIL-based BEMT model, and by Jung et al. [49], where predictions were made using 2D RANS simulations of the respective airfoil sections. The latter method is adopted in the current study and explained below.

Figure 4.7 shows a flowchart depicting the framework used in the current study to predict total noise. The left-hand side of the flow-chart has already been discussed in the previous section. For broadband noise prediction, the BPM method requires inputs of aerodynamic parameters such as inflow velocity, effective angle of attack, and boundary layer

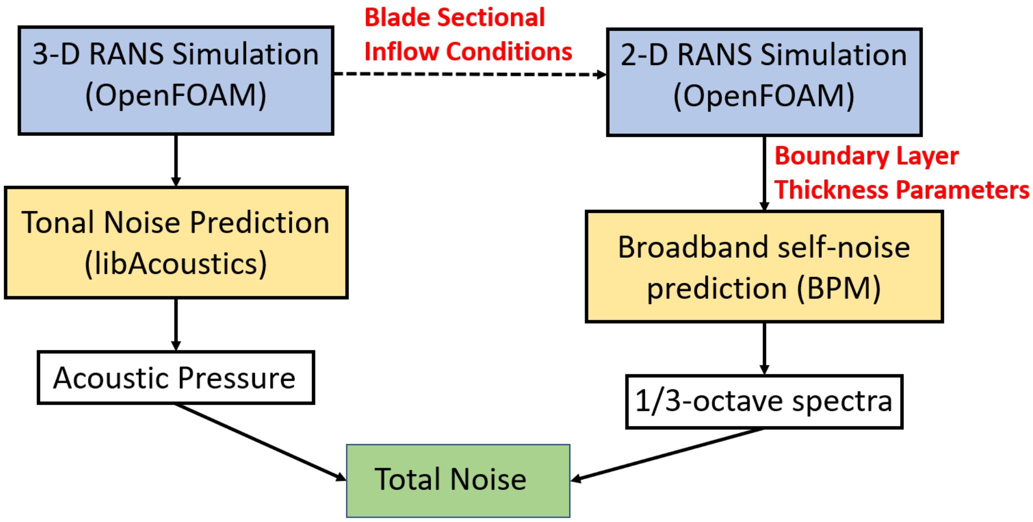

Figure 4.7: Flowchart for tonal+broadband noise prediction, adapted from [49]

parameters of thickness (δ) and displacement thickness (δ^*) at the trailing edge. A series of two-dimensional incompressible URANS simulations for different spanwise rotor sections are conducted for a range of angles of attack. The boundary layer thickness and displacement thickness are computed for each of these cases, thereby providing a look-up table. The Reynolds number and velocity inputs of the two-dimensional simulation is obtained from the inflow conditions encountered by the corresponding spanwise section, based on the operating RPM and advance ratio. Since there is no direct method to calculate the effective angle of attack (α_e)in a three-dimensional simulation, it is calculated using an iterative method that uses the information obtained from the 2D simulation to provide an approximation. This technique proposed by Jung et al [49] is expressed in the equations below.

$$CL_{section} = C_{l\alpha} \times \alpha_e + C_{l\alpha\ =\ 0^\circ} \tag{4.4}$$

$$CL_{section} = C_N \times \mathrm{Cos}(\beta - \alpha_e) - C_C \times \mathrm{Sin}(\beta - \alpha_e) \tag{4.5}$$

Equation (4.4) assumes a linear relation between the 2D lift and angle of attack, where $C_{l\alpha}$ indicates the two-dimensional lift-curve slope and $C_{l\alpha\ =\ 0^\circ}$ is the lift coefficient at zero angle

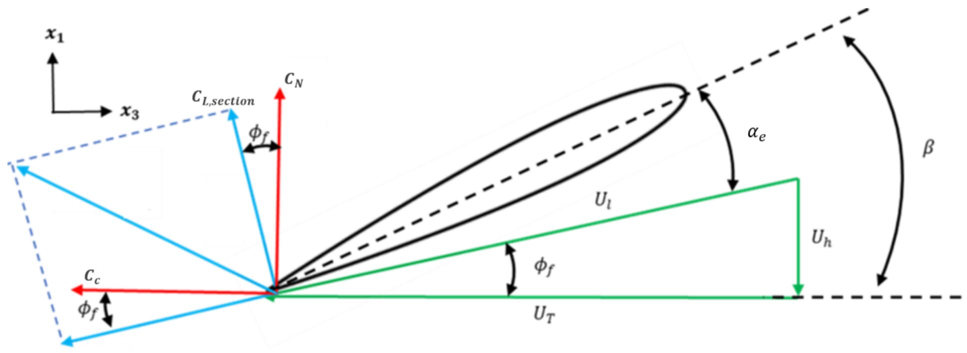

Figure 4.8: Forces encountered at a blade section with a finite inflow, from [120]

of attack. Equation (4.5) gives the three-dimensional sectional lift as a function of sectional normal and tangential forces. Figure 4.8 shows the different components of forces acting on a blade section, where β is the blade pitch angle, ϕ_f is the induced angle of attack and α_e is the effective angle of attack. The non-linear equation obtained form the three-dimensional forces is thereby solved iteratively with the help of the additional two-dimensional lift equation. Finally, at the calculated α_e the boundary layer parameters are extracted using the look-up table and input into the BPM code. Noise using this method is predicted in the $1/3_{rd}$ octave spectra.

The mesh for the 2D simulations was created using Pointwise and automated to generate it for different spanwise sections at various angles of attack using a Glyph script. Each mesh was generated with a $y^+(1)$ value of 0.8 to ensure good resolution in the boundary layer. The mesh close to the airfoil was an O-type structured grid while in the far-field was an isotropic unstructured grid that used the “advancing front ortho” algorithm. Care was taken to ensure the grid in the boundary layer followed the true wall-normal direction as suggested by Constenoble et al. [22]. Figure 4.9 shows the grid at a sample section belonging to the T-motor propeller. It also depicts the boundary layer extraction line that is seen to align well with the wall-normal mesh. The boundary layer parameters were extracted at 95% of the chord length for all sections.

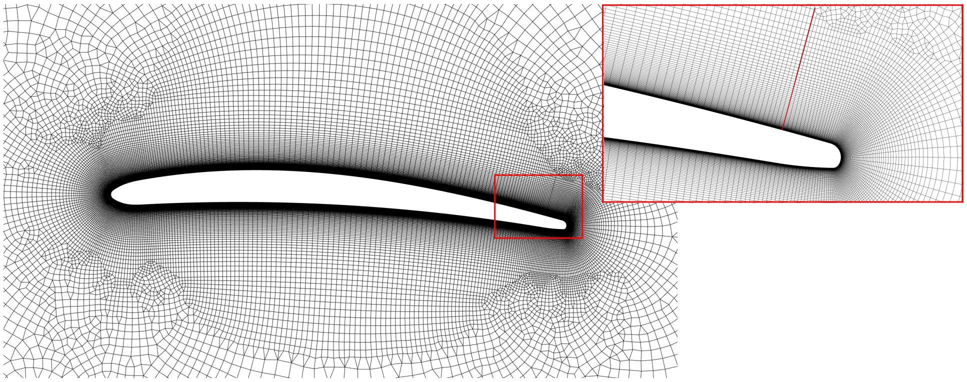

Figure 4.9: Boundary Layer Mesh for 2D-URANS simulation; Boundary layer extraction line shown to be aligned with the wall-normal mesh

Finally, the current study aims to also investigate the efficacy of both fully turbulent and transition models in predicting broadband noise. Therefore, the 2D RANS simulations are conducted using the k-ω SST fully turbulent model and the SSG/LRR-ω-γ transition model. The boundary layer thickness at the airfoil trailing edge is extracted using parameters available from the respective turbulence model. For the fully turbulent model, turbulent kinetic energy (k) is used to identify the boundary layer edge. The turbulent quantity possesses a high value within the boundary layer and diminishes to very low values outside the boundary layer. The second derivative of k with respect to the wall-normal distance is computed to identify the inflection points, and the boundary layer edge is determined to be the point where the last inflection occurs. On the other hand, the transition model is capable of predicting both laminar and turbulent boundary layers. Therefore, it utilizes turbulent kinetic energy (k) for turbulent regions and intermittency (γ) in laminar regions to determine the boundary layer thickness. Unlike k, intermittency (γ) remains low within the boundary layer and increases to a value of 1 as it approaches the boundary layer edge. The same gradient-based technique is used to identify the boundary layer edge with γ as well.

Chapter 5

Computational Aerodynamic Analysis of low-Re Propellers

This chapter applies the proposed transition turbulence model, SSG/LRR-ω-γ, on two different propellers. The predictions made by the model are compared against other turbulence models to study the effect of turbulence modeling on the prediction of aerodynamic characteristics in low-Re propellers. The propellers are analyzed at different operating conditions, which helps gain a better understanding of how Reynolds number, RPM and advance ratio tend to influence propeller performance.

5.1 Test Case I : Delft-APC Propeller

Grande et al. [40] presented oil flow visualizations and PIV flow measurements at various advance ratios for RPM = 4000. In this study, two of the tested advance ratios were considered and have been listed in Table 5.1. The operating Reynolds number at 60% spanwise section has also been reported in the table.

Table 5.1: Operating Conditions for the Delft-APC Propeller Simulations

RPM	**Inflow** (m/s)	**J**	Re_{60}
4000	4.8	0.24	77300
4000	12	0.6	80500

5.1.1 Grid Independence Study

Initially, a grid independence study was carried out by considering surface spacing, wall-normal resolution and volumetric cell size in the overset region. These parameters were chosen to ensure that the grid in the near-wall region as well as in the wake is well resolved. Surface spacing further involved parameters like leading and trailing edge spacing, chordwise and spanwise resolution. With respect to wall-normal resolution, the wall y^+ and number of anisotropic layers were refined. Finally, the volumetric region in the background mesh that encompasses the moving mesh was refined as a factor of the chord-length at the 60% spanwise section. All cases in the grid study were analyzed using the proposed SSG/LRR-ω-γ model.

Aerodynamic performance quantities of thrust and torque coefficients were considered to assess grid independence. Figure 5.1 (a) shows the convergence of thrust and torque over the course of the simulation. The kink in the plot seen at the 5^{th} rotor revolution is a result of activating turbulence as discussed in the previous chapter. Furthermore, the numerical schemes are set to first-order accurate once the turbulence is activated to ensure solution stability. As the simulation progresses, the numerical schemes are gradually changed to second-order accurate. The second kink in the convergence plot, observed around the 7^{th} revolution marks the change from first-order to second-order accurate. Beyond the 10^{th} revolution, the temporal scheme was also changed from *Euler* to *Crank-Nicolson* with a coefficient of 0.5. The convergence plot does not show a significant difference with this change, indicating that the SSG/LRR-ω-γ solution is more sensitive to the order of the convection schemes than to the temporal scheme.

Global aerodynamic quantities of thrust and torque were used to conduct the grid-independence study. The total thrust and torque are calculated by taking the average over the last revolution. These average values were non-dimensionalized using the expressions given in (5.1)

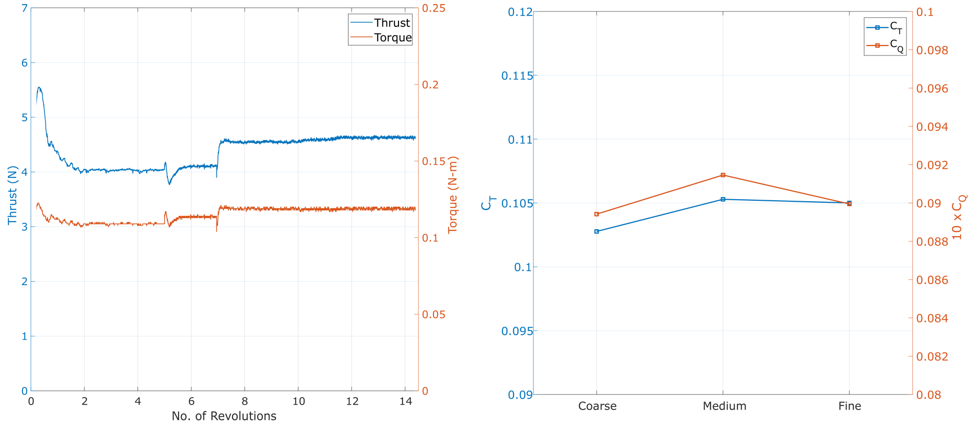

(a) (b)

Figure 5.1: (a) Thrust and Torque Convergence (b) Grid Independence Study performed using the SSG/LRR-ω-γ model

to give the thrust and torque coefficients respectively.

$$C_T = \frac{T}{\rho\ n^2\ D^4}; \quad C_Q = \frac{Q}{\rho\ n^2\ D^5} \tag{5.1}$$

Here, n is the rotational rate (in r.p.s) and D is the rotor diameter. Figure 5.1 (b) shows the grid convergence study that was conducted on the rotor at $J = 0.24$. The "fine" grid was chosen for the remainder of the study. It has a chordwise spacing of 0.013 c, where c is the chord-length at the 60% spanwise section. Further, the fine grid has a $y^+(1) = 0.8$ and the resolution in the overset and surrounding region were set to a length of $0.1c$. The total resolution of the chosen grid is equal to approximately 37 million cells. Each case was executed using a total of 7 nodes, with 128 processors allocated to each node.

5.1.2 Thrust and Torque Prediction

Figure 5.2 shows the thrust and torque coefficients predicted by different turbulence models at the two advance ratios. The black dotted lines in the figure indicate the measured values of C_T and C_Q. The experimental measurement uncertainty was quantified at 1% for thrust and

0.05% for torque. These uncertainties are represented by error bars along the ordinate of each bar plot. However, the uncertainty bar for torque may not be clearly visible due to its small magnitude. At the lower advance ratio of $J = 0.24$, all models, except the fully turbulent SA model exhibit very similar behavior and prediction accuracy in thrust and torque values. The difference between fully turbulent and transition models are minor. On the other hand, at the higher advance ratio, the difference between fully turbulent models and transition models becomes very evident. The transition models k-ω γ-$Re_{\theta t}$ and SSG/LRR-ω-γ, exhibit very similar trends across both cases.

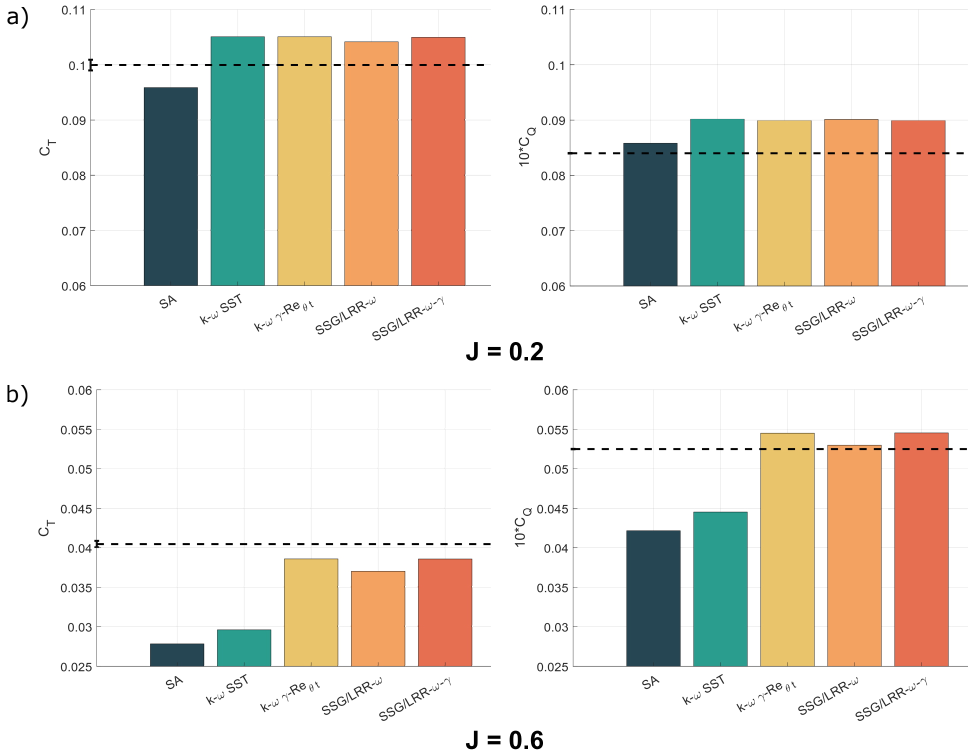

Figure 5.2: Predicted C_T (left) and C_Q (right) at a) $J = 0.24$ and b) $J = 0.6$

To provide a more detailed assessment of prediction accuracy, Figure 5.3 illustrates the percentage error for each model across the two test cases. The SA model seems to be the most accurate at $J = 0.24$ and least accurate at $J = 0.6$. Similarly, the k-ω SST fully turbulent model demonstrates reasonable accuracy, comparable to other models at the lower advance ratio. However, it exhibits poor predictions at the higher advance ratio. It is important to acknowledge the different scales on the y-axis for the two advance ratios, indicating that the percentage errors for the linear-eddy viscosity, fully-turbulent models are quite high at the higher advance ratio. The SSG/LRR-ω fully turbulent model displays slightly erratic behavior, showing good accuracy in thrust at $J = 0.24$ and in torque at $J = 0.6$, however, does consistently better than the k-ω SST model. On the other hand, both transition models demonstrate good prediction accuracy within acceptable limits of approximately 5-7% across different operating conditions. It is observed that as the order of the turbulence models increases, the performance of fully turbulent models improves, particularly at the higher advance ratio. Such distinctions are less apparent for transition models. In summary, fully turbulent models exhibit considerable sensitivity to changes in advance ratio, while transition models appear to be less affected by such variations. Assessing the performance of turbulence models solely based on global integrated quantities may not be adequate, warranting a more detailed examination of their predicted flow features, as discussed in the subsequent sections.

5.1.3 Blade Surface Analysis

Figure 5.5 presents the distribution of instantaneous skin friction magnitude along with limiting streamlines over the suction surface of the blade at the two advance ratios examined in the study. The oil-flow visualization from the study by Grande et al. [40] is also included for comparison. In the experimental contour, the light green area, where oil accumulation is highest, indicates the separated region. At the lower advance ratio, the occurrence of a Laminar Separation Bubble (LSB) is clearly depicted, while at the higher advance ratio, the flow is mostly separated with possible reattachment close to the trailing edge. Efforts were made to replicate the experimental perspective as closely as possible in the presented

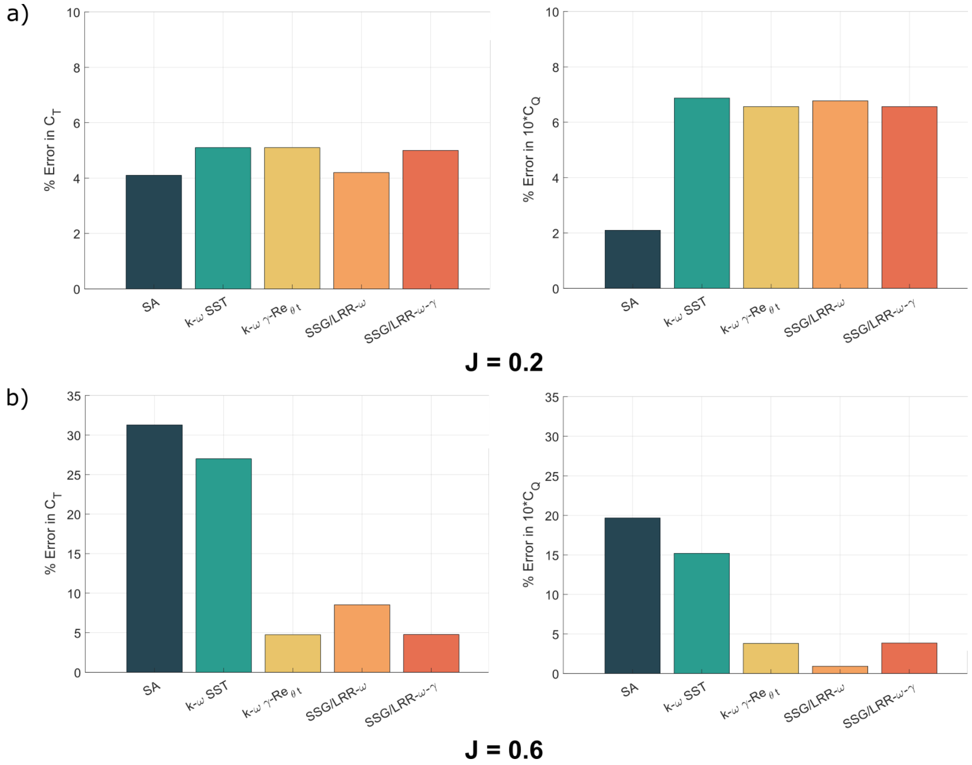

Figure 5.3: Percentage error in predicted C_T (left) and C_Q (right) at a) $J = 0.24$ and b) $J = 0.6$

CFD contours. In the model predictions, the convergence of streamlines indicates the onset of flow separation, which is also denoted by a sudden reduction in skin friction coefficient levels (blue region). At the lower advance ratio, the predicted onset of separation is nearly identical across all models, except SA which predicts the separation onset to be slightly more downstream in the chordwise direction. The onset of separation appears to align closely with the experimental contour near the rotor tip. However, in further inboard regions, the separation line diverges from the experimental contour. This discrepancy can be attributed to slight differences in perspectives as well as higher experimental uncertainties inherent in oil-flow visualizations. The streamline pattern within the separated regions tend to be radial, indicating that centrifugal force is the predominant force. All models predict flow separation near the root section, consistent with the experimental contour and indicated by largely radial profiles of the streamlines. However, the SA model tends to comparatively predict a more attached profile close to the root, with separation occurring only very near to it. Further, the separated region in the chordwise direction is much larger for the SA model compared to other models, all of which exhibit very similar lengths of separated flow regions along the span. Flow reattachment in the predicted contours is depicted by the change in the streamline pattern from predominantly radial to a mix of streamwise and radial. The chaotic nature of the flow downstream of the chord, within the reattached region, also suggests possible vortex shedding and is thereby fluctuating in nature.

In the experiment, flow separates earlier for the lower advance ratio and moves downstream in the chordwise direction as the advance ratio increases due to a decrease in the local angle of attack. This effect is well captured by all models. However, similar to the previous case, the SA model predicts separation onset further downstream of the local chord compared to the other models. The comparison between fully turbulent linear eddy viscosity models (SA and k-ω SST) with the rest reveals that they tend to predict larger regions of separation. This is evident from the greater extent of radial flow seen in the streamline patterns. The differences observed in the surface flow patterns between these two fully turbulent models, in contrast to the others, could potentially explain the discrepancies seen in the global thrust and torque predictions at the higher advance ratio. Finally, the experimental contours seem to show some reattachment very close to the trailing edge, especially in regions closer to the rotor tip. The transition models and the fully turbulent SSG/LRR-ω model seem to predict this reattachment, indicated by the increase in skin-friction and the change in streamline pattern. At both advance ratios, the predictions from both transition and turbulent models depict instances of both separation and reattachment, posing a challenge in definitively identifying whether the separated regions observed in transition models indeed represent laminar separation bubbles solely based on surface flow contours. Hence, the following section

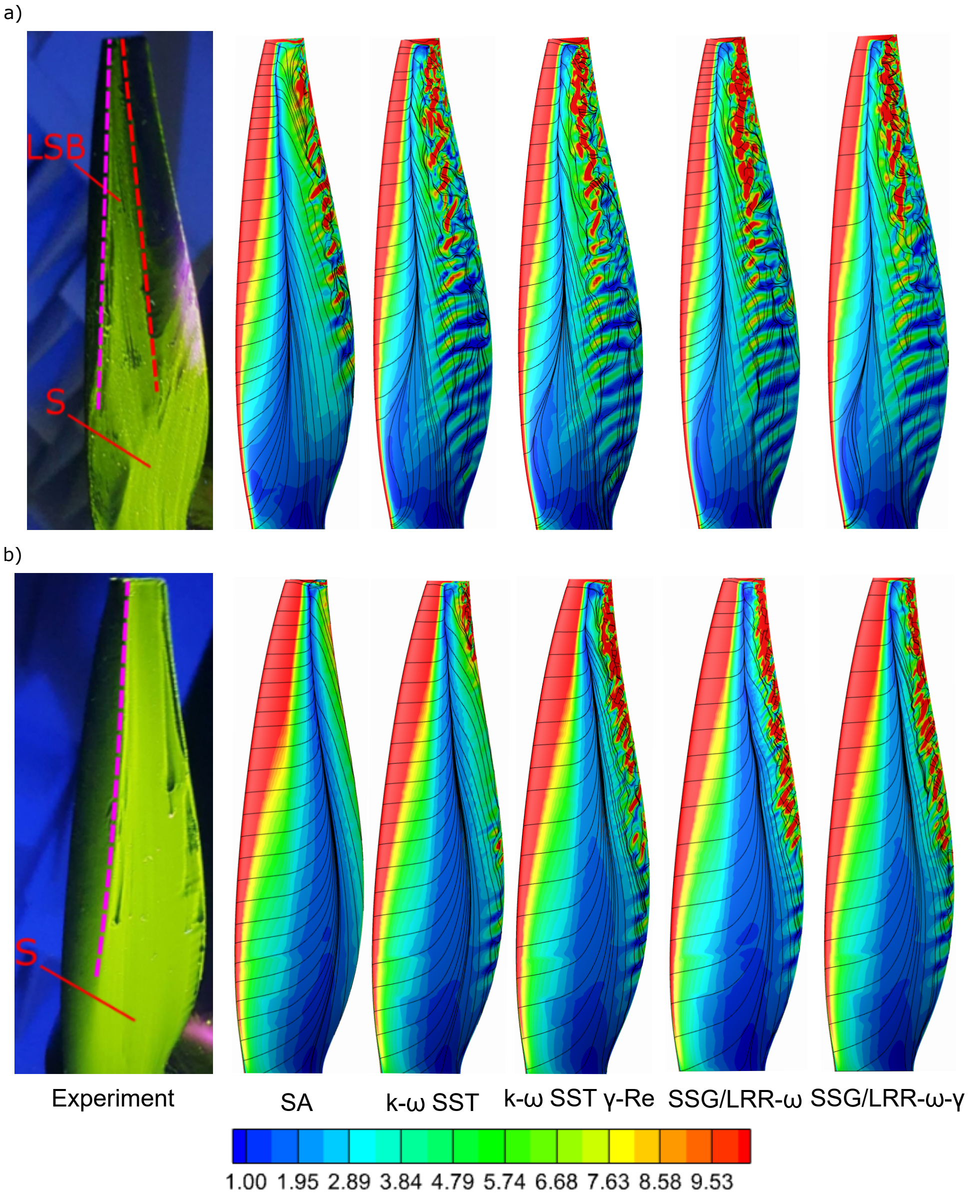

Figure 5.4: Instantaneous skin friction contours with limiting streamlines on the suction side for a) $J = 0.24$ and b) $J = 0.6$. Experimental contours from [40]

delves into a more comprehensive examination of flow characteristics along the spanwise sections.

Figure 5.5 shows the skin friction contours at different rotor azimuthal positions. It is evident that there are flow fluctuations in the reattachment region for all models, while the

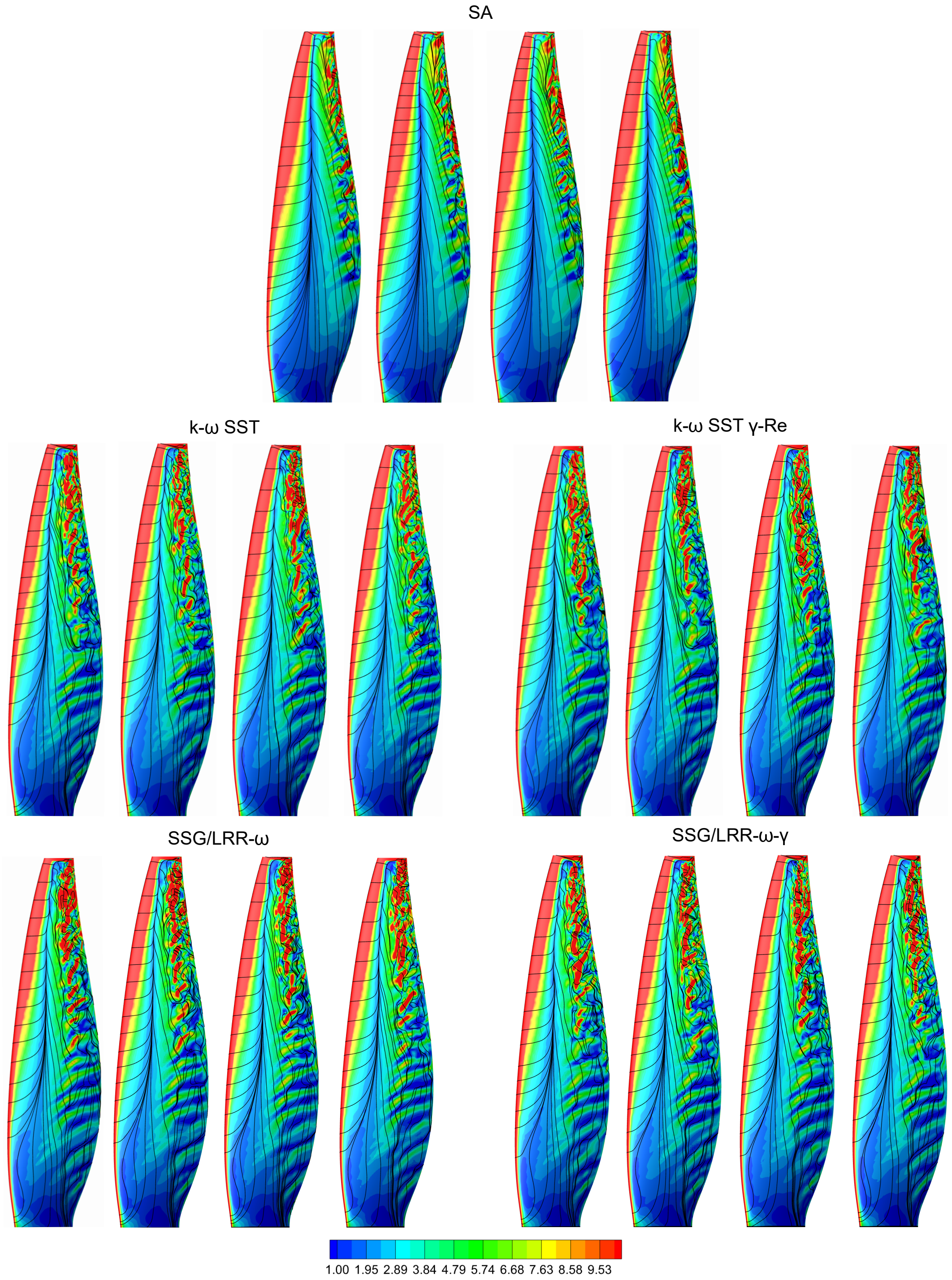

Figure 5.5: Skin friction contour on the suction side for $J = 0.24$ at blade azimuth angles of $\phi = [0°, 90°, 180°, 270°]$ (left to right) predicted by different turbulence models

remaining flow features, like attached flow regions, separation onset, etc., along the blade surface remain consistent over time. This behavior is observed at the higher advance ratio as well and hence hasn't been presented here.

5.1.4 Sectional Flow Analysis

Grande et al. [40, 41] also carried out PIV measurements at the spanwise section of $r/R = 60\%$. About 500 samples (images) of flow measurements were obtained using a spectral phase-locked mode and averaged out to produce velocity distributions at this spanwise plane. Figure 5.6 shows the rms velocity field obtained from the measurements at $J = 0.24$ and $J = 0.6$. The measured contours do not include the blank white region very close to the blade surface, as these areas are associated with high uncertainty in measurement. These contours offer a qualitative evaluation of the transition onset in the flow. The point where the root mean square (RMS) velocity begins to significantly increase marks the onset of turbulence. This point tends to shift downstream along the chord as the advance ratio increases and the local angle of attack decreases. In figure 5.6, it is seen that the turbulence onset for $J = 0.24$ is at the chordwise location of $x/c \approx 0.8$, where the RMS velocity becomes 12% of the free-stream value and for $J = 0.6$, onset location is very close to the trailing edge ($x/c \approx 1$), where the RMS velocity was observed to reach 22% of the freestream value [41]. In the present analysis, these contours serve as a valuable tool to visualize turbulence onset and evaluate which turbulence model effectively captures this phenomenon.

Since a direct comparison to the quantity of U_{rms} is not feasible with a URANS simulation, this study suggests employing a multi-variable approach to qualitatively pinpoint the onset of turbulence and the transition mechanism. The variables identified to carry out this visualization study include non-dimensionalized turbulent kinetic energy ($\tilde{k}$) contours, relative

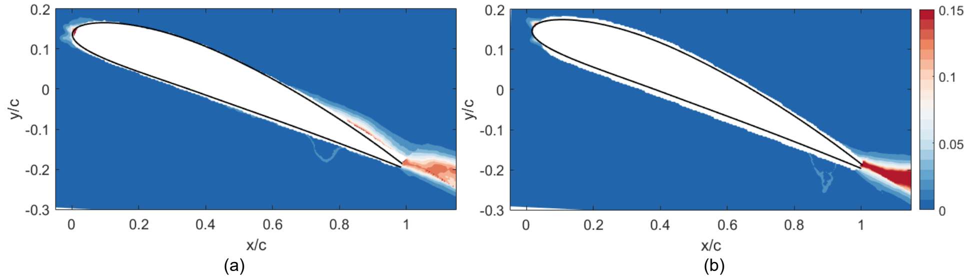

Figure 5.6: Measured RMS Velocity (U_{rms}/U_{∞}) at spanwise section of $r/R = 60\%$ at a) $J = 0.24$ and b) $J = 0.6$ from [41]

velocity vectors and intermittency (γ) contours. Figure 5.7 illustrates the instantaneous $\tilde{k}$ contours for different turbulence models at $r/R = 60\%$. This representation divides the local kinetic energy (k) by the freestream value at the inlet (k_{inlet}). It serves as a useful marker to indicate regions of turbulence onset in RANS simulations by identifying the point where the local k exceeds the value at the inlet by roughly an order of magnitude [46].The contour levels in the figure do not exceed a maximum value of 7 to facilitate clear visualization. The SA model has not been included in this analysis since it does not possess information about turbulent kinetic energy. The fully turbulent models, k-ω SST and SSG/LRR-ω, exhibit high levels of turbulence all along the chord length on both the suction and pressure sides, indicating a fully turbulent boundary layer. The boundary layer near the leading edge is typically very thin, and therefore, the contour levels are not discernible in those regions. In contrast, the transition models begin to display high levels of turbulence only beyond a certain point along the chord length. On the suction side, the levels of $\tilde{k}$ rises to significant levels at $x/c \approx 0.85$ for the k-ω SST γ-$Re_{\theta t}$ model and $x/c \approx 0.9$ for SSG/LRR-ω-γ. Along the pressure side, the turbulence levels remain very low, implying that these regions could have a laminar boundary layer. Figure 5.8 provides a zoomed-in view of the region near the trailing edge along with the relative velocity vector field depicting the direction of the flow within the boundary layer. Interestingly, all models seem to predict flow separation at $x/c \approx 0.4$, followed by reattachment at $x/c \approx 0.75$ and finally separation at $x/c \approx 0.85$. In the case of fully turbulent models, this represents a wholly turbulent separation and reattachment. To understand the mechanisms of flow separation and reattachment in transition models, figure 5.9 presents their corresponding intermittency (γ) contours. Regions with low values of intermittency, marked in blue, indicate laminar flow, while regions with very high intermittency, marked in red, indicate a fully turbulent flow. It is clear that regions close to the leading edge and whole of the pressure side are fully laminar for both models. Around $x/c \approx 0.4$, the laminar boundary is seen to separate, marking a laminar separation. For the SSG/LRR-ω-γ model, the laminar layer seems to reattach at $x/c \approx 0.75$ and later on separate to finally transition to turbulent flow, well in line with the previous plots. This is not as distinct in the k-ω SST γ-$Re_{\theta t}$ model. Nevertheless, it is safe to conclude that the transition models capture the occurrence of a laminar separation bubble with regions of some re-laminarization at this operating condition.

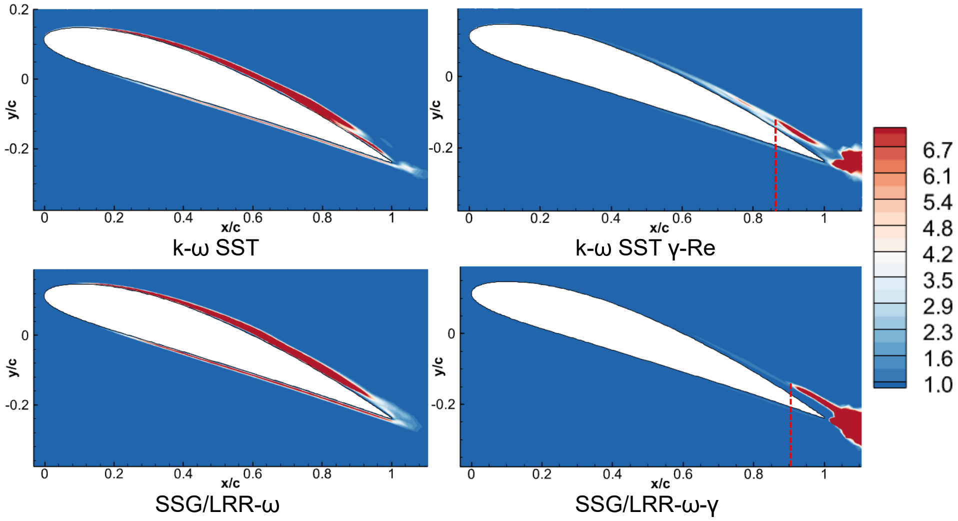

Figure 5.7: Turbulent kinetic energy ($\tilde{k}$) at spanwise section of $r/R = 60\%$ for $J = 0.24$

Similar observations as $J = 0.24$ can be made for the higher advance ratio presented in figure 5.10. The fully turbulent models are seen to predict a thicker turbulent boundary layer on the pressure side due to the lower local angle of attack. The k-ω SST γ-$Re_{\theta t}$ predicts a predominantly laminar flow all along the chord, in line with the experimental observations,

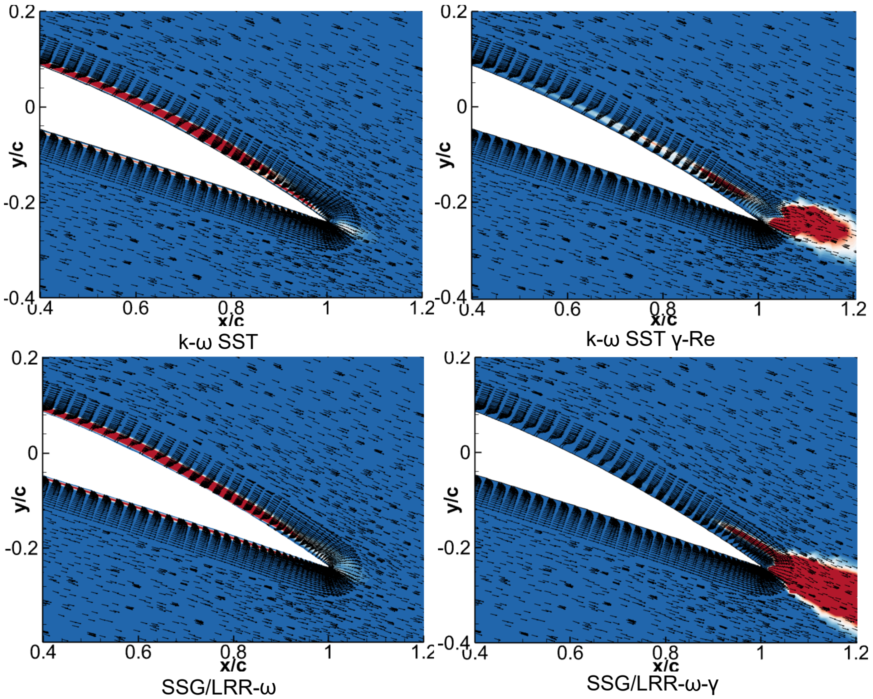

Figure 5.8: Turbulent kinetic energy ($\tilde{k}$) with relative velocity vectors close to the trailing edge at spanwise section of $r/R = 60\%$ for $J = 0.24$

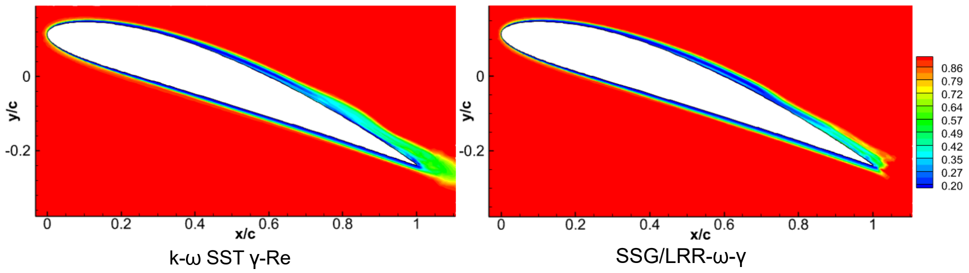

Figure 5.9: Intermittency (γ) at spanwise section of $r/R = 60\%$ at $J = 0.24$

but fails to predict any turbulence onset close to the trailing edge. On the other hand, the SSG/LRR-ω-γ model predicts turbulence onset first at $x/c \approx 0.85$ and again at $x/c \approx 0.98$. The relative velocity vectors in figure 5.11 show that all models predict a fully attached flow until $x/c \approx 0.65$, beyond which the flow is seen to separate with no reattachment. The intermittency contours in figure 5.12 shows the laminar boundary layer separation at $x/c \approx 0.65$ for both models. Downstream of the separation, the SSG/LRR-ω-γ is seen to predict regions of re-laminarization and turbulence, which is reflected in the turbulent kinetic energy contour as well. These patches of turbulence and re-laminarization are also seen in the intermittency contour for the k-ω SST γ-$Re_{\theta t}$ model, however, the levels of turbulent kinetic energy do not seem to reflect this effect.

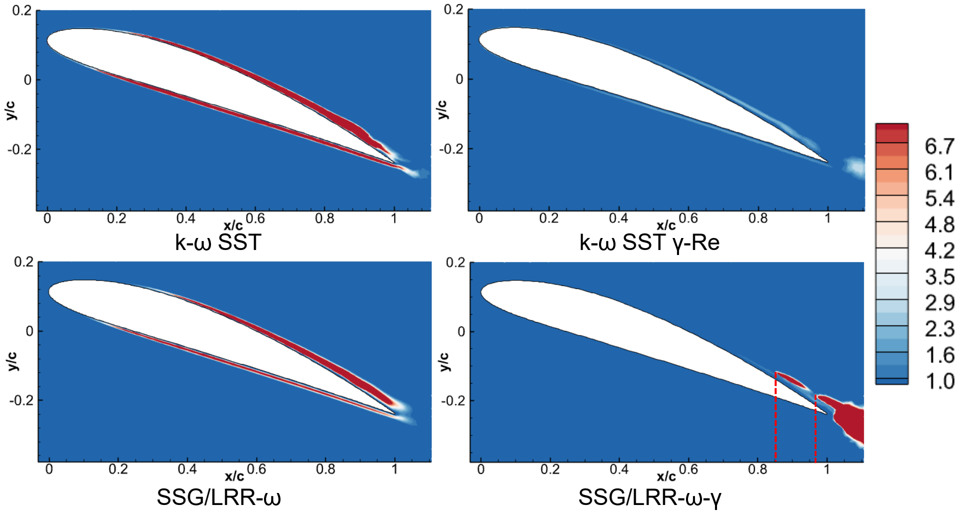

Figure 5.10: Turbulent kinetic energy ($\tilde{k}$) at spanwise section of $r/R = 60\%$ for $J = 0.6$

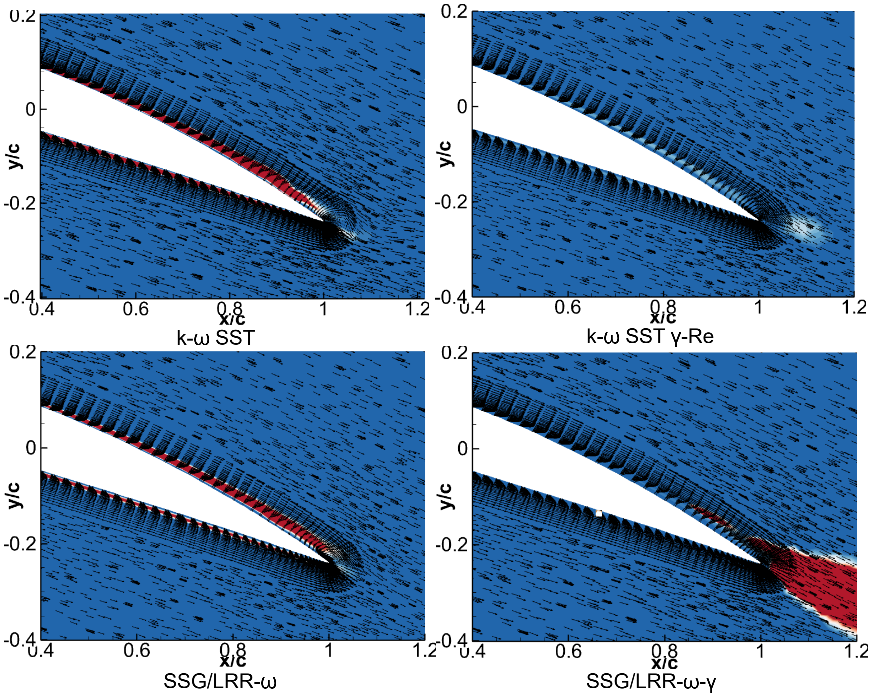

Figure 5.11: Turbulent kinetic energy ($\tilde{k}$) with relative velocity vectors close to the trailing edge at spanwise section of $r/R = 60\%$ for $J = 0.6$

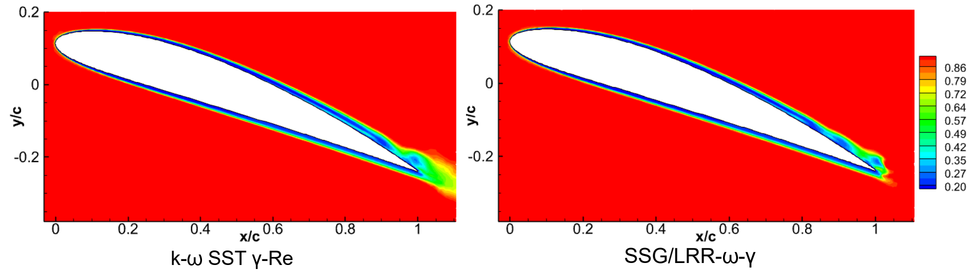

Figure 5.12: Intermittency (γ) at spanwise section of $r/R = 60\%$ at $J = 0.6$

Finally, an important distinction can be made for the two transition models in the wake region of the spanwise section for both operating conditions. In figure 5.8, the k-ω SST γ-$Re_{\theta t}$ predicts a narrow wake which tends upwards, while the SSG/LRR-ω-γ model is seen to predict a fuller wake that is in line with the experimental contour in figure 5.6(a). Similarly, in figure 5.11, the RST-based model predicts a full wake, slightly thicker than that seen in the lower advance ratio, while the SST-based model fails to predict any wake at all. This behavior can be attributed to the lack of Galilean invariance in the SST-based model formulation. Not having a coordinate independent formulation can lead to errors in the prediction of local streamline direction and pressure gradients along the streamline. It also leads to incorrect estimation of the turbulence intensity, which is directly proportional to turbulent kinetic energy and is calculated using the freestream velocities, as opposed to the local velocity [46]. On the other hand, the RST-based model overcomes these drawbacks due to its Galilean invariant formulation, which makes all its variables dependent on local quantities, thereby making it more suitable for flows with moving walls such as propellers.

The sectional analysis has demonstrated that transition models successfully predict regions of laminar boundary layer, laminar separation, reattachment and transition to turbulence. However, the location of transition onset predicted by both models do not perfectly align with the experimental observations. In the future analysis, a quantitative method to extract the location of transition onset will be introduced to gain more confidence in these model predictions.

5.2 Test Case II : T-Motor CF 30x10 Propeller

The T-motor propeller operates in a higher Reynolds number regime compared to the Delft-APC propeller. The operating conditions for the test cases considered for this propeller are provided in Table 5.2, which includes hover and low inflow cases. Thrust and torque data are available from experiments conducted at the Virginia Tech Open Jet Wind tunnel [119, 120]. It was noted by Pisharoti et al. [91] that the inlet dimensions of the open jet tunnel (0.76 m × 0.76 m) are almost equal to the diameter of the rotor ($D = 0.762$ m) being investigated. As the tunnel inflow velocity increases, the interaction of the shear layer of the inlet with the rotor increases, thereby increasing the complexity in the flow field. Therefore, cases with higher inflow are not being studied. Moreover, as the experiment lacked flow visualization data, only global quantities were utilized to validate the model predictions. The remaining flow analyses for this propeller have been conducted to offer purely qualitative insights.

It is also worthy to note that a larger rotor diameter warrants a larger domain and thereby, a larger mesh resolution, resulting in higher computational costs. Therefore, all four turbulence models from the previous case have not been considered in this study due to the computational expense associated with this rotor. Instead, only the fully turbulent k-ω SST model and the proposed SSG/LRR-ω-γ model have been considered from now on.

Table 5.2: Operating Conditions for the Delft-APC Propeller Simulations

RPM	**Inflow** (m/s)	**J**	Re_{75}
2000	0	0.0 (hover)	191000
2000	5.04	0.1978	192000

5.2.1 Grid Independence Study

The grid independence study for the T-motor propeller was carried out on the hover case using the SSG/LRR-ω-γ model. Figure 5.13(a) shows the thrust and torque convergence plot for one of the grids. The computation for the hover case exhibits a longer duration to reach a steady state compared to the finite inflow case studied for the previous rotor. The abrupt change at the 5^{th} rotor revolution corresponds to the activation of turbulence. Subsequently, between the 5^{th} and 10^{th} revolutions, the time step is decreased and the numerical schemes are gradually adjusted from first-order to second-order accuracy. After the 10^{th} rotor revolution, the time step is further reduced to 0.25° of rotor revolution. Beyond this point, the quantities begin to stabilize, reaching a steady state by the 12.5^{th} rotor revolution. The simulation is extended until 14.5 rotor revolutions to ensure that the stable solution is computed over a sufficient duration.

Figure 5.13(b) depicts the grid convergence study carried out using three subsequently refined grids. The same grid parameters considered for the Delft-APC propeller were considered for the current analysis too. The "fine" grid was chosen for the remaining analysis which has a total resolution of $\approx$ 82 million cells. It has a chordwise spacing of 0.006 c, where c is the chord-length at the 75% spanwise section. Further, the fine grid has a $y^+(1) = 0.8$ and the resolution in the overset and surrounding region were set to a length of $0.06c$. Each case was executed using a total of 10 nodes, with 128 processors allocated to each node.

5.2.2 Thrust and Torque Prediction

Figure 5.14 illustrates the coefficients of thrust and torque measured at RPM$= 2000$, accompanied by the corresponding measurement uncertainty. The predictions made by k-ω SST and SSG/LRR-ω-γ models have been indicated using red and black markers respectively.

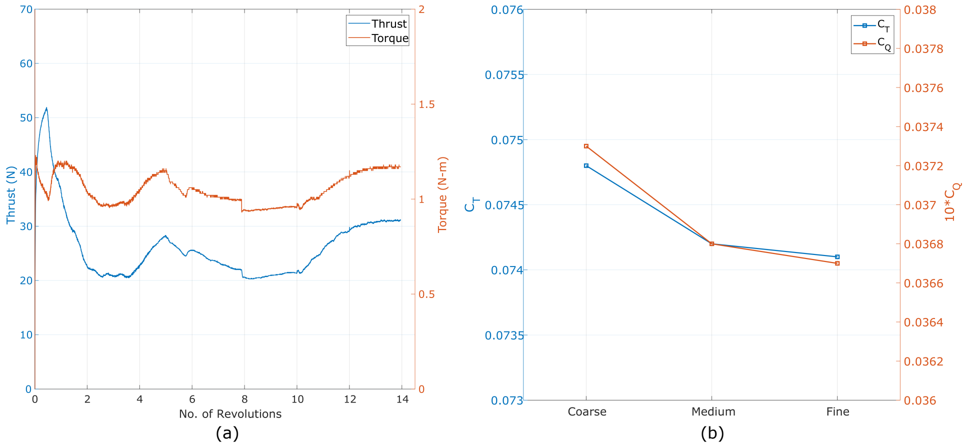

Figure 5.13: (a) Thrust and Torque Convergence (b) Grid Independence Study performed using the SSG/LRR-ω-γ model at hover

Both models seem to under-predict thrust and torque at the considered test conditions. Further, the prediction accuracy seems to deteriorate as the advance ratio increases. These prediction errors were quantified and are presented as bar graphs in figure 5.15. In both cases, the transition model seems to have a better prediction accuracy compared to the fully turbulent model. In contrast to the Delft-APC propeller case, the transition model error tends to rise with an increase in the advance ratio. However, the fully turbulent model exhibits a similar trend as observed in the previous case, where its error increases with J.

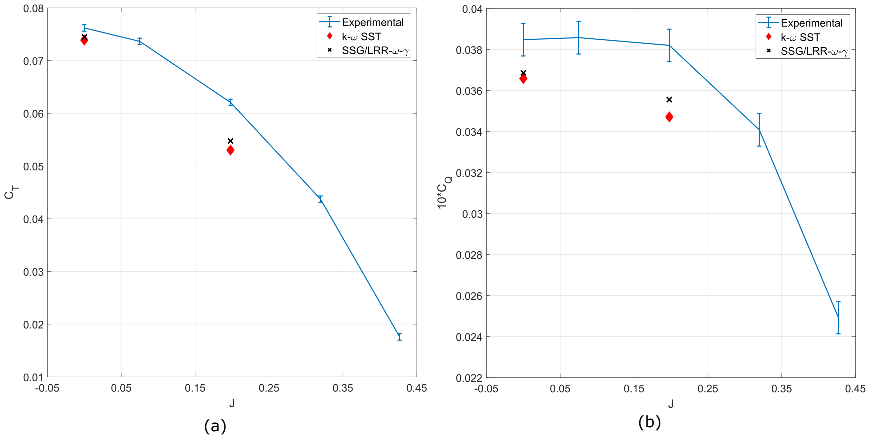

Figure 5.14: Predicted C_T (left) and C_Q (right) for the T-Motor 30×10.5 rotor at RPM=2000 [119, 120]

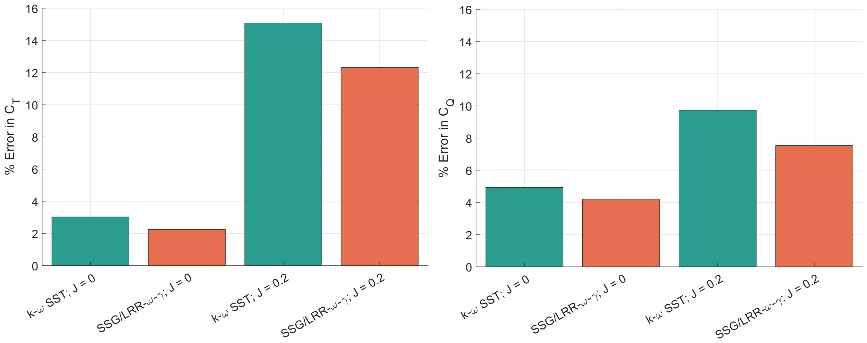

Figure 5.15: Percentage Error in C_T (left) and C_Q (right) for the T-Motor 30×10.5 rotor

5.2.3 Blade Surface Analysis

Figure 5.16 depicts the skin friction distribution over the suction surface of the T-motor blade. At hover, the contour and streamline patterns predicted by both models are fairly identical. Both models predicts a predominantly attached flow over most of the blade surface. Flow begins to separate at roughly 65% spanwise location and near the trailing edge in the chordwise direction. At the higher advance ratio, both models predict flow separation closer to the trailing edge, as is expected due to the decrease in the local angle of attack. There are some noticeable differences between the fully turbulent and transition model at this test condition. It is observed that the fully turbulent model predicts a larger separation region, as evidenced by the larger number of radial streamlines and an earlier onset of separation along the spanwise direction compared to the transition model. This is indicated by an earlier convergence of streamlines as well as a larger region of low skin friction coefficient in the k-ω SST model prediction. This could explain the much larger under-prediction of thrust and torque at the higher advance ratio by the fully turbulent model. This also indicates that the trend observed in the surface flow analysis for the larger rotor aligns with the behavior observed by the models in the previous test case.

Further investigations into the cross-sectional flow for the T-motor propeller have not been included, as the conclusions from the previous study remain valid, rendering additional

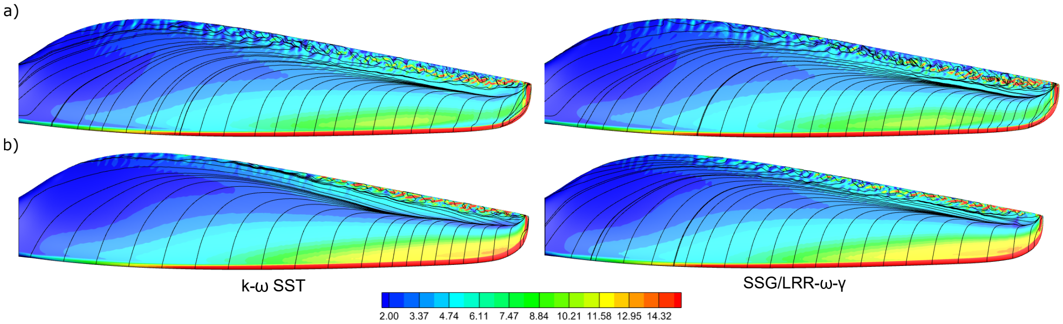

Figure 5.16: Skin friction with limiting streamlines on the suction side for $r/R = 60\%$ at a) Hover and b) $J = 0.2$

analysis redundant.

5.3 Conclusions

Aerodynamic analysis of two distinct propellers was conducted using various turbulence models, aiming for both quantitative and qualitative assessments to discern the impact of these models. Initial investigations into the prediction of aerodynamic performance revealed that transition models demonstrated good accuracy and robustness compared to fully turbulent models across different conditions. Furthermore, among the fully turbulent models examined, the RST-based model consistently demonstrated higher prediction accuracy compared to the linear eddy viscosity models. Analysis of the blade surface indicated a tendency for fully turbulent models to predict increased separation as the advance ratio rose, resulting in underestimations of thrust and torque at higher advance ratios. These trends persisted even with the larger propeller. Additionally, a qualitative examination of the Delft-APC propeller was undertaken to pinpoint the transition to turbulence. Although all models predicted similar flow separation and reattachment patterns, both transition models effectively captured the mechanism behind this separation and reattachment.In the comparison between the SST-based (k-ω γ-$Re_\theta t$) and RST-based (SSG/LRR-ω-γ) models, it was evident that the RST-based model offered better performance in approximating the trailing edge wake as a result of its Galilean invariant formulation. In conclusion, transition models seem to lend a greater advantage in terms of being consistent with their predictions and in capturing the underlying physics that define low-*Re* flows.

Chapter 6

Computational Aeroacoustic Analysis of low-*Re* Propellers

This chapter delves into the CFD-based aeroacoustic predictions facilitated by the current RANS framework. For the Delft-APC propeller, the proposed CFD-based broadband noise method is applied, investigating the impact of utilizing fully turbulent models versus transition models in predicting broadband noise across varying operating conditions. Subsequently, it assesses turbulence model predictions for the T-motor propeller, focusing on both tonal and broadband noise predictions, leveraging available experimental data that decomposes the components of tonal and broadband noise for this propeller [119]. The second case also provides a comparison with an XFOIL-BEMT based broadband noise prediction method.

6.1 Test Case I : Delft-APC Propeller

The CFD-based broadband noise prediction for the Delft-APC propeller is conducted for the two test conditions analyzed in the previous chapter. Since the propeller employs the NACA 4412 airfoil section across its entire span [15], the need to analyze every spanwise section along the blade, as proposed in the BPM method, is obviated. Instead, characteristic Reynolds numbers are tested for the airfoil at a range of angles of attack from $-10°$ to $10°$ to form a look-up table. The chosen Reynolds numbers (Re=$[3.5 \times 10^4, 8.5 \times 10^4]$) encompass the range of sectional Reynolds number experienced by each spanwise section for the two advance ratios considered in the study. The k-ω SST fully turbulent model and the SSG/LRR-ω-γ transition model have been chosen for this analysis.

6.1.1 Blade Self-Noise Prediction

2D URANS Analysis

Figure 6.1 presents the change in lift and drag coefficients with angle of attack for NACA4412. The lift curve slope predicted by the fully turbulent model is fairly constant, with the exception of highly negative angles of attack. On the other hand, the transition model seems to predict a largely variable slope. This is characteristic of a low Reynolds number airfoil which is heavily influenced by the occurrence of laminar separation bubbles, which reduced in size and moves upstream of the chord as the angle increases [6]. It is seen that the transition model predicts a higher lift compared to the fully turbulent model at higher angles of attack, with the exception of $Re = 35,000$. Conversely, at the negative angles of attack, the transition model consistently predicts lower lift compared to the fully turbulent model. Predictions made by Casalino et al. [15] at $Re = 80,000$ using their BEMT-based solver, *OptydB*, have been incorporated for comparison. Notably, both turbulence models tend to underestimate the lift coefficient, except for the fully turbulent model at extremely high negative angles of attack, where it overestimates the lift coefficient. The drag coefficient presented in figure 6.1(b) shows that the transition model consistently predicts higher drag compared to the fully turbulent model as well as the *OptydB* prediction. Figure 6.2 provides a comparison of the predicted velocity contours and streamlines at $Re = 80,000$ and $\alpha = 4°$. The streamlines depicted in the transition model shows the formation of a laminar separation bubble, while the fully turbulent model predicts a fully attached flow over the complete airfoil with a small

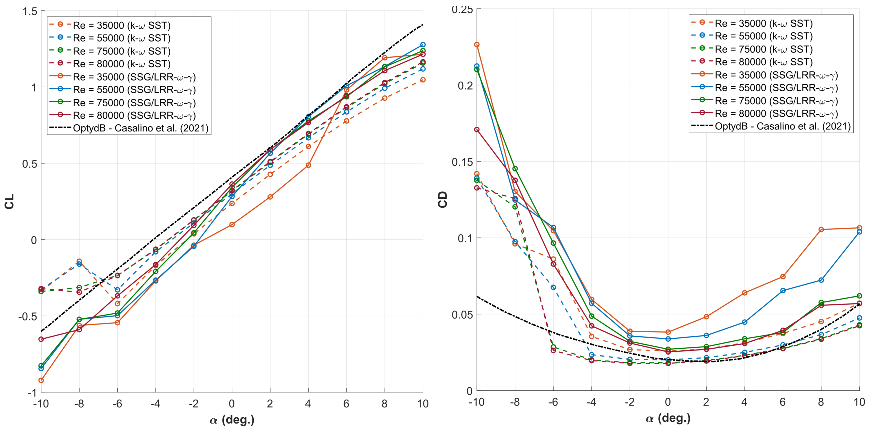

(a) (b)

Figure 6.1: Predicted a) C_L and b) C_D for NACA4412 at different Reynolds numbers

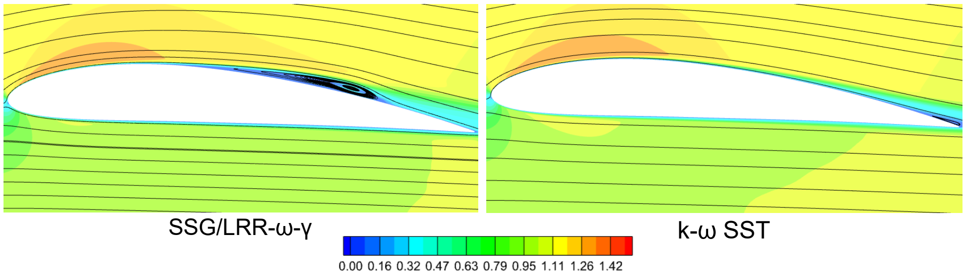

Figure 6.2: Velocity magnitude contour at $Re = 80,000$ and $\alpha = 4°$

separation at the trailing edge. This further justifies the varying lift curve slope modeled by the transition model which ideally provides a truer depiction of the flow compared to the transition model.

Figure 6.3 shows the predicted boundary layer parameters at different Reynolds numbers. The fully turbulent model predicts a steadily increasing profile of boundary layer thickness on the suction side and a decreasing profile on the pressure side with an increase in angle of attack. This trend is also reflected in its displacement thickness predictions. The transition model largely displays the same behavior with changing angle of attack and Reynolds number. However, it predicts a much larger thickness over the suction side compared to the fully turbulent model, which in turn manifests in the displacement thickness plots as well. On the pressure side, at higher angles of attack, it was observed that the transition model predicts

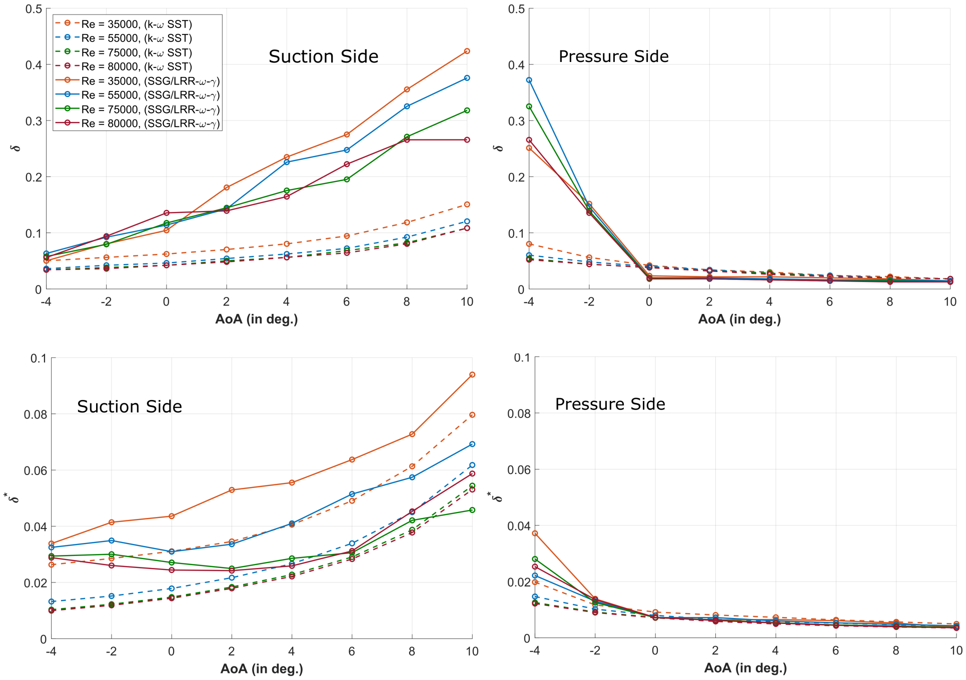

Figure 6.3: Predicted boundary layer thickness (top) and displacement thickness (bottom) for NACA4412 at different Reynolds numbers

a fully laminar flow and hence has a thinner boundary layer thickness compared to the fully turbulent model. At the negative angles of attack, however, the model suddenly begins to see laminar separation and vortex shedding on the pressure side, which rapidly increases the predicted thickness. At positive angles, the difference between the displacement thickness predicted on the pressure side by the fully turbulent model and transition model is relatively low.

3D Loading and Effective Angle of Attack Calculation (α_e)

From the 3D calculations discussed in the previous chapter, the surface loading was obtained. Figure 6.4(a) presents the sectional normal and tangential forces across the rotor blade predicted by the turbulence models at the two advance ratios. These were computed by extracting the sectional forces at each time step and averaging them over one rotor revolution.

At the lower advance ratio, the difference in predicted loading between the two turbulence models is negligible. However, at the higher advance ratio, a visible difference is observed between the two models. This difference is expected given that the global thrust and torque values depicted in Figure 5.2, which represent integrated values of these loading curves, show the same trend.

Values of the 2D lift-curve slope and sectional forces from the 3D loading distribution is plugged into equations (4.4) and (4.5) to compute the effective angle of attack (α_e) at each spanwise section. Figure 6.4(b) presents the final distribution of α_e predicted by the turbulence models along the spanwise direction for both advance ratios. As expected, the local angle of attack reduces with an increase in the advance ratio. The fully turbulent model generally forecasts a higher local angle of attack for the lower advance ratio compared to the transition models, except for sections close to the root and tip. Since the loading distribution is largely the same for both models at this advance ratio, these differences can be attributed to the difference in lift curve slopes seen for each model. Conversely, at the higher advance ratio, the trend is reversed, with the fully turbulent model consistently predicting a lower angle of attack.

Figure 6.5 shows the interpolated boundary layer thickness and displacement thickness along the blade span respectively for $J = 0.24$. Despite the fully turbulent model predicting a higher local angle of attack at $J = 0.24$, the transition model projects a higher distribution of δ across all angles over the suction side. This is mainly due to the transition model estimating δ to be significantly higher at all angles. This difference reduces to a great extent in the displacement thickness curve, except in regions close to the blade tip, where the transition model predicts a higher δ^*. The pressure side boundary layer parameters of δ and δ^* are very similar for both models and don't vary much along the spanwise direction. At the higher advance ratio, the boundary layer thickness tends to vary less along the

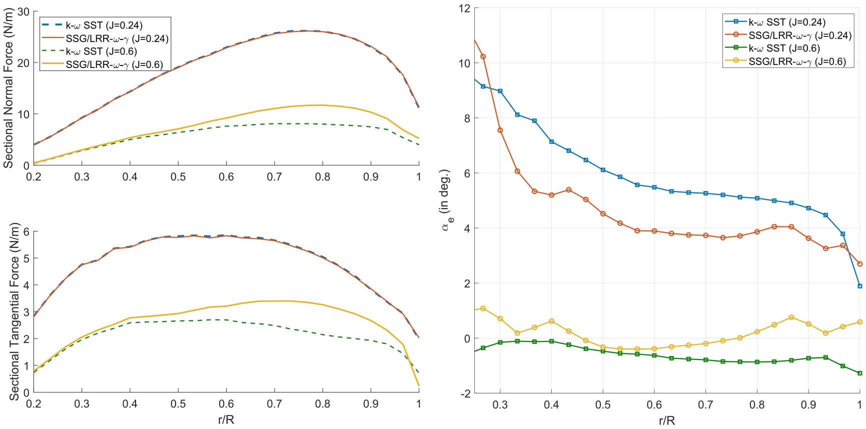

(a) (b)

Figure 6.4: a) Sectional normal and tangential force over the APC rotor blade, b) Effective angle of attack (α_e) based on different loading and operating conditions

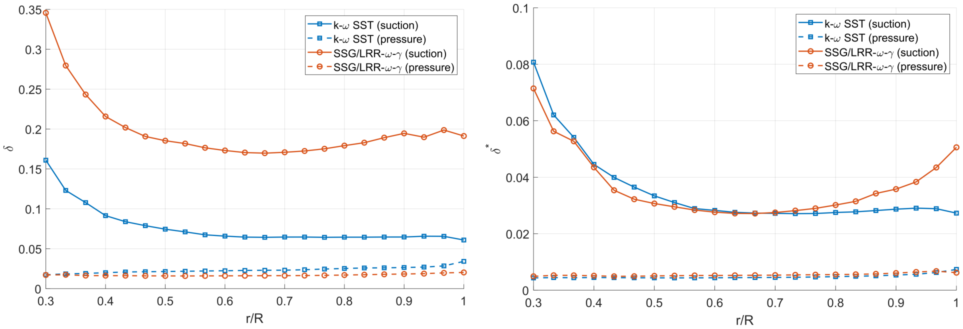

(a) (b)

Figure 6.5: a)Boundary layer thickness (δ) and b) Displacement thickness (δ^*) along the span at $J = 0.24$

span, as a consequence of the distribution of the effective angle of attack. As anticipated, the transition model forecasts a greater boundary layer thickness along the suction side compared to the fully turbulent model. This difference doesn't seem to diminish in the distribution of δ^* either. There is a more discernible difference between the turbulence models in the distribution of δ along the pressure side at this advance ratio. However, this contrast minimizes in the distribution of δ^*, except at the tip.

Finally, the calculated effective angle of attack and displacement thickness distribution, along with sectional Reynolds number and inflow velocity, are used as input parameters for the

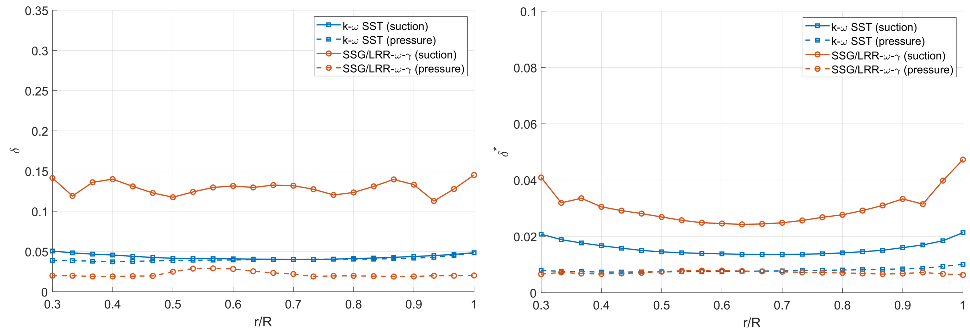

(a) (b)

Figure 6.6: a)Boundary layer thickness (δ) and b) Displacement thickness (δ^*) along the span at $J = 0.6$

BPM code to compute broadband noise. Top image in Figure 6.7 shows the experimental narrowband spectra, compared with the predictions made by the fully turbulent k-ω SST model and the SSG/LRR-ω-γ transition model at $J = 0.24$. The noise predictions were made with respect to Mic 1 from the experimental set-up discussed in [41]. The hump observed around 1.5kHz in the measured spectra is due to motor noise as discussed by Casalino et al. [15]. It's evident that both turbulence models tend to slightly over-predict the spectra, with peaks at different frequencies. While both models show similar predictions in the frequency range of 1000-3000 Hz, the fully turbulent model appears to perform better at higher frequencies compared to the transition model. Upon examining the individual noise components for each model, the most dominant source at lower frequencies and very high frequencies tends to be TBL_{SS}, which is the noise due to the turbulent boundary layer over the suction side. However, the most prominent difference in the model predictions lies in TBL_A, which is attributed to noise generated due to separation or stall. The transition model exhibits a narrower peak for this noise component, tending towards lower frequencies, whereas the fully turbulent model tends towards higher frequencies with a broader peak. Further, the combination of a higher level of TBL_{SS} and TBL_A noise close to the higher frequencies help the fully turbulent model achieve a better prediction in that region.

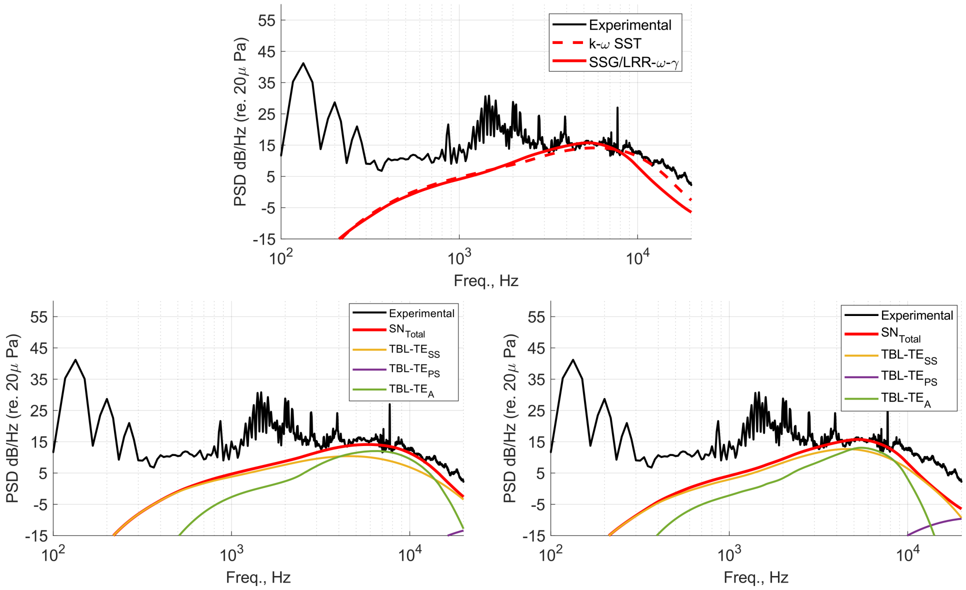

k-ω SST

SSG/LRR-ω-γ

Figure 6.7: Self-noise Noise Prediction at $J = 0.24$. Comparison of total self-noise (top). Individual self-noise components predicted by each turbulence model (bottom)

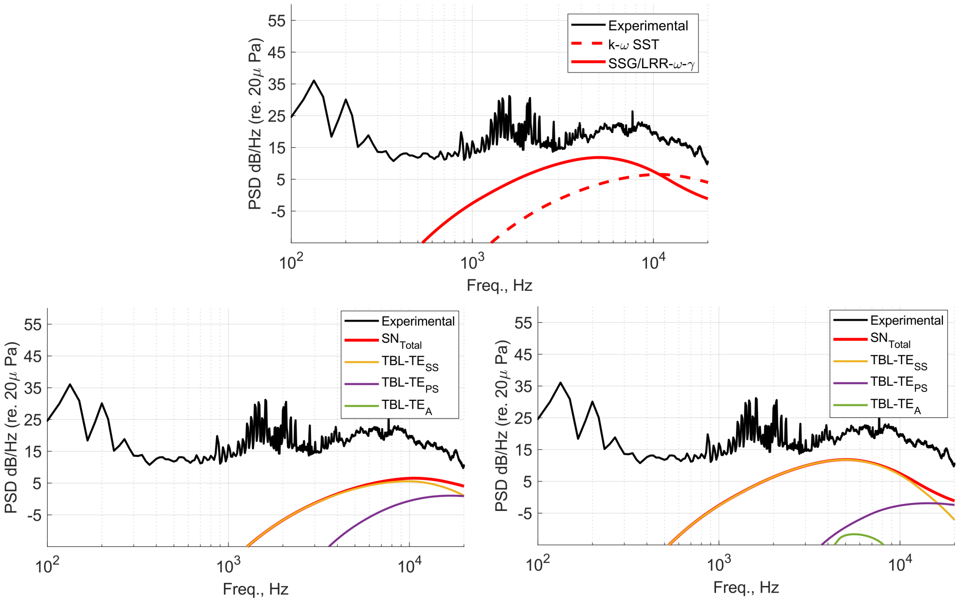

k-ω SST

SSG/LRR-ω-γ

Figure 6.8: Self-noise prediction at $J = 0.6$. Comparison of total self-noise (top). Individual self-noise components predicted by each turbulence model (bottom)

Figure 6.8 presents the broadband noise predictions at the higher advance ratio. Comparing the measured spectra, it can be seen that the broadband hump beyond 2kHz increases in amplitude with an increase in advance ratio. This can be attributed to an increase in the length of the shed vortices as the flow separation moves closer to the trailing edge and tends to remain separated without reattachment. This behavior is evident in the flow visualizations (Figures 5.5(b) and 5.10) and was also discussed in [40]. At this operating condition, both models tend to under-predict the acoustic spectra and the gap in the prediction seems to be larger compared to the previous case. This behavior was also observed in the XFOIL-BEMT based predictions made by Whelchel [120]. The transition model exhibits a notably better prediction than the fully turbulent model, particularly at lower frequencies. The fully turbulent model continues to perform slightly better than the transition model at higher frequencies, although the difference between their performances is smaller compared to the transition model's advantage at lower frequencies for this case. The individual breakdown of the noise components show that the contribution of noise due to the boundary layer on the pressure side has increased in both turbulence models compared to the lower advance ratio, with it dominating at very high frequencies. The main difference again lies in the TBL_A component which seems to be non-existent for the fully turbulent model, while it seems to have an effect in the predictions made by the transition model at lower frequencies.

6.2 Test Case II : T-Motor CF 30x10 Propeller

This section initially discusses the tonal noise predictions and then presents the broadband noise prediction analysis. The test cases analyzed are the same as those considered for the aerodynamic analysis. The acoustic measurements from the experiments carried out by Whelchel et al. [119] have been used to compare the predictions made by the proposed

RANS framework. An advantage of this experimental data is that it contains decomposed components of tonal and broadband noise which were obtained by using a phase averaging technique. This provides a fairer comparison of the predicted broadband noise using the BPM method. The broadband noise predictions are also compared with the predictions made by an XFOIL-BEMT based method propose in [120] to gain insight into the prediction accuracy of methods with different fidelity.

6.2.1 Tonal Noise Prediction

The acoustic spectra predicted by the *libAcoustics* library on OpenFOAM, using the aerodynamic predictions of the SSG/LRR-ω-γ model, are illustrated in Figure 6.9. These plots display the spectra for the hover test case at two distinct microphone locations from the experimental set-up in [119]. Here, Mic 1 is the far-filed mic with directionality of $\theta = 45°$ and Mic 14 is the in-plane mic. The model fairly predicts the Blade Passage Frequency (BPF) tone in both cases. However, tones beyond the BPF are not effectively captured by the current framework. This limitation arises because the harmonics of the BPF are influenced by broadband noise [93, 119], which in turn is highly affected by turbulent flow. RANS simulations only capture the mean turbulent flow and cannot effectively model the fluctuations responsible for generating higher harmonic tones. Consequently, with the current model, only the BPF tone can be accurately captured, while other tones beyond the BPF are not effectively represented.

Figure 6.10 depicts the BPF tone predicted by the two turbulence models for hover and $J = 0.2$. The BPF tone was calculated by taking a 20Hz band centered on the tone for both experimental and computed cases. It is seen that the predictions made by both models are identical. The predictions seem to be the most accurate at the observer angle of $\theta = 15°$.

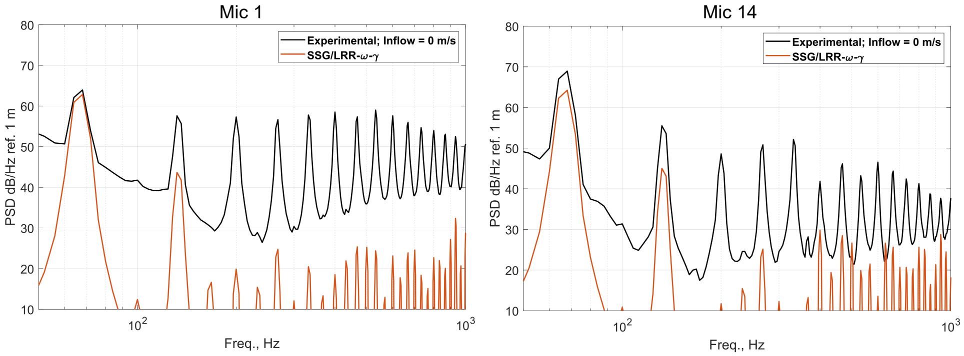

Figure 6.9: Tonal Noise Spectra Predicted by SSG/LRR-ω-γ at hover

The dominant contribution to the BPF tone is generally attributed to thickness noise and steady mean loading. Interestingly, unlike the trends observed in the prediction of global thrust and torque, the accuracy of BPF tone predictions tends to improve with an increase in advance ratio. Additionally, the differences between the turbulence models in predicting aerodynamic load characteristics do not seem to significantly affect the accuracy of BPF predictions. This discrepancy could be attributed to the fact that global characteristics such as thrust, torque, and BPF tend to cancel out various fluctuations, thus providing an incomplete understanding of the underlying detailed mechanisms. Indeed, this underscores the importance of employing comprehensive metrics to evaluate the predictions of different models. By incorporating more holistic metrics that consider a wider range of flow features and characteristics, researchers can gain a deeper understanding of the strengths and limitations of various modeling approaches.

6.2.2 Blade Self-Noise Prediction

2D Aerodynamic Analysis

The T-motor propeller is an off-the-shelf propeller and hence, the exact profile of the spanwise section is unknown. Therefore, in this case, the 2-D RANS simulation is carried out for

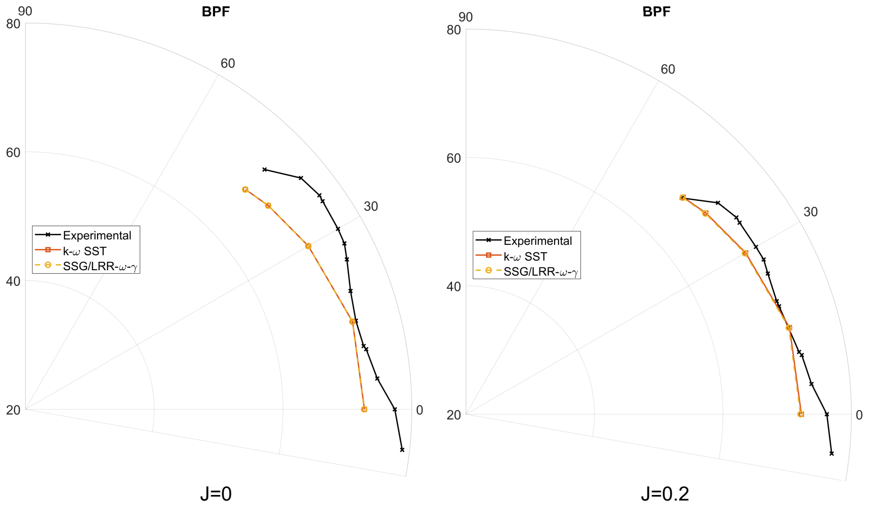

Figure 6.10: Directionality plot of the predicted BPF at different advance ratios

different spanwise sections along the span with its corresponding Reynolds number and local inflow velocity. The lift and drag coefficients of some of the sections have been presented in figure 6.11. As expected, the transition model has a highly varying lift-curve slope, contrasting with the more uniform slope observed in the fully turbulent model. Additionally, mirroring the trends observed previously, the transition model tends to forecast higher lift at higher angles of attack and lower lift at negative angles of attack compared to the fully turbulent model. Similarly, the predictions for drag coefficient align with those from the previous analysis. Further information about the boundary layer and displacement thickness calculations have been omitted for this case to avoid redundancy in the analysis.

3D Loading and Effective Angle of Attack Calculation (α_e)

The loading distribution across the blade surface is depicted in Figure 6.12, showcasing predictions derived from both CFD calculations and the BEMT method. Termed as ”XFOIL-BEMT,” this approach involves acquiring aerodynamic data from XFOIL for individual sections and subsequently analyzing it using BEMT with tip loss corrections to determine local

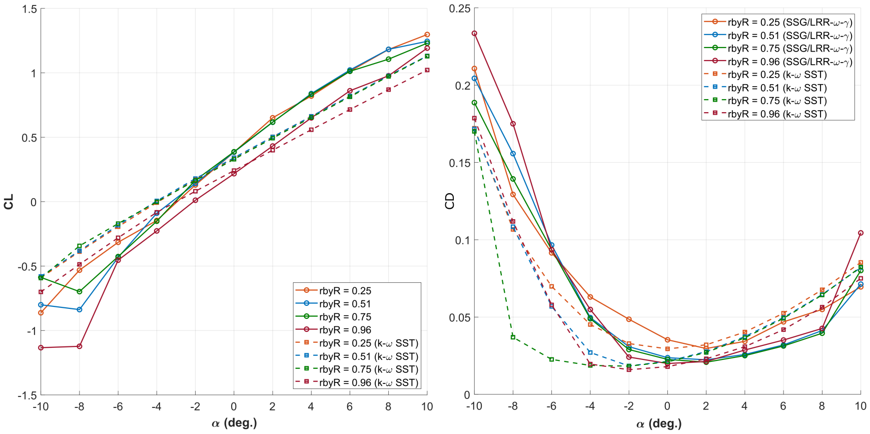

Figure 6.11: Predicted C_L and C_D for different spanwise sections of the T-motor propeller

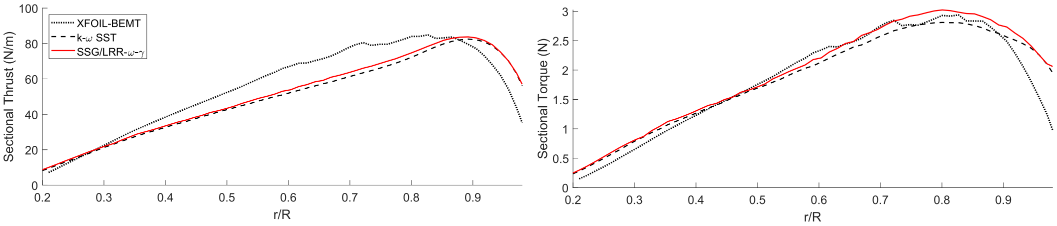

Figure 6.12: Sectional Thrust and Torque distribution over the T-motor propeller blade at hover

angle of attack and loading distribution. The results for the "XFOIL-BEMT" method have been obtained from the analysis conducted in [120].The BEMT-based predictions display a broader loading distribution curve compared to the CFD predictions. This suggests that the low-fidelity method tends to overestimate the integrated thrust due to its less accurate modeling of viscous effects. Further, the thrust distribution peaks around $r/R = 80\%$ for the BEMT-based method, whereas it peaks closer to the tip at $r/R = 85\%$ for the CFD-based method. With respect to torque distribution, differences between the two turbulence models also becomes evident. The k-ω SST model predicts a lower torque distribution curve compared to the transition model, in line with the global torque predictions seen in figure 5.14.

The effective angle of attack predicted by the two turbulence models and the "XFOIL-

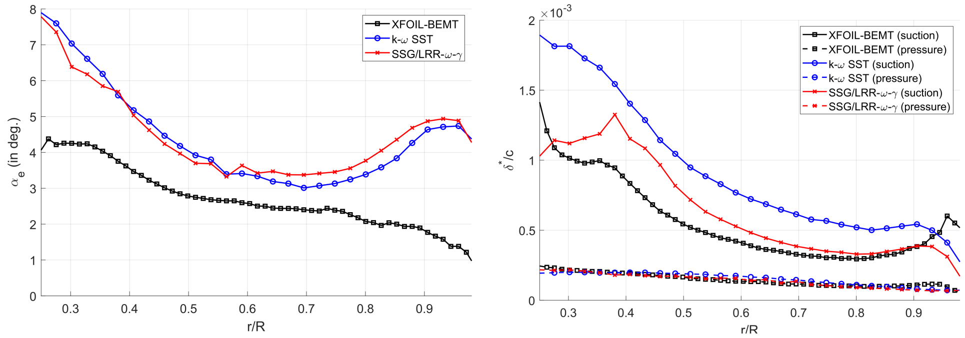

Figure 6.13: Effective angle of attack distribution (left) and δ^* distribution (right) along the span at hover

BEMT" method are presented in figure 6.13. The CFD models tend to predict a higher effective angle of attack all across the blade compared to the BEMT-based method. In the BEMT-based method, the angle of attack consistently decreases across the span. However, in the CFD-based predictions, the angle initially decreases, then increases beyond $r/R = 70\%$, and finally decreases again towards the tip. The corresponding interpolated displacement thickness distribution along the span has been presented on the right side of figure 6.13. There is an evident different between the turbulence models as well as the BEMT-based predictions on the suction side, with the fully turbulent model predicting the highest values of δ^*. For the pressure side, the thickness distribution is fairly similar for all methods and seems to monotonically decrease with the spanwise radius.

In the top-left corner of figure 6.14, the total noise component predicted by each method is displayed. The experimental spectra presented here focus solely on broadband noise, filtering out any high frequency tonal components and motor tones to provide a fairer comparison with the BPM method prediction. The spikes observed at very high frequencies ($> 10^4$Hz) is attributed to ESC noise as well as motor noise that impact the broadband spectra [120]. They are also attributed to the rotor being the same size as the tunnel inlet, thereby creating additional shear effects that could have been captured by the microphones. Both turbulence models produce nearly identical predictions, exhibiting fair accuracy in capturing the high frequency noise. However, the BEMT-based method under-predicts the noise level and exhibits poorer accuracy compared to the CFD-based methods. None of the models successfully capture the lower frequency spectra, typically dominated by blade wake interaction and turbulence ingestion noise, which are not accounted for in the current method.

Further examination of the individual noise components reveals that the CFD-based methods have identical TBL_{SS} components and predominantly similar TBL_A components, with slightly higher levels in the transition model prediction. In the current case, the LBL_{VS} component, representing noise due to laminar boundary layer vortex shedding, has been included in the model. However, it could not be incorporated in the k-ω SST model predictions, as the model only predicts a fully turbulent boundary layer due to its formulation. The inclusion of the $LBL-VS$ component in the transition model seems to offset the lower levels of TBL_{PS}, thereby leading to similar predictions at higher frequencies compared to the fully turbulent model. In the BEMT-based method, transition effects were incorporated through XFOIL, allowing for a direct comparison with the predictions of the CFD-based transition model. Comparing the two, it's observed that the low-fidelity method predicts lower levels of TBL_{SS} and TBL_A components, but significantly higher TBL_{PS} and $LBL-VS$ components compared to the transition model prediction. Overall, the reduced accuracy in the low-fidelity method can be attributed to the underlying aerodynamic predictions. It is highly likely that the XFOIL predictions of sectional polars are lacking due to complex transition phenomena seen at these operating conditions. Consequently, these inaccuracies could have influenced the calculation of induced and effective angles of attack, as well as boundary layer properties, which were subsequently utilized in the BPM code.

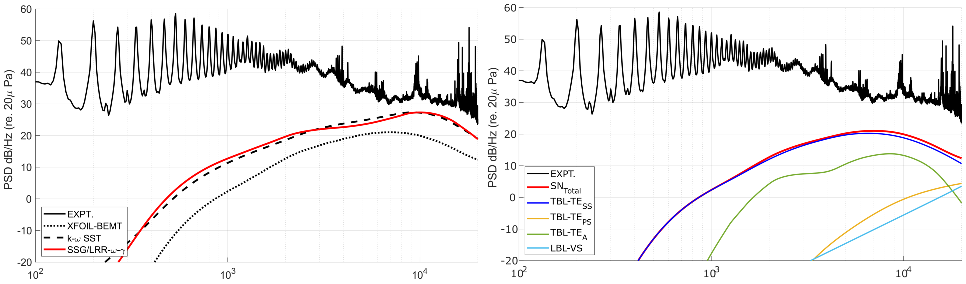

Total Noise Comparison

XFOIL-BEMT

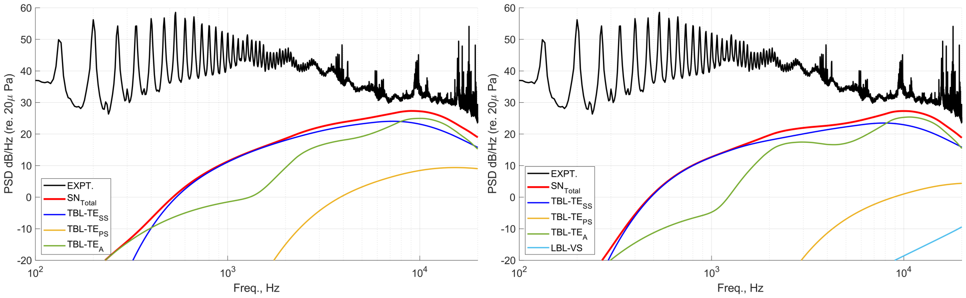

k-ω SST

SSG/LRR-ω-γ

Figure 6.14: Total Blade self-noise prediction and individual breakdown of self-noise components for each computational method

6.2.3 Conclusions

An assessment of aeroacoustic prediction methods for the two propeller test cases was carried out. Tonal noise prediction was carried out using the acoustic analogy and it was seen that the BPF tone was well captured by the current framework. The higher harmonics were not predicted well since these tones are influenced by turbulent fluctuations, which are not captured by RANS models. The major focus of this chapter was on modeling blade self-noise using a CFD-based BPM framework. Using the first propeller, effects of changing operating conditions on model predictions was studied. The fully turbulent model prediction deteriorated more noticeably with an increase in advance ratio compared to the transition model. When comparing CFD-based predictions with a lower fidelity method, it became evident that the CFD-based methods provided better predictions of the broadband spectrum.

Chapter 7

Design and Analysis of Swept Propellers for Large Payload Multi-copters

This chapter introduces a design study that was carried out using the established flow and nosie prediction methods. The advantages and disadvantages of a swept rotor for low-*Re* applications were investigated. The CFD analysis portion of the following write-up was published in [91].

Tackling the issue of noise mitigation in rotors requires innovative design ideas while ensuring that their aerodynamic efficiency is not compromised. The current study aims to explore one such design: swept rotors. Similar to swept wings, swept rotors are known to improve the aerodynamic efficiency in compressible flow regimes. In marine propulsion, swept rotors are widely used as they are known to reduce the noise and vibration when subjected to large non-uniform inflow that arises from the wake of the ship hull [14]. From an acoustic perspective, Hanson [44] showed that swept planforms can be beneficial in mitigating noise for conventional propeller-driven aircraft. He demonstrated that destructive interference of individual components of noise emitted by blade sections along the span can lead to reduced total noise. Wright and Simmons demonstrated a considerable noise reduction in swept-bladed axial fans in comparison to the straight-bladed design when subjected to highly turbulent inflow [126]. Similar analyses for lower Reynolds number regimes, where UAVs are known to operate, seem to be limited. Recently, Weidemann et al [121] conducted a parametric analysis of different swept blade geometries and concluded that the aerodynamic performance for sUAV rotors seem less sensitive to sweep while the noise does seem to reduce in comparison to the unswept blade, albeit subject to the sweep angle. However, the study focused mainly on low frequency tonal noise sources.

The work discussed in the current chapter aims to conduct an in-depth study of the aerodynamic and aeroacoustic characteristics of swept rotors compared to straight-bladed (or unswept) rotors. For this, an experimental analysis was performed in the Virginia Tech Open Jet tunnel where the loading and acoustic characteristics of the rotor were measured at varying rotational speeds and inflow conditions. The results and analysis of this experiment are presented in [91, 120]. Using the methods presented in [119], the measured acoustic spectra were separated into broadband and tonal components to understand the influence of each component on the rotor noise and how it changes with varying operating conditions. The computational analysis was validated using this data. The computational framework uses the proposed transition turbulence model, SSG/LRR-ω-γ, which has been validated for isolated rotors in previous chapters. A brief acoustic analysis to study the self-noise components of each blade is also presented.

7.1 Computational Set-up

7.1.1 Propeller Geometry

Unswept and swept propeller geometries are compared in the current study. The unswept geometry shown in Figure 7.1 (a), abbreviated as UG for the remaining paper, is the commercially available T-motor carbon-fiber propeller that has a 30 in. (0.762 m) diameter and 10.5 in. pitch. The swept propeller geometry (abbreviated as SG) shown in figure 7.1 (b) is designed to have the same diameter in order to maintain dynamic similarity. The blade sections are designed using the NACA-16 series ($a = 0.8$) airfoil. It is to be noted that the swept geometry is not shape optimized any way and is just a proof-of-concept to study the effect of sweep. The chord and pitch distribution for each of the rotors are given in Figure 7.1 (c) and (d). The net sweep provided to the propeller is roughly equal to 20^0.

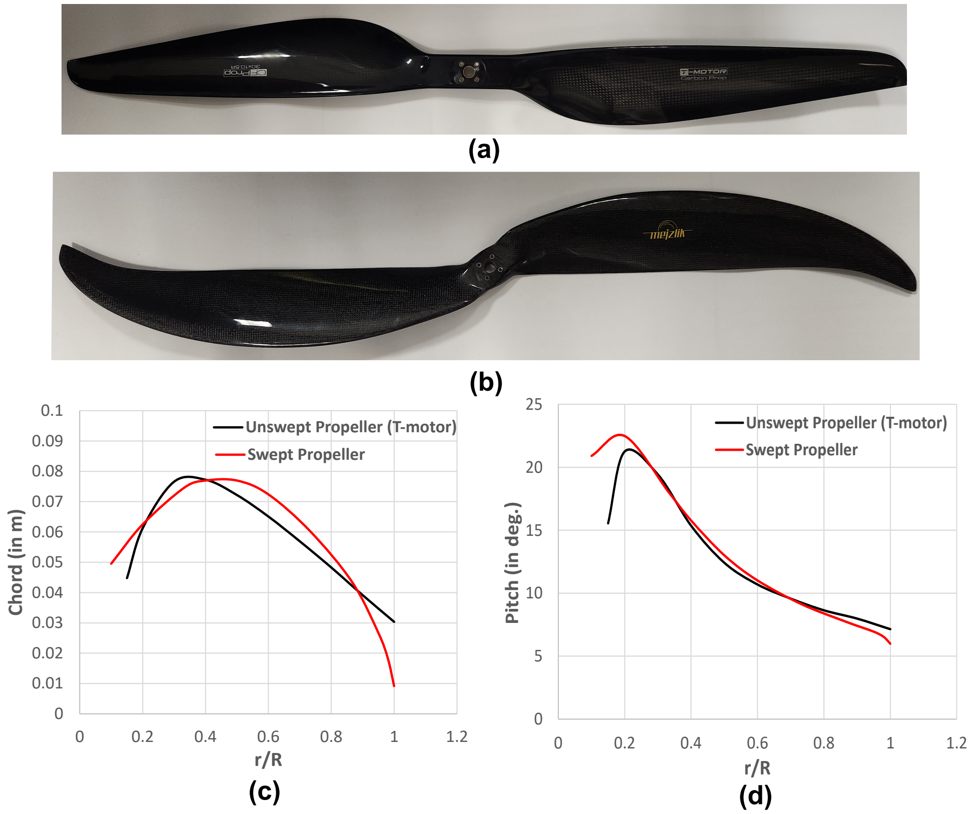

Figure 7.1: (a) Unswept T-motor propeller (b) Swept propeller (c) Chord Distribution (d) Pitch Distribution

7.1.2 Grid-Independence Analysis

CFD simulations in the current study were performed on OpenFOAM-v2006. An overset grid was implemented using *snappyHexMesh*, which is a split-hexahedra meshing utility on OpenFOAM. The background (stationary) mesh was constructed to extend up to a distance of $6R$ in the plane of rotation, $4R$ upstream of the rotor and $10R$ in the wake of the rotor, where R indicates the propeller radius. The region in the wake was set to be large in order to avoid any re-circulation effects. The background grid has 5 refinement levels with the finest region having the same grid size as the overset region. A simple grid-independence study was carried out on the swept propeller to set the resolution of the surface grid and the prism layers for the overset region of the mesh. The background grid resolution was kept unchanged in the grid independence study. Table 7.1 shows the different resolutions tested. The two values specified under surface resolution indicate the maximum and minimum spacing on the rotor surface scaled by the tip chord (c). Figure 7.2 shows the change in coefficient of thrust and torque with increase in grid resolution. The solution for CQ becomes independent of the grid by the 3^{rd} mesh. The 3^{rd} and 4^{th} grids have the same $y^+(1)$. This implies that torque is more sensitive to the $y^+(1)$ resolution while thrust is more sensitive towards surface resolution for the current computational framework. For the remaining analysis, grid 3 was chosen. The same grid parameters were used for the unswept rotor as well.

Table 7.1: Grid Resolution Matrix for the Swept Propeller

	Surface Resolution	$y^+(1)$
Grid 1	[$0.05c$, $0.025c$]	1.5
Grid 2	[$0.025c$, $0.0125c$]	1.2
Grid 3	[$0.025c$, $0.00625c$]	0.9
Grid 4	[$0.0125c$, $0.00625c$]	0.9

The computational analysis was performed for a select number of test cases from the experimental data. Operating conditions of the cases considered in the CFD study along with the

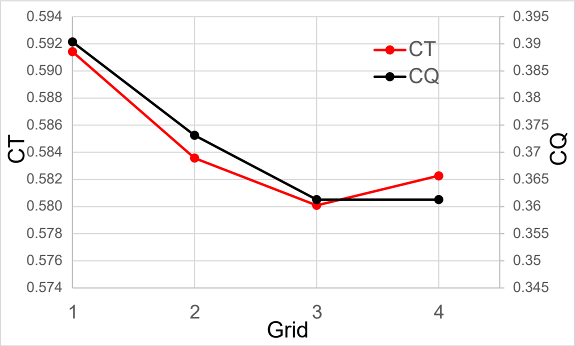

Figure 7.2: Grid Independence Study carried out on the swept propeller.

Reynolds number at 75% spanwise section have been given in Table 7.2

Table 7.2: Test Matrix of CFD Simulations for both propeller geometries

RPM	U_∞ **(m/s)**	**J**	**UG:**Re_{75}	**SG:**Re_{75}
1830	0	0	1.92×10^5	2.26×10^5
1830	5	0.22	1.93×10^5	2.27×10^5
2000	0	0	2.10×10^5	2.47×10^5
2000	5	0.19	2.11×10^5	2.48×10^5

7.2 Computational Results and Analysis

7.2.1 Aerodynamic Analysis

For the CFD analysis, firstly the predicted thrust and torque coefficients were estimated. The aerodynamic coefficients were calculated by taking the mean of the axial force and moment across the final rotor revolution and non-dimensionalizing them by applying equation (**??**).

Tables 7.3 and 7.4 show the comparison between the predicted and measured performance coefficients for the unwept and swept propellers respectively. Further, figure 7.3 shows a bar plot indicating the prediction error for each test case. The model performs best at hover conditions. The accuracy reduces as the advance ratio increases but stays within 12% for

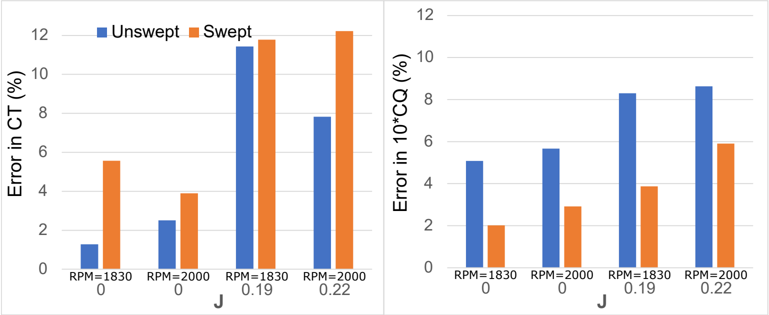

Figure 7.3: Bar plot showing the error in predictions of CT and CQ for the two propeller geometries

thrust and within 10% for torque.

The steady loading distribution over a single blade is shown in Figures 7.4 and 7.5 for the case with $U_\infty = 5$ m/s and $U_\infty = 0$ m/s respectively. Here, "UG" stands for the unswept geometry and "SG" stands for swept geometry. The surface loading was calculated by taking the mean of the integrated chordwise pressure over the last rotor revolution. For the case with a finite inflow, the swept propeller has a higher predicted sectional thrust and torque at both RPMs, while, the unswept propellers seems to have a higher torque at the sections closer to the hub and tip. The location of peak loading for each of the cases have been indicated with a dotted line of the same color. he differences in the thrust plot are not significant, however, in the sectional moment plot, the swept rotor peaks at in-board location compared to the unswept geometry. At hover, the thrust distribution again suggests that both propellers have

Table 7.3: Comparison of experimental and predicted thrust and torque coefficients for the Unswept Rotor

RPM	U_∞	**J**	CT_{exp}	CT_{pred}	CQ_{exp}	CQ_{pred}
1830	0	0	0.076	0.074	0.0038	0.0036
2000	0	0	0.077	0.075	0.0038	0.0036
2000	5	0.19	0.062	0.055	0.0038	0.0035
1830	5	0.22	0.056	0.052	0.0037	0.0034

Table 7.4: Comparison of experimental and predicted thrust and torque coefficients for the Swept Rotor

RPM	U_∞	**J**	CT_{exp}	CT_{pred}	CQ_{exp}	CQ_{pred}
1830	0	0	0.074	0.079	0.0039	0.0039
2000	0	0	0.075	0.078	0.0039	0.0038
2000	5	0.19	0.066	0.058	0.0038	0.0037
1830	5	0.22	0.062	0.054	0.0038	0.0036

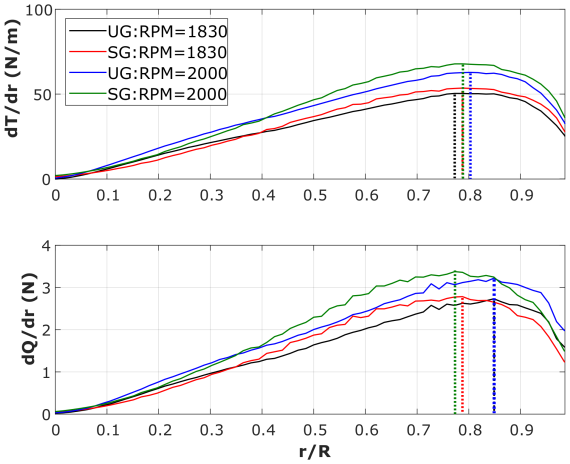

Figure 7.4: Predicted sectional thrust and torque of a single blade vs normalized span at $U_\infty = 5$ m/s

the peak loading at similar spanwise locations which has shifted closer to the tip compared to the case with a finite inflow. However, the order of the peak moment distribution is switched, wherein the unswept rotor has a more in-board location compared to the swept geometry.

Figures 7.6 and 7.7 show the contour of skin friction coefficient (C_f) along with streamlines at varying RPMs for the two propellers. The regions where the streamlines converge are indicative of separation or low skin friction coefficient zones. The contours for the unswept propeller show that at RPM=2000, there is a larger region of low skin friction (indicated by the light blue region) which extends along the rotor span compared to the case with

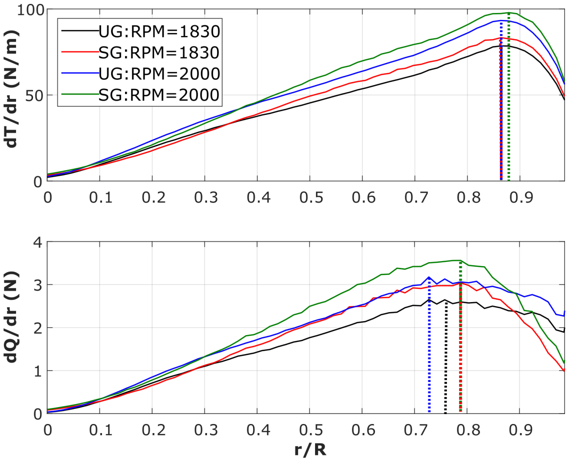

Figure 7.5: Predicted sectional thrust and torque of a single blade vs normalized span at $U_\infty = 0$ m/s

RPM=1830. There is very little difference seen on the suction side for the swept propeller with a change in RPM. This does not seem in agreement with the thrust and torque plots seen in the previous section which suggested that the swept rotor is more sensitive to change in Reynolds number. The main difference between the two propellers is visible closer to the tip, wherein the swept propeller has the separated region (converged streamlines) extend all the way up to the tip. The separation and reattachment of flow happens upstream of the chord for the swept propeller in comparison to the unswept geometry closer to the tip. Further, at each RPM, the unswept rotor has lower levels of skin friction close to the leading edge of the blade compared to the swept rotor. At the pressure side in Figure 7.7, both propellers show very similar behavior at both RPMs. From the streamlines, it looks like the flow tends to separate and reattach close to the leading edge for a large portion of the span. The swept propeller, however, has a much larger region of attached flow close to the tip.

At hover, the separation zone does not extend until the tip as shown in Figure 7.8. This behavior is also observed in the experiment conducted by Grande et al. [40]. They explain that the tip vortex washes out the possible separation and transition zones when the inflow is zero. Compared to the case with a finite inflow, the separation region at hover moves upstream along the chordwise direction. This is due to the fact that at zero advance ratio, the angle of attack at individual sections is higher compared to the case with a finite advance ratio, resulting in an earlier flow separation and transition.

Figure 7.10 shows the Q-criterion plot at all the test cases considered. At hover, for both RPMs, it can be seen that the wake tends to push the wake flow upstream and cause recirculation while, at a finite inflow, the wake is washed down with no recirculation. This further supports the fact that at hover, the mid-frequency range which is governed by blade wake interaction and turbulence ingestion noise, is much higher (as discussed in the previous section). The swept rotor is seen to have a larger diffusion of vortex structures, causing a dense collection of weaker vortices at the core. Figure 7.11 shows the vorticity contour along the axial plane. The hub vortex for the unswept rotor is stronger compared to the swept geometry. For the swept rotor, it is seen that the vorticity is spread more widely and the trailing vortex has a wider curvature, thereby a wider surface area. It is possible that this results in a lower blade wake interaction, supporting the observations made in previous section.

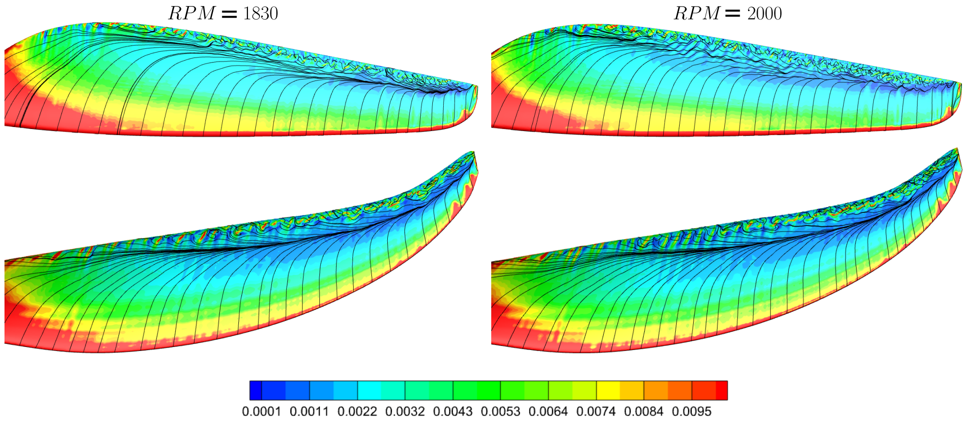

Figure 7.6: C_f contour with streamlines along the suction side at $U_\infty = 5$ m/s. The blade is at $\phi = 0^o$ at the 15^{th} revolution

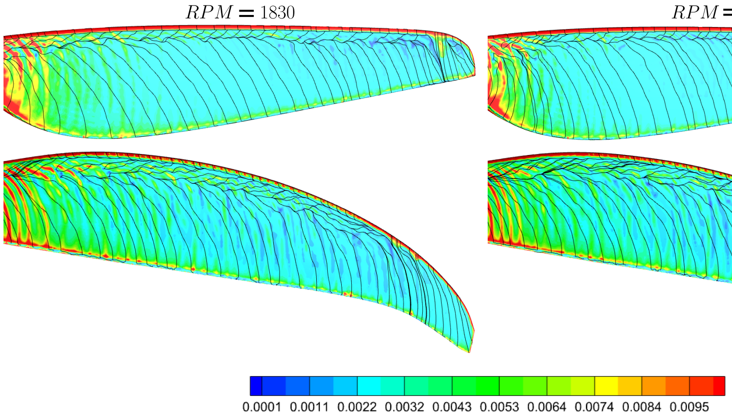

Figure 7.7: C_f contour with streamlines along the pressure side at $U_\infty = 5$ m/s. The blade is at $\phi = 0^o$ at the 15^{th} revolution

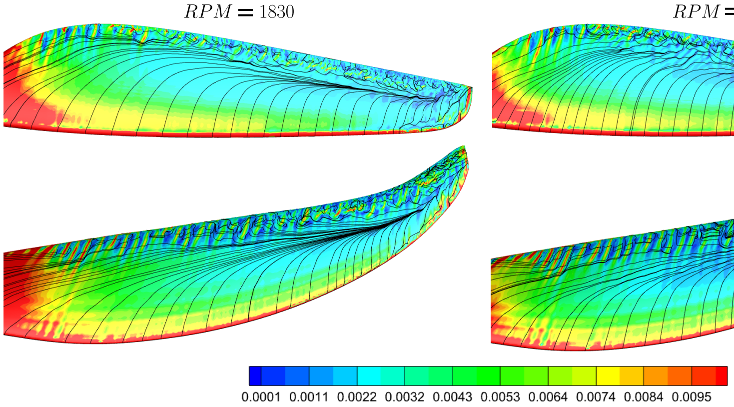

Figure 7.8: C_f contour with streamlines along the suction side at $U_\infty = 0$ m/s. The blade is at $\phi = 0^o$ at the 15^{th} revolution

At RPM=2000, two spanwise sections at $r/R = 75\%$ and $r/R = 90\%$ were studied closely to understand the behavior at the boundary layer for both the propellers as shown in Figures 7.12 and 7.13 respectively. The turbulent kinetic energy (TKE) is presented to show the onset of transition. The point where the TKE contour starts to increase is indicative of transition to turbulent flow and is annotated with a red arrow in all the images. As the inflow increases, the transition location moves downstream due to the decrease in angle of attack. This is more evident for the swept propeller at $r/R = 75\%$ in Figure 7.12 and

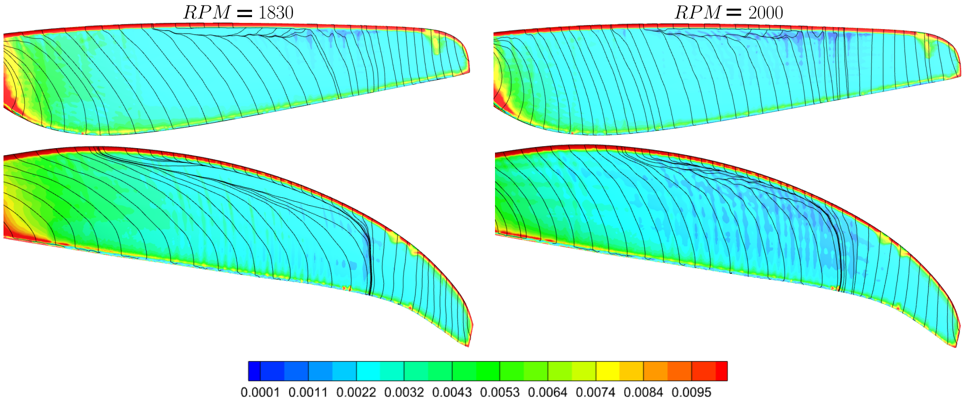

Figure 7.9: C_f contour with streamlines along the pressure side at $U_\infty = 0$ m/s. The blade is at $\phi = 0^o$ at the 15^{th} revolution

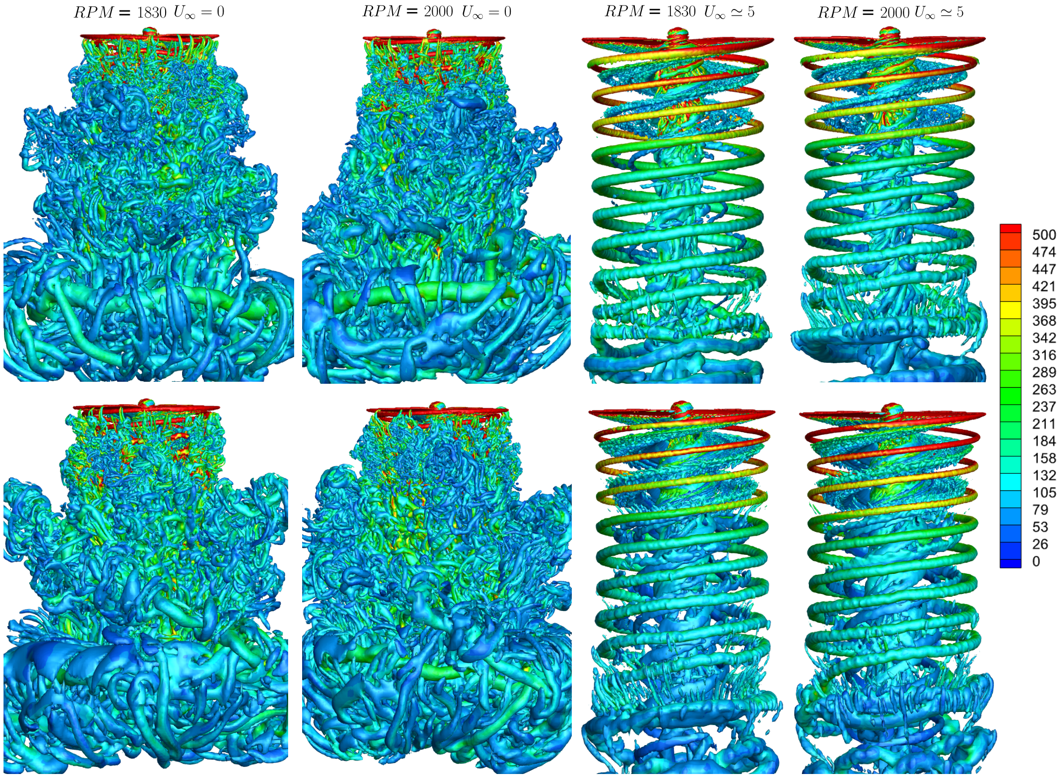

Figure 7.10: Q-criterion plot colored with vorticity magnitude at the 15^{th} revolution for the unswept propeller (top) and the swept propeller (bottom)

clearly distinct for both propellers at $r/R = 90\%$ in Figure 7.13. This behavior was also demonstrated in the experiments carried out by Grande et al. [40].

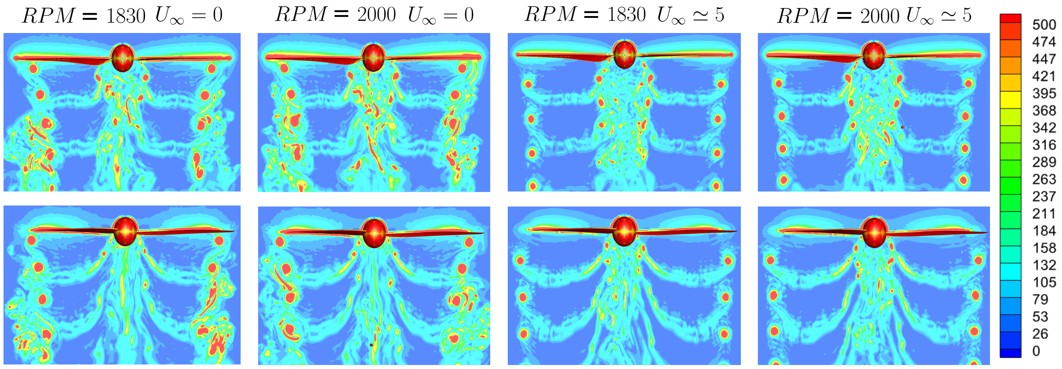

Figure 7.11: Vorticity magnitude contours along the plane $y = 0$ for the unswept propeller (top) and the swept propeller (bottom)

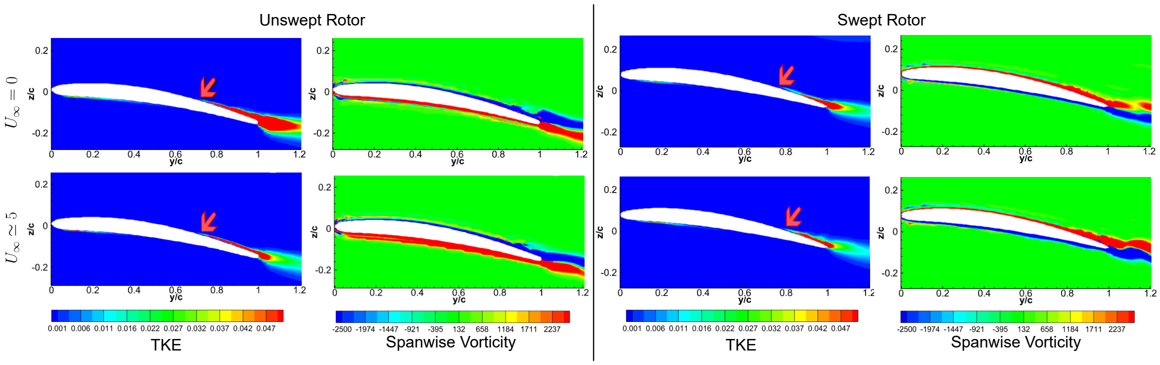

Figure 7.12: Turbulent kinetic energy (TKE) and spanwise vorticity contour at $r/R = 75\%$ for RPM=2000

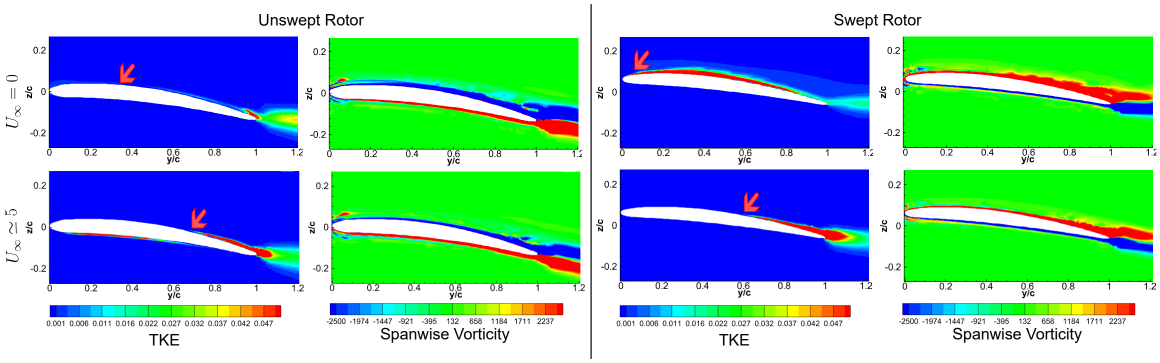

Figure 7.13: Turbulent kinetic energy (TKE) and spanwise vorticity contour at $r/R = 90\%$ for RPM=2000

7.2.2 Aeroacoustic Analysis

The acoustic signatures of the swept and the unswept propellers were measured in the Virginia Tech Open Jet wind tunnel and the results are presented in Pisharoti et al. [91]. The findings from Pisharoti et al. [91] show that swept propellers provide an acoustic advantage, specially when it comes to broadband noise. Sweeping the propeller blades have been shown reduce mid-frequency tones, which are often associated with turbulence ingestion noise and blade wake interaction components. Additionally, the authors also observed a reduction in high-frequency noise during hover, typically attributed to self-noise, further highlighting the benefits of employing swept propellers. By leveraging the proposed self-noise prediction method, the current study seeks to delve a little deeper into the individual components contributing to broadband noise to enable a more comprehensive understanding of the underlying mechanisms influencing noise generation. The hover condition at an $RPM = 2000$ has been considered for this study. The three-dimensional loading data for both the propellers has been taken from the OpenFOAM simulations to maintain consistency with the rest of the analysis.

Figure 7.14 shows the comparison of the measured narrowband spectra with the CFD-based predictions. The predictions made for the unswept propeller, utilizing three-dimensional data from the OpenFOAM predictions in this chapter, are consistent with those from the previous chapter, which employed the Pointwise mesh for its three-dimensional analysis. In terms of the swept propeller, it seems like the CFD-based predictions tends to marginally over-predict the measured high-frequency noise. Due to this discrepancy, conducting a comparative analysis of the individual components of noise sources generated by each propeller might not be entirely fair. Nonetheless, observations on which component of noise seems to dominate each propeller can still be carried out.

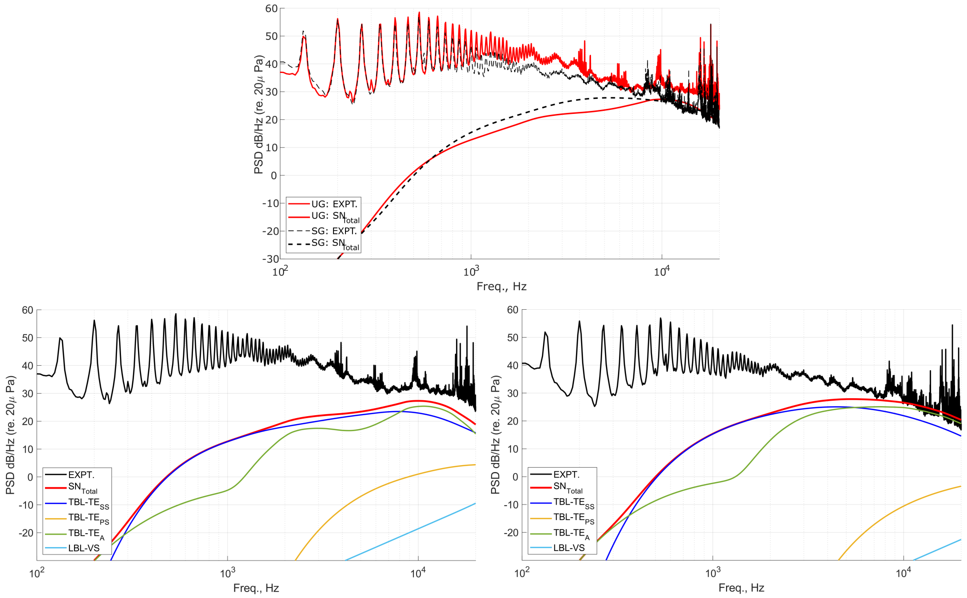

Unswept

Swept

Figure 7.14: Self-noise prediction at $RPM = 2000$ and $U_\infty = 0$. Comparison of total self-noise (top). Individual self-noise components generated by different propellers (bottom)

The suction side turbulent boundary layer noise is dominant for both propellers at lower frequencies and continues to stay dominant for the unswept propeller until roughly 8000Hz. For the swept propeller however, the turbulence separation and stall noise TBL_A tends to take-over much earlier at roughly 4000Hz and stays dominant even at very high frequencies. The TBL_{PS} and $LBL - VS$ noise components tend to contribute to the total spectrum from low frequencies and peak at very high frequencies, indicating a higher prevalence of laminar separation and vortex shedding in the unswept propeller, which spans over a broader frequency range.

7.3 Conclusions

A detailed study was carried out to understand the influence of sweep on the aerodynamic and aeroacoustic performance of a UAV propeller. This analysis was performed to complement the experimental analysis presented in [91, 120]. A qualitative analysis of the wake indicated that the swept rotor exhibits lower blade wake interaction, further supporting the experimental observations. The boundary layer characteristics at two different sections were also analyzed and it was concluded that the difference in the high frequency noise observed could be due to the differences in transition and separation phenomena observed on the rotor surface. Blade self-noise predictions indicated that the contribution of noise from the turbulent boundary layer on the pressure side and the laminar boundary layer were higher for the unswept propeller compared to the swept variant. However, further investigation is warranted to conclusively confirm these findings, as the noise predictions require additional refinement.

Chapter 8

Summary

The primary goal of the current study was to establish a computational framework that would accurately capture the complex flow encountered in low-*Re* propeller flows. To achieve that, a second-order RANS closure transition turbulence model, SSG/LRR-ω-γ was proposed. The model formulation was implemented on OpenFOAM. It has proven to be capable of capturing different transition mechanisms with equivalent or better accuracy compared to the current state-of-the-art for different canonical cases. The current study also demonstrated the ability of RST models to be better than linear eddy viscosity models when it comes to highly three dimensional flows. After thorough validation of the proposed model, it was applied on multiple low-*Re* propellers. The comparative analysis involving different turbulence models revealed two key findings. Firstly, transition models in general exhibited greater robustness in their prediction capabilities and in capturing underlying physics. Secondly, among the transition models, the newly proposed SSG/LRR-ω-γ model appeared to have an advantage in predicting detailed flow features. Furthermore, to obtain a fast prediction of broadband noise, a RANS-coupled semi-empirical self-noise prediction method was implemented. An assessment of different models showed the proposed transition model to be very consistent in its predictions with varying geometry as well as operating conditions. Finally, the combined flow and noise prediction framework was applied to a novel swept propeller design to understand its influence on aerodynamic and acoustic characteristics.

Future Scope

This thesis has attempted to address some of the shortcomings and challenges in the fields of turbulence modeling in the context of canonical cases as well as low-*Re* propeller applications. It has also looked into the aeroacoustic modeling for these low-*Re* rotors using the current state-of-art. The author would like to propose some improvements for each of these facets:

- The proposed model needs to be validated across a broader range of applications to establish its reliability. Further, extending the model to incorporate roughness effects would improve its applicability to real-world scenarios to a greater extent. The crossflow extension of the model can be improved by making it Galilean invariant.

- For low-*Re* propellers, it would be interesting to study crossflow transition effects using the established transition model. It would also be interesting to study rotor-rotor and rotor-airframe interactional effects using transition models to further understand the underlying flow physics.

- Extending the current RANS model to a hybrid RANS/LES framework would also be a promising direction. This would provide accurate estimation of near-wall phenomena using the underlying RANS transition model, as well as a good representation of far-field flow characteristics. This framework could also improve aeroacoustic predictions.

- Finally, a crucial point regarding the current self-noise prediction method needs to be addressed. The method notably simplifies the prediction of broadband noise, primarily considering it as a function of 2D boundary layer properties. Aerodynamic models now are capable of capturing complex flow phenomena that are known to influence high frequency noise. However, the BPM model does not take these effects into consideration. A more comprehensive parametric study is required to develop updated scaling parameters that encompass these intricate influences within broadband noise prediction frameworks to improve their prediction.

Bibliography

[1] Turbulence modeling resource. https://turbmodels.larc.nasa.gov/. Accessed: 2023-03-08.

[2] *Turbulence Modeling for CFD.* DCW Industries, Inc., La Canada, CA, 1993.

[3] *Turbulent Flows*, pages 364–365. Cambridge University Press, Cornell Universty, NY, 2000.

[4] Samuel O Afari. Prediction of noise associated with an isolated uav propeller. 2019.

[5] Michael F Barad, Joseph G Kocheemoolayil, and Cetin C Kiris. Lattice boltzmann and navier-stokes cartesian cfd approaches for airframe noise predictions. In *23rd AIAA Computational fluid dynamics conference*, page 4404, 2017.

[6] William G Bastedo Jr and Thomas J Mueller. Spanwise variation of laminar separation bubbles on wings at low reynolds number. *Journal of aircraft*, 23(9):687–694, 1986.

[7] John Brandt and Michael Selig. Propeller performance data at low reynolds numbers. In *49th AIAA Aerospace Sciences Meeting including the New Horizons Forum and Aerospace Exposition*, page 1255, 2011.

[8] Kenneth S Brentner and Feridoun Farassat. Modeling aerodynamically generated sound of helicopter rotors. *Progress in aerospace sciences*, 39(2-3):83–120, 2003.

[9] Thomas F Brooks, Michael A Marcolini, and D Stuart Pope. Main rotor broadband noise study in the dnw. *Journal of the American Helicopter Society*, 34(2):3–12, 1989.

[10] Thomas F Brooks, D Stuart Pope, and Michael A Marcolini. Airfoil self-noise and prediction. Technical report, 1989.

[11] Casey L Burley and Thomas F Brooks. Rotor broadband noise prediction with comparison to model data. *Journal of the American Helicopter Society*, 49(1):28–42, 2004.

[12] Samet Caka Cakmakcioglu, Onur Bas, and Unver Kaynak. A correlation-based algebraic transition model. *Proceedings of the Institution of Mechanical Engineers, Part C: Journal of Mechanical Engineering Science*, 232(21):3915–3929, 2018.

[13] Samet Caka Cakmakcioglu, Onur Bas, Riccardo Mura, and Unver Kaynak. A revised one-equation transitional model for external aerodynamics. *Applied CFD Modeling and Numerical Corrections with Experimental Data I*, June, 2020.

[14] John Carlton. *Marine propellers and propulsion*. Butterworth-Heinemann, 2018.

[15] Damiano Casalino, Edoardo Grande, Gianluca Romani, Daniele Ragni, and Francesco Avallone. Definition of a benchmark for low reynolds number propeller aeroacoustics. *Aerospace Science and Technology*, 113:106707, 2021.

[16] Damiano Casalino, Gianluca Romani, Raoyang Zhang, and Hudong Chen. Lattice-boltzmann calculations of rotor aeroacoustics in transitional boundary layer regime. *Aerospace Science and Technology*, 130:107953, 2022.

[17] Kuei-Yuan Chien. Predictions of channel and boundary-layer flows with a low-reynolds-number turbulence model. *AIAA journal*, 20(1):33–38, 1982.

[18] Jae Hoon Choi and Oh Joon Kwon. Enhancement of a correlation-based transition turbulence model for simulating crossflow instability. *AIAA Journal*, 53(10):3063–3072, 2015.

[19] Andrew W Christian and Randolph Cabell. Initial investigation into the psychoacoustic properties of small unmanned aerial system noise. In *23rd AIAA/CEAS aeroacoustics conference*, page 4051, 2017.

[20] Julien Cliquet, Robert Houdeville, and Daniel Arnal. Application of laminar-turbulent transition criteria in navier-stokes computations. *AIAA journal*, 46(5):1182–1190, 2008.

[21] Jason Cornelius, Sven Schmitz, Jose Palacios, Bernadine Juliano, and Richard Heisler. Rotor performance predictions for urban air mobility: Single vs. coaxial rigid rotors. *Aerospace*, 11(3):244, 2024.

[22] Miranda Costenoble, James Baeder, John Hrynuk, and Rajneesh Singh. Computation and extraction of boundary layer parameters from numerical simulations for use in rotor acoustics models. In *VFS 76th Annual Forum & Technology Display*, 2020.

[23] J Coupland. Ercoftac special interest group on laminar to turbulent transition and retransition: T3a and t3b test cases. *A309514*, 1990.

[24] JR Dagenhart and William S Saric. Crossflow stability and transition experiments in swept-wing flow. Technical report, 1999.

[25] Bart J. Daly and Francis H. Harlow. Transport equations in turbulence. *The Physics of Fluids*, 13(11):2634–2649, 1970.

[26] M. Drela. Viscous-inviscid analysis of transonic and low reynolds number airfoils. *AiAA Journal*, 25(10):1347–1355, 1989.

[27] M. Drela. Xfoil: An analysis and design system for low reynolds number airfoils. *Technical Report, MIT*, 1989.

[28] M. Drela. Three-dimensional integral boundary layer formulation for general configurations. *21st AIAA Computational Fluid Dynamics Conference*, 2013.

[29] Bernhard Eisfeld and Olaf Brodersen. Advanced turbulence modelling and stress analysis for the dlr-f6 configuration. In *23rd AIAA Applied Aerodynamics Conference*, page 4727, 2005.

[30] Bernhard Eisfeld, Chris Rumsey, and Vamshi Togiti. Verification and validation of a second-moment-closure model. *AIAA Journal*, 54(5):1524–1541, 2016.

[31] Andrey Epikhin, Ilya Evdokimov, Matvey Kraposhin, Michael Kalugin, and Sergei Strijhak. Development of a dynamic library for computational aeroacoustics applications using the openfoam open source package. *Procedia Computer Science*, 66: 150–157, 2015.

[32] Fereidoun Farassat. Derivation of formulations 1 and 1a of farassat. Technical report, 2007.

[33] Fereidoun Farassat and Jay Casper. Towards an airframe noise prediction methodology: Survey of current approaches. In *44th AIAA Aerospace Sciences Meeting and Exhibit*, page 210, 2006.

[34] Jochen Fröhlich and Dominic Von Terzi. Hybrid les/rans methods for the simulation of turbulent flows. *Progress in Aerospace Sciences*, 44(5):349–377, 2008.

[35] Ryan Gerakopulos, Michael S.H. Boutilier, and Serhiy Yarusevych. Aerodynamic characterization of a naca 0018 airfoil at low reynolds numbers. *40th AIAA Fluid Dynamics Conference*, pages 1–13, 2010.

[36] Stewart Glegg and William Devenport. *Aeroacoustics of low Mach number flows: fundamentals, analysis, and measurement*. Academic Press, 2017.

[37] James Goldschmidt, Henry Tingle, Peter G Ifgu, Steven A Miller, Lawrence S Ukeiley, Ben Goldman, Giovanni Droandi, and Kyuho Lee. Acoustics and forces from an isolated rotor system. In *AIAA SCITECH 2022 Forum*, page 2530, 2022.

[38] Cornelia Grabe and Andreas Krumbein. Correlation-based transition transport modeling for three-dimensional aerodynamic configurations. *Journal of Aircraft*, 50(5): 1533–1539, 2013.

[39] Cornelia Grabe, Nie Shengyang, and Andreas Krumbein. Transition transport modeling for the prediction of crossflow transition. In *34th AIAA applied aerodynamics conference*, page 3572, 2016.

[40] Edoardo Grande, Daniele Ragni, Francesco Avallone, and Damiano Casalino. Laminar separation bubble noise on a propeller operating at low reynolds numbers. *AIAA Journal*, 60(9):5324–5335, 2022.

[41] Edoardo Grande, Gianluca Romani, Daniele Ragni, Francesco Avallone, and Damiano Casalino. Aeroacoustic investigation of a propeller operating at low reynolds numbers. *AIAA Journal*, 60(2):860–871, 2022.

[42] Eric Greenwood, Kenneth S Brentner, Robert F Rau, and Ze Feng Ted Gan. Challenges and opportunities for low noise electric aircraft. *International Journal of Aeroacoustics*, 21(5-7):315–381, 2022.

[43] Donald B Hanson. Spectrum of rotor noise caused by atmospheric turbulence. *The Journal of the Acoustical Society of America*, 56(1):110–126, 1974.

[44] Donald B Hanson. Influence of propeller design parameters on far-field harmonic noise in forward flight. *AIAA Journal*, 18(11):1313–1319, 1980.

[45] Nanyaporn Intaratep, William N Alexander, William J Devenport, Sheryl M Grace, and Amanda Dropkin. Experimental study of quadcopter acoustics and performance at static thrust conditions. In *22nd AIAA/CEAS Aeroacoustics Conference*, page 2873, 2016.

[46] Rohit Jain. Computational fluid dynamics transition models validation for rotors in unsteady flow conditions. *Journal of Aircraft*, 59(4):875–895, 2022.

[47] W Johnson and C Silva. Nasa concept vehicles and the engineering of advanced air mobility aircraft. *The Aeronautical Journal*, 126(1295):59–91, 2022.

[48] Wayne Johnson, Christopher Silva, and Eduardo Solis. Concept vehicles for vtol air taxi operations. In *AHS Specialists"Conference on Aeromechanics Design for Transformative Vertical Flight*, number ARC-E-DAA-TN50731, 2018.

[49] Yong Su Jung, James Baeder, and Chengjian He. Empirical rotor broadband noise prediction using cfd boundary layer parameter extraction. *Journal of the American Helicopter Society*, 2023.

[50] Joseph Katz and Allen Plotkin. *Low-speed aerodynamics*, volume 13. Cambridge university press, 2001.

[51] Joseph G Kocheemoolayil, Gerrit-Daniel Stich, Michael F Barad, and Cetin C Kiris. Propeller noise predictions using the lattice boltzmann method. In *25th AIAA/CEAS Aeroacoustics Conference*, page 2661, 2019.

[52] HP Kreplin, H Vollmers, and HU Meier. Wall shear stress measurements on an inclined prolate spheroid in the dfvlr 3 m× 3 m low speed wind tunnel, goettingen. *DFVLR-AVA, Report IB*, pages 22–84, 1985.

[53] N Krimmelbein and R Radespiel. Transition prediction for three-dimensional flows using parallel computation. *Computers & Fluids*, 38(1):121–136, 2009.

[54] Vinod K Lakshminarayan and James D Baeder. Computational investigation of micro hovering rotor aerodynamics. *Journal of the American Helicopter Society*, 55(2):22001–22001, 2010.

[55] Robin Langtry. Extending the gamma-rethetat correlation based transition model for crossflow effects. In *45th AIAA fluid dynamics conference*, page 2474, 2015.

[56] Robin B. Langtry and Florian R. Menter. Correlation-based transition modeling for unstructured parallelized computational fluid dynamics codes. *AIAA Journal*, 47: 2894–2906, 2009.

[57] Brian Edward Launder, G Jr Reece, and W Rodi. Progress in the development of a reynolds-stress turbulence closure. *Journal of fluid mechanics*, 68(3):537–566, 1975.

[58] Seongkyu Lee. Empirical wall-pressure spectral modeling for zero and adverse pressure gradient flows. *AIAA Journal*, 56(5):1818–1829, 2018.

[59] Seongkyu Lee, Lorna Ayton, Franck Bertagnolio, Stephane Moreau, Tze Pei Chong, and Phillip Joseph. Turbulent boundary layer trailing-edge noise: Theory, computation, experiment, and application. *Progress in Aerospace Sciences*, 126:100737, 2021.

[60] Gordon J Leishman. *Principles of helicopter aerodynamics with CD extra*. Cambridge university press, 2006.

[61] Sicheng Li and Seongkyu Lee. Predictions and validations of small-scale rotor noise using ucd-quietfly. In *Proceedings of the American Helicopter Society Technical Conference on Aeromechanics Design for Transformative Vertical Flight, San Jose, CA*, pages 25–27, 2022.

[62] Sicheng Kevin Li and Seongkyu Lee. Prediction of rotorcraft broadband trailing-edge noise and parameter sensitivity study. *Journal of the American Helicopter Society*, 65 (4):1–14, 2020.

[63] Su Liu and Isam Janajreh. Development and application of an improved blade element momentum method model on horizontal axis wind turbines. *International Journal of Energy and Environmental Engineering*, 3:1–10, 2012.

[64] Xiran Liu, Dan Zhao, and Nay Lin Oo. Comparison studies on aerodynamic performances of a rotating propeller for small-size uavs. *Aerospace Science and Technology*, 133:108148, 2023.

[65] Leonard V Lopes, David D Boyd Jr, Douglas M Nark, and Karl E Wiedemann. Identification of spurious signals from permeable ffowcs williams and hawkings surfaces. In *American Helicopter Society (AHS) International Annual Forum and Technology Display*, number NF1676L-25336, 2017.

[66] Dongli Ma, Yanping Zhao, Yuhang Qiao, and Guanxiong Li. Effects of relative thickness on aerodynamic characteristics of airfoil at a low reynolds number. *Chinese Journal of Aeronautics*, 28(4):1003–1015, 2015.

[67] Reda R Mankbadi, Samuel Afari, and Vladimir V Golubev. Towards high-fidelity analysis of noise radiation and control of propeller-driven uav. In *25th AIAA/CEAS Aeroacoustics Conference*, page 2632, 2019.

[68] Reda R Mankbadi, Samuel O Afari, and Vladimir V Golubev. High-fidelity simulations of noise generation in a propeller-driven unmanned aerial vehicle. *AIAA Journal*, 59 (3):1020–1039, 2021.

[69] Michael Marques Goncalves, Vladimir V Golubev, and Anastasios S Lyrintzis. Analysis of e-vtol rotor noise predictions. In *AIAA SCITECH 2024 Forum*, page 2809, 2024.

[70] Matthew H McCrink and James W Gregory. Blade element momentum modeling of low-reynolds electric propulsion systems. *Journal of Aircraft*, 54(1):163–176, 2017.

[71] Shivaji Medida and James Baeder. A new crossflow transition onset criterion for rans turbulence models. In *21st AIAA Computational Fluid Dynamics Conference*, page 3081, 2013.

[72] F. R. Menter, R. Langtry, and S. Völker. Transition modelling for general purpose cfd codes. *Flow, Turbulence and Combustion*, 77:277–303, 2006.

[73] Florian Menter. A correlation-based transition model using local variables - part i: Model formulation, 2006.

[74] Florian R Menter. Two-equation eddy-viscosity turbulence models for engineering applications. *AIAA journal*, 32(8):1598–1605, 1994.

[75] Florian R Menter. Influence of freestream values on k-omega turbulence model predictions. *AIAA journal*, 30(6):1657–1659, 1992.

[76] Florian R. Menter, Pavel E. Smirnov, Tao Liu, and Ravikanth Avancha. A one-equation local correlation-based transition model. *Flow, Turbulence and Combustion*, 95:583–619, 2015.

[77] Monal Merchant and L Scott Miller. Propeller performance measurement for low reynolds number uav applications. In *44th AIAA Aerospace Sciences Meeting and Exhibit*, page 1127, 2006.

[78] M.V Michelassi, J.G Wissink, and W. Rodi. Analysis of dns and les of flow in a low pressureturbine cascade with incoming wakes and comparison with experiments. *Flow Turbul. Combust.*, 69:295–330, 2002.

[79] Amadeo Moran-Guerrero, Leo Miguel Gonzalez-Gutierrez, Adriana Oliva-Remola, and Hector R Diaz-Ojeda. On the influence of transition modeling and crossflow effects on open water propeller simulations. *Ocean Engineering*, 156:101–119, 2018.

[80] Christoph Müller and Florian Herbst. Modelling of crossflow-induced transition based on local variables. *Proc. ECCOMAS, Paper*, (2252):72, 2014.

[81] Riccardo Mura and Samet C. Cakmakcioglu. A revised one-equation transitional model for external aerodynamics - part i: Theory, validation and base cases. *Applied CFD Modeling and Numerical Corrections with Experimental Data II*, June, 2020.

[82] Shengyang Nie, Normann Krimmelbein, Andreas Krumbein, and Cornelia Grabe. Coupling of a reynolds stress model with the γ- $re_{\theta t}$ transition model. *AIAA Journal*, 56 (1):146–157, 2018.

[83] Shengyang Nie, Normann Krimmelbein, Andreas Krumbein, and Cornelia Grabe. Extension of a reynolds-stress-based transition transport model for crossflow transition. *Journal of Aircraft*, 55(4):1641–1654, 2018.

[84] Marie Paul Nisingizwe, Pacifique Ndishimye, Katare Swaibu, Ladislas Nshimiyimana, Prosper Karame, Valentine Dushimiyimana, Jean Pierre Musabyimana, Clarisse Musanabaganwa, Sabin Nsanzimana, and Michael R Law. Effect of unmanned aerial vehicle (drone) delivery on blood product delivery time and wastage in rwanda: a retrospective, cross-sectional study and time series analysis. *The Lancet Global Health*, 10(4):e564–e569, 2022.

[85] National Academies of Sciences, Division on Engineering, Physical Sciences, Aeronautics, Space Engineering Board, and Committee on Enhancing Air Mobilityâ¬" A National Blueprint. *Advancing aerial mobility: A national blueprint.* National Academies Press, 2020.

[86] Michael Ol, Cale Zeune, and Michael Logan. Analytical/experimental comparison for small electric unmanned air vehicle propellers. In *26th AIAA Applied Aerodynamics Conference*, page 7345, 2008.

[87] Nicole A Pettingill and Nikolas S Zawodny. Identification and prediction of broadband noise for a small quadcopter. In *75th Annual Forum & Technology Display*, 2019.

[88] Naina Pisharoti and Stefano Brizzolara. Validation study of reynolds stress model coupled with gamma transition for uav propellers. In *ASME International Mechanical Engineering Congress and Exposition*, volume 85666, page V010T10A012. American Society of Mechanical Engineers, 2021.

[89] Naina Pisharoti, Lakshmi Miller, and Stefano Brizzolara. Comparative study of first and second-order closure rans transition turbulence models for the 6:1 prolate spheroid. In *34*th *Symposium on Naval Hydrodynamics*, 2022.

[90] Naina Pisharoti, John Webster, and Stefano Brizzolara. Reynolds stress turbulence modelling with γ transition model. *International Journal of Computational Fluid Dynamics*, pages 1–23, 2022.

[91] Naina Pisharoti, Jeremiah Whelchel, W. Nathan Alexander, and Stefano Brizzolara. Experimental and numerical investigation of isolated swept rotors for uavs. *Vertical Flight Society 79th Annual Forum Technology Display*, 2023.

[92] Naina Pisharoti, Jeremiah Whelchel, William N Alexander, and Stefano Brizzolara.

Cfd-based aerodynamic and aeroacoustic analysis of large payload multi-copter rotors. In *AIAA SCITECH 2023 Forum*, page 0617, 2023.

[93] Stephen A Rizzi, Dennis L Huff, David D Boyd, Paul Bent, Brenda S Henderson, Kyle A Pascioni, D Caleb Sargent, David L Josephson, Mehmet Marsan, Hua Bill He, et al. Urban air mobility noise: Current practice, gaps, and recommendations. Technical report, 2020.

[94] Carl Russell, Jaewoo Jung, Gina Willink, and Brett Glasner. Wind tunnel and hover performance test results for multicopter uas vehicles. In *AHS 72nd annual forum*, pages 16–19, 2016.

[95] J. Russell. Length and bursting of separation bubbles: A physical interpretation of pressure distribution. 1979.

[96] Darshan Sarojini, Marius L Ruh, Anugrah Jo Joshy, Jiayao Yan, Alexander K Ivanov, Luca Scotzniovsky, Andrew H Fletcher, Nicholas C Orndorff, Mark Sperry, Victor E Gandarillas, et al. Large-scale multidisciplinary design optimization of an evtol aircraft using comprehensive analysis. In *AIAA SciTech 2023 Forum*, page 0146, 2023.

[97] Herman Schlichting and Klaus Gersten. *Boundary Layer Theory.* Springer, 2000.

[98] R Schlinker and R Amiet. Helicopter rotor trailing edge noise. In *7th Aeroacoustics Conference*, page 2001, 1981.

[99] Galen B Schubauer and Philip S Klebanoff. Contributions on the mechanics of boundary-layer transition. 1955.

[100] G.B. Schubauer and H.K.Skramstad. Laminar boundary-layer oscillations and stability of laminar flow. *Journal Of The Aeronautical Sciences*, 14(2):69–78, 1947.

[101] A. Smith and N. Gamberoni. Transition, pressure gradient and stability theory. *Douglas Aircraft Company*, 1956.

[102] Philippe Spalart and Steven Allmaras. A one-equation turbulence model for aerodynamic flows. *AIAA*, 439, 01 1992.

[103] Philippe R Spalart. Detached-eddy simulation. *Annual review of fluid mechanics*, 41: 181–202, 2009.

[104] Charles Speziale, Sutanu Sarkar, and T. Gatski. Modelling the pressure-strain correlation of turbulence - an invariant dynamical systems approach. *Journal of Fluid Mechanics*, 227, 07 1991.

[105] James H Stephenson, Daniel Weitsman, and Nikolas S Zawodny. Effects of flow recirculation on unmanned aircraft system (uas) acoustic measurements in closed anechoic chambers. *The Journal of the Acoustical Society of America*, 145(3):1153–1155, 2019.

[106] Gerrit-Daniel Stich, Luis S Fernandes, Jared C Duensing, Jeffrey A Housman, Gaetan K Kenway, and Cetin C Kiris. Validation of actuator disk, actuator line and sliding mesh methods within the lava solver. In *The 11th International Conference on Computational Fluid Dynamics*, number ICCFD11-2022-0903, 2022.

[107] Christopher KW Tam. Recent advances in computational aeroacoustics. *Fluid dynamics research*, 38(9):591, 2006.

[108] Austin Thai, Rohit Jain, and Sheryl Grace. Cfd validation of small quadrotor performance using createtm-av helios. In *VFS 75th Annual Forum & Technology Display*, 2019.

[109] Austin D Thai, Sheryl M Grace, and Rohit Jain. Effect of turbulence modeling selection

within helios for small quadrotor aerodynamics. *Journal of Aircraft*, 59(4):927–945, 2022.

[110] Austin David Thai. *Development of high-fidelity computational methods for prediction of multirotor aerodynamics, aeroacoustics, and trim.* PhD thesis, Boston University, 2022.

[111] Austin David Thai, Elisa De Paola, Alessandro Di Marco, Luana Georgiana Stoica, Roberto Camussi, Roberto Tron, and Sheryl Marie Grace. Experimental and computational aeroacoustic investigation of small rotor interactions in hover. *Applied Sciences*, 11(21):10016, 2021.

[112] Subramanian Vallinayagam Pillai and Sylvain Lardeau. Accounting crossflow effects in one-equation local correlation-based transition model. In *8th AIAA Theoretical Fluid Mechanics Conference*, page 3159, 2017.

[113] J.L van Ingen. A suggested semi-empirical method for the calculation of the boundary layer transition region. *VTH-74*, 1956.

[114] Patricia Ventura Diaz and Steven Yoon. High-fidelity computational aerodynamics of multi-rotor unmanned aerial vehicles. In *2018 AIAA Aerospace Sciences Meeting*, page 1266, 2018.

[115] H.K. Versteeg and W. Malalasekera. *An Introduction to Computational Fluid Dynamics: The Finite Volume Method.* Pearson Education Limited, 2007. ISBN 9780131274983. URL https://books.google.com/books?id=RvBZ-UMpGzIC.

[116] D. Keith Walters and Davor Cokljat. A three-equation eddy-viscosity model for reynolds-averaged navier–stokes simulations of transitional flow. *Journal of Fluids Engineering*, 130(12), 2008.

[117] D. Keith Walters and James H. Leylek. A new model for boundary layer transition using a single-point rans approach. *Journal of Turbomachinery*, 126(1):193–202, 2004.

[118] Meng Wang, Jonathan B Freund, and Sanjiva K Lele. Computational prediction of flow-generated sound. *Annu. Rev. Fluid Mech.*, 38:483–512, 2006.

[119] Jeremiah Whelchel, W. Nathan Alexander, Naina Pisharoti, Stefano Brizzolara, Rohit Murali, and Daniel J. Stilwell. Examination of broadband and tonal noise sources produced by evtol propellers and drive systems. In *28th AIAA/CEAS Aeroacoustics Conference*, 2022.

[120] Jeremiah Mark Whelchel. *Measurement and Prediction of Rotor Noise Sources for sUAS in Outdoor and Laboratory Environments*. PhD thesis, Virginia Tech, 2023.

[121] Arthur Wiedemann, Colin P Britcher, and Chris R Fuller. A study of the aeroacoustics of swept propellers for small unmanned aerial vehicles. In *AIAA Scitech 2021 Forum*, page 1926, 2021.

[122] David C Wilcox. Formulation of the k-w turbulence model revisited. *AIAA Journal*, 46(11), 2008.

[123] JE Ffowcs Williams and David L Hawkings. Sound generation by turbulence and surfaces in arbitrary motion. *Philosophical Transactions for the Royal Society of London. Series A, Mathematical and Physical Sciences*, pages 321–342, 1969.

[124] Justin Winslow, Hikaru Otsuka, Bharath Govindarajan, and Inderjit Chopra. Basic understanding of airfoil characteristics at low reynolds numbers (10 4–10 5). *Journal of aircraft*, 55(3):1050–1061, 2018.

[125] Jordon Won, Nikos Trembois, and Seongkyu Lee. Towards accurate broadband noise predictions using cfd. pages 1–15, 05 2023. doi: 10.4050/F-0079-2023-17950.

[126] T Wright and WE Simmons. Blade sweep for low-speed axial fans. 1990.

[127] Xiaohua Wu and Parviz Moin. Direct numerical simulation of turbulence in a nominally zero-pressure-gradient flat-plate boundary layer. *Journal of Fluid Mechanics*, 630:5–41, 2009.

[128] Xiaohua Wu, Robert G. Jacobs, Hunt Julian C.R., and Paul A. Durbin. Simulation of boundary layer transition induced by periodically passing wakes. *Journal of Fluid Mechanics*, 398:109–153, 1999.

[129] Liangyu Xu, Emilio Baglietto, and Stefano Brizzolara. Extending the applicability of rans turbulence closures to the simulation of transitional flow around hydrofoils at low reynolds number. *Ocean Engineering*, 164:1–12, 2018.

[130] Seokkwan Yoon, Neal Chaderjian, Thomas H Pulliam, and Terry Holst. Effect of turbulence modeling on hovering rotor flows. In *45th AIAA Fluid Dynamics Conference*, page 2766, 2015.

[131] Nikolas S Zawodny, D Douglas Boyd Jr, and Casey L Burley. Acoustic characterization and prediction of representative, small-scale rotary-wing unmanned aircraft system components. In *American Helicopter Society (AHS) Annual Forum*, number NF1676L-22587, 2016.

[132] Di Zhang. *Turbulence Modeling and Simulation of Unsteady Transitional Boundary Layers and Wakes with Application to Wind Turbine Aerodynamics*. PhD thesis, Virginia Tech, 2017.